Petrophysical and Mechanical Characterization of the Volcanic Rocks in the Hellisheiði Geothermal Field and implications of Thermal Fracturing in CO_2 mineralization

E. Redondo García

Delft University of Technology

Petrophysical and Mechanical Characterization of the Volcanic Rocks in the Hellisheiði Geothermal Field and implications of Thermal Fracturing in CO_2 mineralization

by

E. Redondo García

to obtain the degree of **Master of Science**
in Applied Earth Sciences
at the Delft University of Technology,
to be defended publicly on Monday May 15, 2023 at 10:15 AM.

Student number:	4894189	
Supervisors:	Dr. A. Barnhoorn,	TU Delft, supervisor
	Dr. M. Janssen,	TU Delft, supervisor
Thesis committee:	Dr. P.J. Vardon,	TU Delft
	Dr. ir. D.S. Draganov,	TU Delft

Cover: *Hellisheidi Power Plant. Photo by Orkuveita Reykjavikur.*

An electronic version of this thesis is available at `http://repository.tudelft.nl/`.

TU Delft

Abstract

The level of advancement in the understanding of the mechanical properties of volcanic rocks is comparatively lower than that of sedimentary rocks. As part of the SUCCEED Project (*Synergetic Utilisation of CO*2 *Storage Coupled with Geothermal Energy Deployment*), which aims to investigate the feasibility of injecting captured and produced CO_2 into the reservoirs to enhance geothermal production and achieve permanent CO_2 storage at the Hellisheiði Geothermal Field in Iceland, this experimental research provides significant insights into the petrophysical and mechanical properties of the volcanic rocks collected from surface outcrops. The subsurface in Hellisheiði is mainly built up of hyaloclastite formations and interglacial basaltic lavas. During a field campaign samples were collected in different outcrops, ensuring that the samples were of high quality and sufficiently diverse to enable comprehensive analysis. Four samples per block and rock type have been prepared from the collected blocks, and they have been subjected to different laboratory tests to evaluate their petrophysical properties, such as porosity, density, and permeability, and their geomechanical behavior, using Unconfined Compression Test (UCS), Active-Source Acoustic Test, and Splitting Tensile Strength Test. Additionally, laboratory experiments have been conducted to investigate the impact of rapid cooling on rock damage due to thermal fracturing. The results show that there are interdependent relationships between porosity, bulk density, ultimate strength, Young's modulus, and wave velocities that can be observed when considering average values per rock. The rocks studied showed a negative correlation between porosity and other parameters and a direct correlation between ultimate strength and Young's Modulus. When examining individual rock samples, no significant correlations were observed between porosity and other parameters, however, those correlations where evident when comparing between different rock types, emphasizing the importance of analyzing rock properties from a broader perspective. The rocks studied could be classified into five units based on their petrophysical and mechanical properties. Ordered from higher porosity and lower mechanical parameters, these units are: unit 1 consists of hyaloclastite HH-1, unit 2 includes porous basalts HBA-18 and HPB-23, unit 3 consists of low-porosity basalts HB-4 and HBimp-9, unit 4 is made up of dike ND-6, and unit 5 comprises gabbro G. This implies that there is a notable variation in the properties of rocks between different units, but the properties of rocks within the same unit do not differ significantly. Volcanic rocks have a significant amount of unconnected porosity, which, if connected, can enhance the storage capacity of the reservoir and improve the reactive surface area of the rocks in contact with the reinjected fluid, leading to a more efficient mineral storage process. The results of a thermal shock conducted to simulate reservoir and injection temperatures (270ºC and 60ºC) have shown no significant changes in the petrophysical and mechanical properties of the rocks, indicating that this temperature difference does not increase the effective porosity nor compromise the integrity of the reservoir. This study validates the potential use of certain rocks collected from surface outcrops in Hellisheiði as reservoir analogs for future geological models, particularly those with lower porosity.

Acknowledgements

I would like to express my gratitude to everyone who has contributed in any way to this work. I want to especially thank my supervisor Dr. Auke Barnhoorn for his support and guidance throughout this project. I also want to thank Dr. Martijn Janssen for guiding me through laboratory tests and data analysis. I am grateful to my professors Dr. Deyan Draganov and Dr. Phil Vardon for their thoughtful feedback, which has helped shape my research. Additionally, I want to express my gratitude to the technicians Marc Friebel and Jens van den Berg for the good times during the field campaign and their invaluable assistance in the laboratory. I would also like to thank Milad Nardeloo and Dr. Debanjan Chandra for their help with laboratory work. Thanks also to my colleagues, with whom I have grown professionally.

I wish to thank my parents and sister for supporting me throughout my academic years and believing in me in every step of the way. I am immensely grateful to my Dutch family for being a fundamental support since I arrived in the Netherlands. Lastly, I would like to express my gratitude to my friends for always being there, even when some of them are miles away.

E. Redondo García
Delft, May 2023

Contents

1
Introduction

1.1. Iceland's Energy Context and Carbon Footprint.

The fight against climate change is one of the main environmental challenges of this time. The reliance on fossil fuels as the primary source of energy is unsustainable due to the environmental impact of greenhouse-gas emissions, predicted resource depletion and the economic instability that implies being energetically dependant of other countries for those who lack these resources.

The energy scenario of Iceland differs from other countries as it lacks domestic resources of oil and natural gas and therefore relies on imported fossil fuels that are primarily used for transportation by land, sea and air (Orkustofnun 2021b) (See Apendix A). The share of renewable energy in Iceland is among the highest in the world, being the world's largest green energy producer per capita. During the past century the country has evolved from an impoverished nation, dependent upon peat and imported coal for its energy, to a land of plenty, where practically all stationary energy is derived from renewable resources. Harnessing local energy resources was, in fact, a precondition for economic development of the country (Orkustofnun 2006). Energy utilization in Iceland, in the modern sense, started at the beginning of the 20^{th} century, when the first hydropower generators were built. At this time, Icelanders, who had only used natural geothermal springs for bathing and washing, started to use geothermal energy for heating by experimenting with piping through which geothermal steam flowed to heat their houses. Currently, geothermal energy is used for both direct heat and electricity generation. In 2020, geothermal represented around 70% of the total energy consumption, covering 31% of the total electricity produced and 89% of the total space heating. In the same year, about 72% of the total heat use was for space heating. (Orkustofnun 2021a). Iceland is one of the 197 countries that adopted the historic 2015 United Nations Paris Agreement (United-Nations 2015), committing to achieve net-zero emissions to address climate change. The Icelandic government aims to continue being an example of national energy transition with large positive economical and environmental benefits.

Geothermal energy is an environmentally friendly, renewable, and sustainable source of electricity and heat and contributes significantly to the Icelandic energy budget. However, its utilization, particularly power production, may result in significant greenhouse gas (GHG) emissions (Fridriksson et al. 2017). Non-condensable gases of magmatic origin are found dissolved in the geothermal water, mostly in the form of carbon dioxide (CO_2) and hydrogen sulfide (H_2S) but also as sulfur oxide, methane, ammonia and nitrogen (Sigfússon et al. 2018). These gases typically represent less than 5% of the geothermal fluid by weight and the concentration of CO_2 can be as high as 97.8% by mole (Bloomfield et al. 1999) but can vary, mainly due to natural processes such as when magmatic events create an influx of CO_2 into the geothermal reservoir. Non-condensable gases are separated from the geothermal fluid at the cooling tower of power plants and released into the atmosphere. The geothermal fluid depleted in CO_2 is generally injected back into the reservoir. Despite the fact that the amount of CO_2 emitted during geothermal utilization is estimated to be up to 5% of CO_2 emissions from a fossil-fuel-burning power plant of a comparable size (Duffield et al. 2003) these emissions are not desirable.

Carbon Capture and Storage (CCS) is a technology to reduce anthropogenic CO_2 emissions into the atmosphere by capturing and injecting the gas into the deep subsurface for long-time storage (Bandilla

2020). However, for CCS to significantly reduce carbon emissions, very large amounts of CO_2 will need to be captured and stored. The subsurface offers vast reservoir capacities sufficient to accommodate great volumes of CO_2. Nevertheless, the effectiveness of the storage depends strongly on the retention time, reservoir stability, and the risk of leakage (Hawkins 2004). The CarbFix method was developed to reduce the GHG emissions of the Hellisheiði Power Plant by reinjecting the co-produced CO_2 along with the spent geothermal fluid and turning it ”into stone” (CarbFix 2022).

1.2. The Hellisheiði Power Plant and the CarbFix method.

The Hellisheiði Power Plant is a steam combined heat and power plant (GCHP) owned by Orkuveita Reykjavíkur (OR). It is a flash power plant located in a high-temperature geothermal area about 30 km east of Reykjavík. The generation of electricity is performed in two separate pressure stages: electricity produced with high-pressure turbines corresponding to a single flash power plant and the additional electricity produced with a low-pressure turbine, making the overall plant a double flash power plant. Electricity generation started in 2006 and hot water production in 2010 (Karlsdóttir et al. 2010). It has 303 MWe of electric production capacity installed, accounting for 46% of the total electric capacity of geothermal power plants in Iceland, and 133 MWth of thermal capacity serving the local district heating system, what makes it the largest geothermal combined heat and power plant in the country (Karlsdóttir et al. 2015). Currently, the power plant is in operation at near full capacity. The geothermal site has a total of 61 production wells and 17 reinjection wells (Ratouis et al. 2019). Regarding GHG emissions, data from 2015 to 2021 (Table 1.1) shows that the CO_2 net emissions have been reduced over time.

	Unit	**2015**	**2016**	**2017**	**2018**	**2019**	**2020**	**2021**
GHG emissions	tCO_2eq/year	49,900	46,650	43,500	45,950	49,950	50,850	47,500

Table 1.1: Annual net CO_2 emissions from the Hellisheiði Geothermal Power Plant in 2015-2021 period. Source: Reykjavik Energy Annual Environmental data report 2021 Reykjavik Energy Group (OR) 2021.

As it can be observed in Figure 1.1, the main cause for this reduction has been the implementation of the carbon capture and storage (CCS) technologies developed by CarbFix. The project developed methods and technology for the permanent *in situ* mineral storage of CO_2 and CO_2-H_2S gas mixtures in basalts. The injection of CO_2 into young basaltic formations provides significant advantages, including great storage potential and permanent storage over geological time scales. The minerals forming basaltic rocks are rich in divalent cations such as Ca^{2+}, Mg^{2+}, and Fe^{2+}. The acidic CO_2-charged fluid

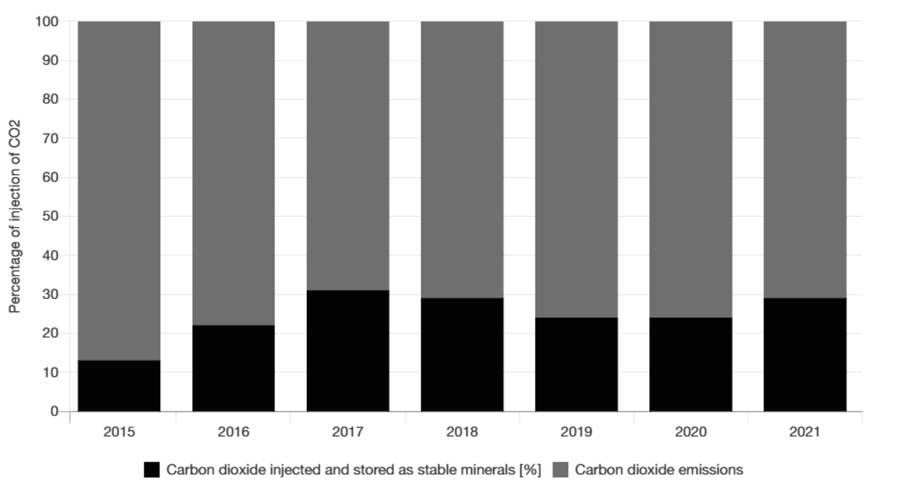

Figure 1.1: Annual percentage of injection of carbon dioxide from the Hellisheiði Geothermal Power Plant in 2013-2021. Modified from OR (2021).

accelerates the release of these metals through mineral dissolution, promoting the formation of carbonate minerals including calcite, magnesite and siderite (Gislason et al. 2014; Gislason et al. 2003), thereby providing mineral storage of the injected CO_2. This has been confirmed by other authors (Xu et al. 2006), who studied the mineral carbonation potential of different minerals and showed that rocks with high proportions of divalent cations have the greatest carbonation potential, such as plagioclase (Ca,Na)$Al_{1.70}Si_{2.30}O_8$), pyroxene ($(Mg,Fe)_2SiO_4$), and olivine ($(Ca,Mg,Fe)_2SiO_3$), the most abundant minerals in basaltic rocks at the CarbFix injection site in Hellisheiði. Volcanic glass is also common.

$$CO_{2\,(g)} + H_2O = H_2CO_{3\,(aq)} \tag{1.1}$$

$$H_2CO_{3\,(aq)} = HCO_3{}^- + H^+ \tag{1.2}$$

$$HCO_3^- = CO_3{}^{2-} + H^+ \tag{1.3}$$

$$(Ca, Mg, Fe)^{2+} + CO_3{}^{2-} = (Ca, Mg, Fe)CO_{3\,(s)} \tag{1.4}$$

The basic concept of CarbFix is to dissolve CO_2 in water before it is dispersed as a single-phase fluid into the pore space of basaltic formations (Aradóttir et al. 2011). As shown in equation 1.1, CO_2 is dissolved in water to form carbonic acid (H_2CO_3), which can dissociate into bicarbonate (HCO_3^-) and carbonate ($CO_3{}^{2-}$) as it can be observed in equations 1.2 and 1.3 respectively. That carbonate will then be combined with the released cations to form calcite ($CaCO_3$), dolomite ($CaMg(CO_3)_2$), magnesite ($MgCO_3$) and siderite ($FeCO_3$). See equation 1.4. However, it is difficult to predict beforehand which of these carbonates will actually precipitate in the subsurface during CO_2 injection. The stability of carbonates is well-understood in terms of thermodynamic limits, which indicate that they can only remain stable at temperatures below 300ºC. Observations of hydrothermally altered basaltic rocks from Iceland show that calcite does not form at temperatures above 290ºC (Franzson 1998).

The standard approach to geological storage is to inject CO_2 as a separate supercritical phase in deep saline aquifers, depleted oil and gas reservoirs and in deep unmineable coal seams at depths >800 m. Under this conditions, CO_2 stays supercritical and is buoyant with respect to the host rocks and aqueous fluids at relevant temperature and pressure. In the absence of a proper impermeable cap rock, injected CO_2 could therefore migrate laterally or upward, reducing long-term storage and risking contamination of shallower groundwater resources (Benson et al. 2008). In this particular case, rather than injecting CO_2 directly into geological formations, CarbFix has developed a technology to dissolve CO_2 into well water and formation fluids during injection. Once dissolved, the CO_2 is no longer buoyant and the presence of a cap rock is no longer needed. Furthermore, carbon mineralization is enhanced and the formation of minerals ensures storage stability (Metz et al. 2005, Oelkers et al. 2008). This process was studied in a pilot-scale injection carried out in Hellisheiði in 2012, where 175 tons of CO_2 were injected in the Hellisheiði Geothermal Field (Sigfusson et al. 2015). Extensive geochemical monitoring was carried out prior to, during, and after both injections, which revealed the rapid mineralization of the injected gas. Over 95% of the injected CO_2 was mineralized in less than two years (Matter et al. 2016). Following the success of the first pilot, the CarbFix method was scaled up as part of the CarbFix2 project in 2014.

For the sake of clarity, it is important to mention that although the proximity to the geothermal plant allows access to large amounts of CO_2, CarbFix also injects CO_2 from other sources. Currently, CarbFix works in collaboration with Climeworks, a Swiss clean-tech company specializing in direct air capture (DAC) technology. Together they developed the 'Arctic Fox' plant, that in combination with the CarbFix2 project demonstrated the feasibility of combining DAC and CO_2 mineral storage of 50 tons of CO_2 per year (Gutknecht et al. 2018). In 2020, following successful pilot operations, Climeworks and Carbfix made a ground-breaking agreement to significantly scale-up atmospheric CO_2 removal and storage: project 'Orca' (Climeworks 2022), which captured around 4.000 tons of CO_2 per year. Currently, the new plant 'Mammoth' (Climeworks 2023) is under construction and will capture 36.000 tons per year when fully operational. Furthermore, CarbFix aims to upscale the mineral storage of CO_2 by developing a cross-border carbon transport and storage hub: the 'Coda Terminal' project (CarbFix 2021). CO_2 will be captured at industrial sites in North Europe and shipped to the Terminal where it will be unloaded into onshore tanks for temporary storage and then injected into the subsurface. The goal is to create a business model that will allow them to store 3 million tonnes of CO_2 per year from 2031.

1.3. Research context: the SUCCEED project.

This master thesis is part of a larger research consortium: *Synergetic Utilisation of CO_2 Storage Coupled with Geothermal Energy Deployment* (SUCCEED). The main objective of this project is to study the viability of injecting produced and captured CO_2 into the reservoirs to enhance geothermal production and, at the same time, permanently store CO_2 at the Kizildere (Turkey) and Hellisheiði (Iceland) geothermal fields. The project aims at accelerating and maturing the use of CCUS by developing, testing and demonstrating measurement, monitoring and verification technologies that can be used in most CO_2 geological storage projects (Imperial-College-London 2020).

1.4. Research Objectives.

Geothermal reservoirs are susceptible to substantial fluctuations in temperature, stress, and pressure over both temporal and spatial scales, as stated by Grant et al. (2011). As noted by Heap et al. (2021), our knowledge of the mechanical properties of volcanic rocks is less advanced compared to that of granite and porous sedimentary rocks. In the context of exploiting geothermal energy, the mechanical properties and strength of volcanic rocks are important (Siratovich et al. 2016; Eggertsson et al. 2020; Weaver et al. 2020; Heap et al. 2020a; Weydt et al. 2020) to understand how the mentioned fluctuations can impact the reservoir properties. The diverse nature of volcanic rocks, including differences in mineralogical composition, porosity, and microstructure, such as pore size and shape, crystal size and shape, crystal content, presence of microcracks, glass, and alteration, creates a considerable obstacle in comprehending their mechanical behavior, as stated by different authors (Toramaru 2020, Blower et al. 2003, Wright et al. 2009, Shea et al. 2010, Voltolini et al. 2011, Colombier et al. 2017 and Cashman 2020).

The SUCCEED project places significant emphasis on investigating the petrophysical and geomechanical properties of reservoirs, with the goal of analyzing their response to CO_2 injection. This thesis aims to advance the knowledge of the mechanical behavior of volcanic rocks and characterize the petrophysical and mechanical properties of rocks in the Hellisheiði Geothermal Field in Iceland. Petrophysical properties such as porosity, bulk density, and permeability are measured, and the results of tests including unconfined compression, splitting tensile strength, and active-source acoustics are presented, yielding values for ultimate compressive strength, ultimate tensile strength, Young's modulus, and Poisson's ratio. The interrelation between various mechanical properties and the impact of porosity on them is discussed. Additionally, the study investigates the effects of thermal shock on the generation of fractures under reservoir and re-injection temperature conditions, as well as their impact on geomechanical behavior and CO_2 mineral storage.

Figure 1.2: Picture of cores with CO_2 mineralized in their pores. Source: CarbFix.

2

Geological Context

2.1. Tectonic Context

Iceland is located in a unique geological and tectonic context in which the divergent plate boundary between the Eurasian and the North American plates, the Mid-Atlantic ridge (MAR), coincides with a hotspot presumed to be fed by a deep mantle plume (Einarsson 1991 and Einarsson 2001). It is one of the few places on earth where an active spreading centre is located onshore and the only surface expression of the MAR. This onshore expression is known as the Neovolcanic Zone. As shown in Figure 2.1, this area runs through Iceland from north-east to south-west and as it crosses the hotspot it breaks up into a complex series of segments. The spreading rate of the MAR ranges from 18.9mm/yr at the plate boundary in north Iceland to 20.2mm/yr at the Reykjanes ridge, SW of Iceland, according to the REVEL plate motion model (Sella et al. 2002).

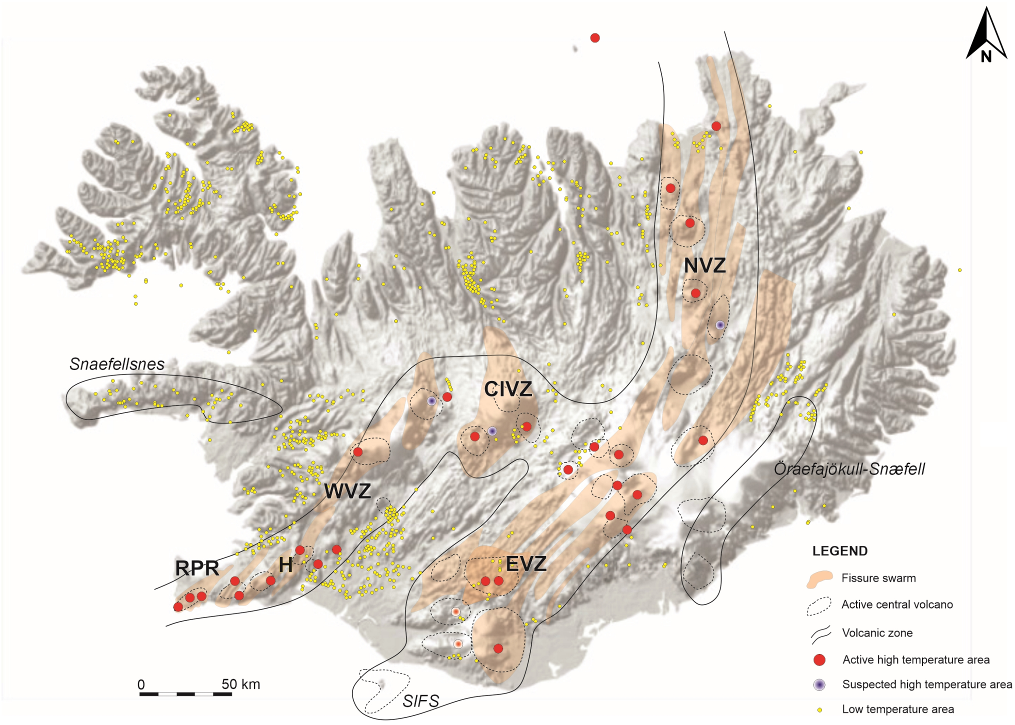

Figure 2.1: Simplified tectonic and geothermal map of Iceland. Individual plate boundary segments are indicated: RPR Reykjanes Peninsula Rift, WVZ Western Volcanic Zone, SISZ South Iceland Seismic Zone, EVZ Eastern Volcanic Zone, CIVZ Central Iceland Volcanic Zone, NVZ Northern Volcanic Zone, SIVZ South Iceland Volcanic Zone. H marks the central volcano of Hengill. Based on map of Iceland by Jóhannesson et al. (1999).

The MAR consists of a sequence of spreading centers that demarcate the ridge crest, interspersed with transform faults. The neovolcanic zone is divided into two distinct categories based on the extent of crustal spreading that has occurred within them. The volcanic flank zones are linked with minimal or negligible crustal spreading, while the volcanic rift zones are identified by significant crustal spreading. There are three volcanic flank zones: the Snæfellsnes Volcanic Zone, the South Iceland Volcanic Flank Zone (SIFZ) and the Öraefajökull-Snæfell Flank Zone. Regarding the volcanic zones, the Northern Volcanic Zone (NVZ) and the sub-parallel Western and Eastern Volcanic Zones (WVZ, EVZ) are purely divergent segments (Sæmundsson 1979; Einarsson 1991; Einarsson 2008). The WVZ and NVZ are joined by a transform E-W zone across central Iceland, known as the Central Iceland Volcanic Zone (CIVZ) (Einarsson 1991 and Stefánsson et al. 2008). The southernmost branch of the WVZ is the oblique Reykjanes Peninsula Rift (RPR). Bodvarsson (1960) and Bodvarsson (1961) classified Iceland's thermal regions into high-temperature areas, where the temperature at 1 km depth is above 200ºC, and low-temperature areas, where the temperature is below 150ºC. High-temperature areas are restricted to the active volcanic regions whereas low-temperature areas are found mostly in the flank zones.

The Hellisheiði Geothermal Field is located within the Hengill volcanic system, a region where the WVZ meets the Reykjanes Peninsula and is intersected by the strike-slip tectonic domain of the SISZ, forming the Hengill triple junction (Sæmundsson 1974; Sæmundsson 1979; Einarsson 1991; Stefánsson et al. 2008). As previously stated, the Reykjanes Peninsula is a continuation of the Reykjanes Ridge. As the ridge axis enters the shelf area SW of Iceland it is expressed as a series of constructional volcanic mounds sitting on a flat surface (Johnson et al. 1985). Figure 2.2 shows the tectonic structure here and on the Reykjanes Peninsula, an en echelon extensional rift zone about 70 km in length.

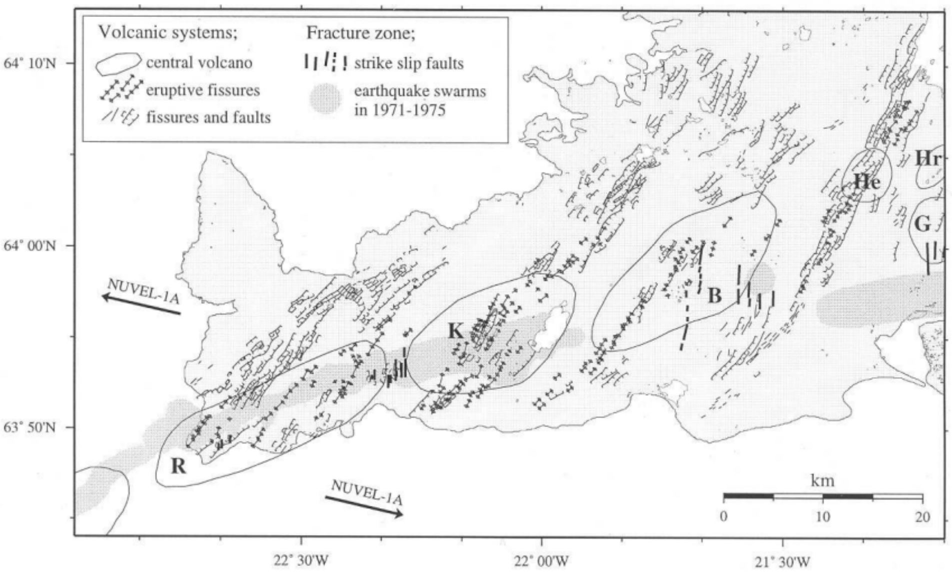

Figure 2.2: Faults and fissures on the Reykjanes Peninsula. Modified from Hreinsdóttir et al. (2001) and Clifton et al. (2007). Letters indicate volcanic systems: R, Reykjanes; K, Krísuvík; B, Brennisteinsfjöll; He, Hengill; Hr, Hrómundartindur; G, Grensdalur.

The Hengill system covers about 110 km^2 and is one of the most extensive geothermal areas in Iceland. The system is composed of a central volcano and a NE-SW oriented fissure swarm with a graben structure that extends to the northeast and southwest, which favours the rising of magma pulses and associated heat (Foulger 1995). In some places, however, the fractures are intersected features connected to the SISZ transform zone which may favor the permeability of the Hellisheiði field (Arnason et al. 2001), that is highly linked to intrusions as well as faults and fractures (Harðarson et al. 2009).

A dataset of 495 records was created by interpreting borehole breakouts and drilling-induced fractures from borehole image logs in 57 geothermal wells onshore Iceland, as well as other stress indicators such as earthquake focal mechanism solutions, geological information, and overcoring measurements

Ziegler et al. (2016) used this dataset to compile the orientation of the maximum horizontal stress (S_{Hmax}). The results, presented in Figure 2.3, demonstrate that (S_{Hmax}) orientations from different depths and stress indicators are consistent with each other and parallel to the rift axes in the active spreading regions. S_{Hmax} changes orientation from NE-SW in the South to approximately N-S in central Iceland and NNW-SSE in the North. The dataset was collected based on the assumption that the vertical stress (S_V) is a principal stress.

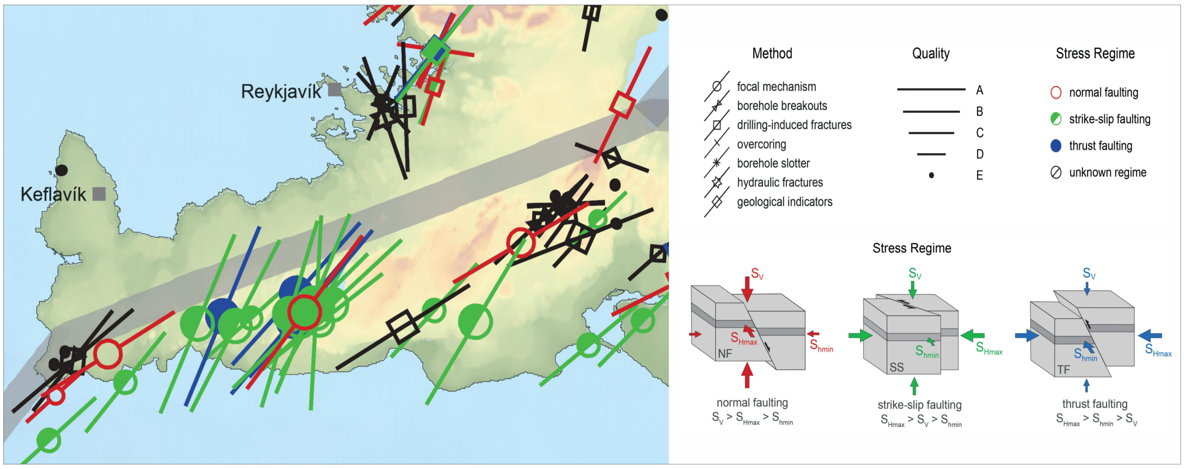

Figure 2.3: Stress map of the Reykjanes peninsula. Modified from Ziegler et al. 2016.

2.2. Stratigraphy of the Húsmuli reinjection site

This project focuses on a particular location within the Hellisheiði Geothermal Field: the Húsmuli reinjection site. This area is described as an interglacial lava shield by Sæmundsson (2016). The available subsurface information comes mainly from drilling data, drill cuttings, lithological logs, temperature and pressure data, fluid samples and productivity data (Franzson et al. 2010). There are seven production wells in the site (HE-31, HE-44, HE-48, HE-33, HE-08, HE-05, HE-46) and five re-injection wells (HN-09, HN-12, HN-14, HN-16, HN-17), whose locationa can be consulted in Figure 2.4. These wells are all directionally drilled and cased until they enter the geothermal reservoir (Ratouis et al. 2019). Information on the wellhead coordinates (ISN93), measured depth, well depth and casing depth for the most relevant wells is gathered in Table 2.1.

	Type of well	X [m]	Y [m]	Z [m.b.s.l.]	Azimuth	Measured depth [m]	Vertical depth [m]	Casing depth [m.b.s.l]
HN-16	Injection	383,449.02	395,746.96	270	350°	2204	1902	-343
HN-17	Injection	383,439.34	395,731.24	270	345°	2200	1770	-366
HE-31	Production/ Monitoring	385,036.59	396,779.94	570	280°	2703	2292	-134
HE-48	Production/ Monitoring	385,059.35	396,868.85	570	300°	2288	1850	-238
HE-44	Production/ Monitoring	385,037.10	396,863.68	570	330°	2606	2340	-256
HE-33	Production/ Monitoring	385,037.10	396,863.81	570	358°	2325	1383	-265

Table 2.1: Wellhead coordinates (ISN93), measured depth, well depth, and casing depth for the wells relevant to the Carbfix2 injection at the Húsmuli site. Source: Ratouis et al. 2019.

Figure 2.2 shows that there are two other volcanoes to the east and south of the Hengill volcano, namely the Hrómundartindur volcano (Hr) and the Grensdalur volcano (G), respectively. The available evidence suggests that the volcanic production center shifted to the west from Grensdalur to the Hengill system around 0.5 million years ago (Ingolfsson et al. 2008). The Grensdalur volcano was previously the central volcano of the extinct Hveragerdi system, which forms the base of the Hengill system.

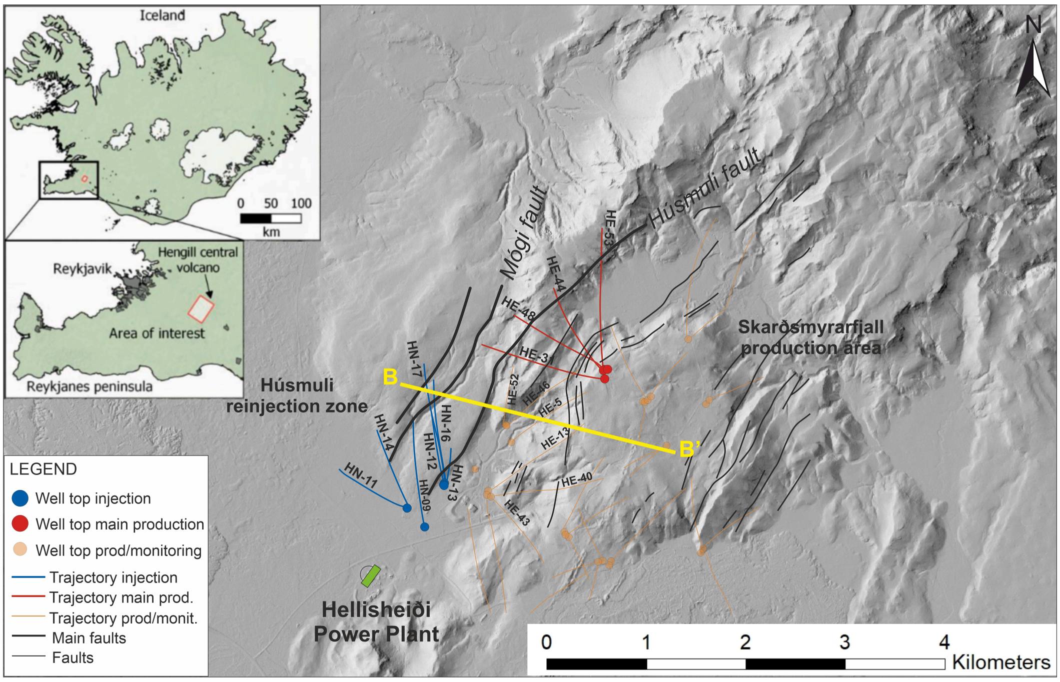

Figure 2.4: Topographical map of map of Húsmuli reinjection and main wells.

Above the base of the system, the subsurface in Hellisheiði is mainly built up of hyaloclastite formations and interglaciar compound lavas, forming a mountain complex rising up to some 420 m. Hyaloclastites are fragmented volcanoclastic deposits that form within explosive or nonexplosive magma-water interaction (Jakobsson et al. 2008). In the site, hyaloclastite intervals contain tuffs, breccias and pillow lavas that were formed during glacial periods as a result of volcanic eruptions underneath ice sheets. Basaltic lavas, on the other hand, formed during interglacial periods and flowed to the lowlands (Franzson et al. 2010). Their thickness can vary between a few meters to several hundreds of meters and their texture is described as medium- to coarse-grain basaltic lithologies. This series (Figure 2.5) is intersected by NE-SW intrusive sub-vertical fine-grained to medium-grained basaltic dykes.

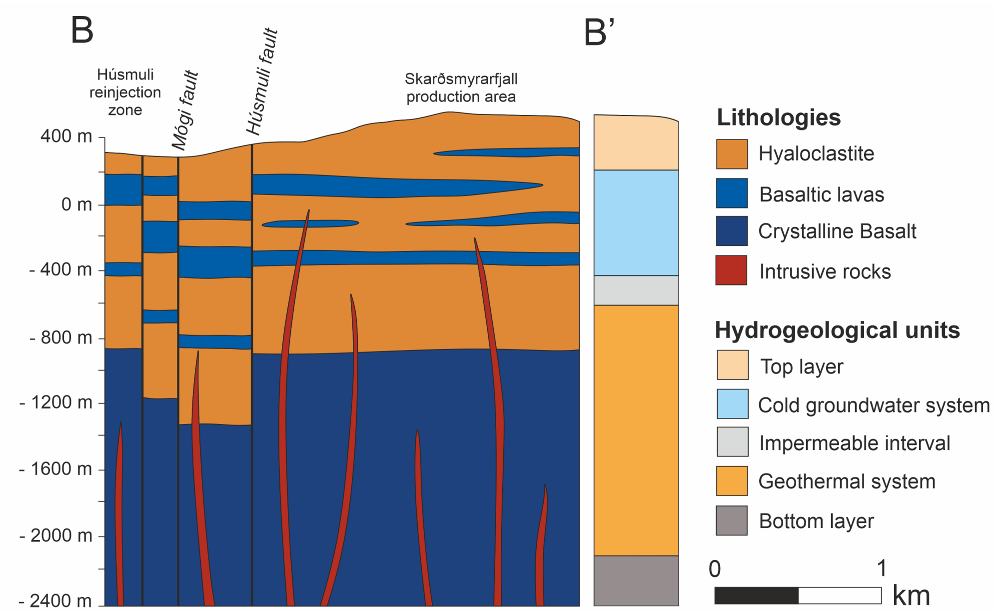

Figure 2.5: Geological cross section and hydrogeological units present in the subsurface of Húsmuli.

According to Harðarson et al. (2011), at the Húsmuli site, a series of basaltic lavas and hyaloclastites are present from the surface to about 415 m below sea level (b.s.l.). A thick layer of hyaloclastite extends from 415 m b.s.l. down to 1454 m b.s.l. The heavily altered crystalline rocks at the base of the Hengill system are believed to be situated at a depth of around 900 to 1300 meters b.s.l., as reported by Helgadóttir et al. (2010) and Snæbjörnsdóttir (2011). The intrusive rocks penetrate through the sequence of rocks at a depth below roughly 500 m b.s.l. and become the dominant part of the strata below 1500 m b.s.l..

The cold groundwater table in Húsmúli is situated at a depth of approximately 30 meters, with temperatures ranging from 5ºC to 10ºC. According to Gunnarsson et al. (2011), a 200-meter-thick hyaloclastite layer at around 400 m b.s.l. separates the groundwater geothermal system from the colder groundwater system above, with a significantly lower vertical permeability. At a depth of 1500 m b.s.l., the number of aquifers significantly decreases, and no aquifers can be found below 2000 m b.s.l.. Initially, the natural groundwater flow in Húsmúli was towards the southwest, but production activities have caused pressure changes, leading to a flow reversal. As explained by Khodayar et al. (2015), a pressure high in the injection zone and a pressure low in the production zone have caused this reversal.

The permeability of the Húsmúli site is primarily controlled by fractures. As previously mentioned, the site has a complex system of fractures, including NNE-oriented extensional faults, fault segments, and shears connected to the SISZ transform zone oriented in various directions. This fracture network has a significant impact on the permeability in Húsmúli, which appears to be highly anisotropic along the fault lines. According to Kristjánsson et al. (2016), two noteworthy NNE-trending normal faults are visible on the surface: the Mógil fault in the west, which runs through the Mógil gully, and the Húsmúli fault in the east, which makes up the western part of the Sleggubeinsdalir Valleys (Figures 2.4 and 2.5). These faults are the target of reinjection wells at the Húsmúli site, as reported by Gunnarsson et al. 2015. Permeability in the Húsmúli geothermal system is also influenced by lithological boundaries in the upper 1000 m of the system, as well as by intrusive rocks that run parallel to the NNE-trending normal faults, forming fracture networks upon their emplacement (Franzson 1988; Franzson 1998). To identify the feedzones for the geothermal wells, down-hole temperature and pressure logs, as well as loss of circulation during drilling, are used (Gunnarsson 2011). The depths of the main feedzones found in the CarbFix2 wells are presented in Table 2.2 and Figure 2.6. Typically, the geothermal fluid temperature upon reinjection ranges from 60 ºC to 80 ºC, while the down-hole temperature in the production wells ranges from around 260 ºC to 285 ºC (Gunnarsson 2011).

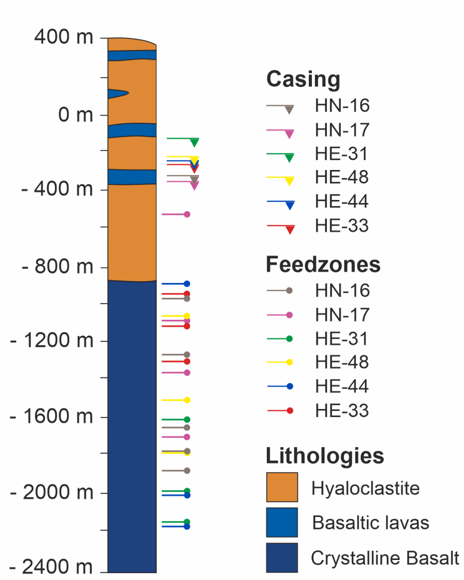

Figure 2.6: Schematic stratigraphic column showing the major feedzones encountered in each of the main six wells in Húsmuli and the depth of their casing.

Well	HN-16	HN-17	HE 31	HE 33	HE 44	HE 48
Depth [m b.s.l.]	-712	-510	-1044	-384	-332	-465
	-990	-815	-1413	-566	-1432	-859
	-1380	-1110	-1577	-744	-1609	-1222
	-1520	-1426				
	-1601					

Table 2.2: Feedzone depth locations for the wells relevant to the Carbfix re-injection site in Húsmuli. Source: Ratouis et al. 2019.

Reinjection in the Hellisheiði geothermal field is primarily carried out at Gráuhnúkar and Húsmúli sites (refer to Figure 2.7). Initially, Húsmúli was intended to replace Gráuhnúkar as the primary reinjection site since the latter proved to have temperatures suitable for production, but it has encountered operational difficulties. The injection capacity has been declining, injectivity has been found to be heavily reliant on the temperature of the injected water, and seismic activity has been induced by injection. Therefore, further research is required to understand how the injectivity of the wells evolves and how they can be stimulated to improve and maintain their injectivity (Gunnarsson et al. 2015).

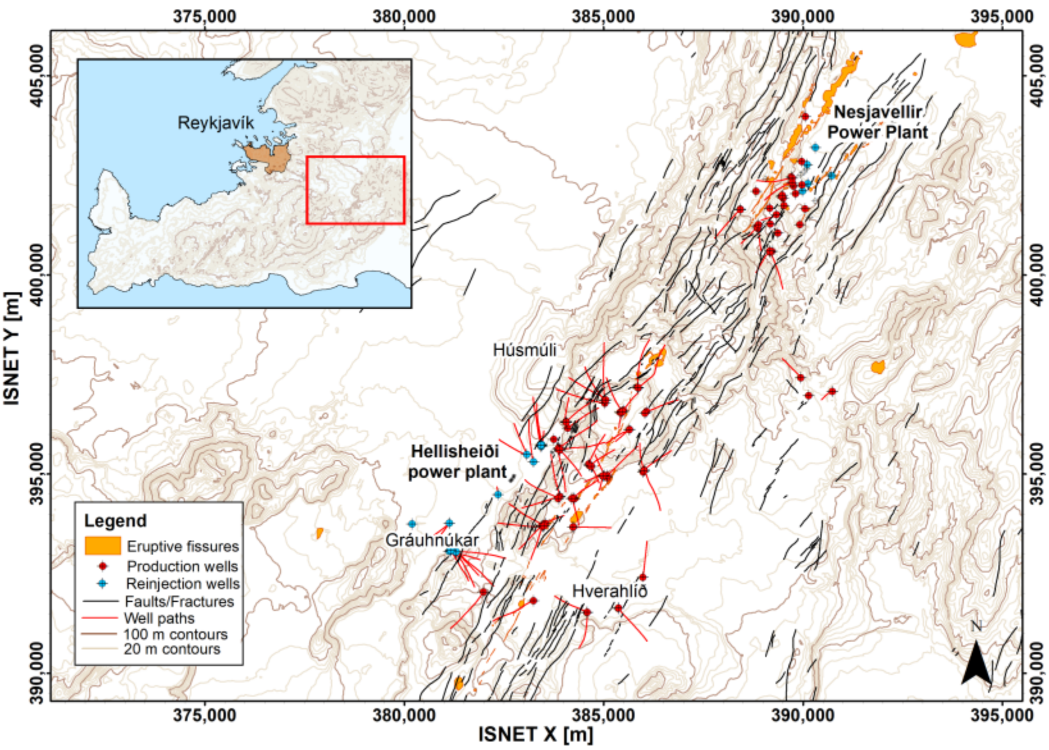

Figure 2.7: Location of Húsmuli and other reinjection areas. Source: Tómasdóttir (2018)

3
Fieldwork and Experimental Procedures

3.1. Fieldwork: seismic survey and sampling

During the summer of 2021, a field campaign was conducted in the area of interest as part of the SUCCEED project, with the main goal of acquiring seismic data to study the subsurface structures. Despite the challenging accessibility, two seismic lines were established to investigate the subsurface structures. The map in Figure 3.1 shows the configuration of the inline and crossline used for the seismic survey. An active seismic source was utilized to generate seismic waves, which were then recorded using fiber optics, three-component geophones, and wireless SmartSolo seismic sensors. The fiber optics cable was installed in a previous campaign along the inline. The geophones were distributed along a section in the northern half of the inline, while the SmartSolo sensors comprehensively covered both the inline and the crossline.

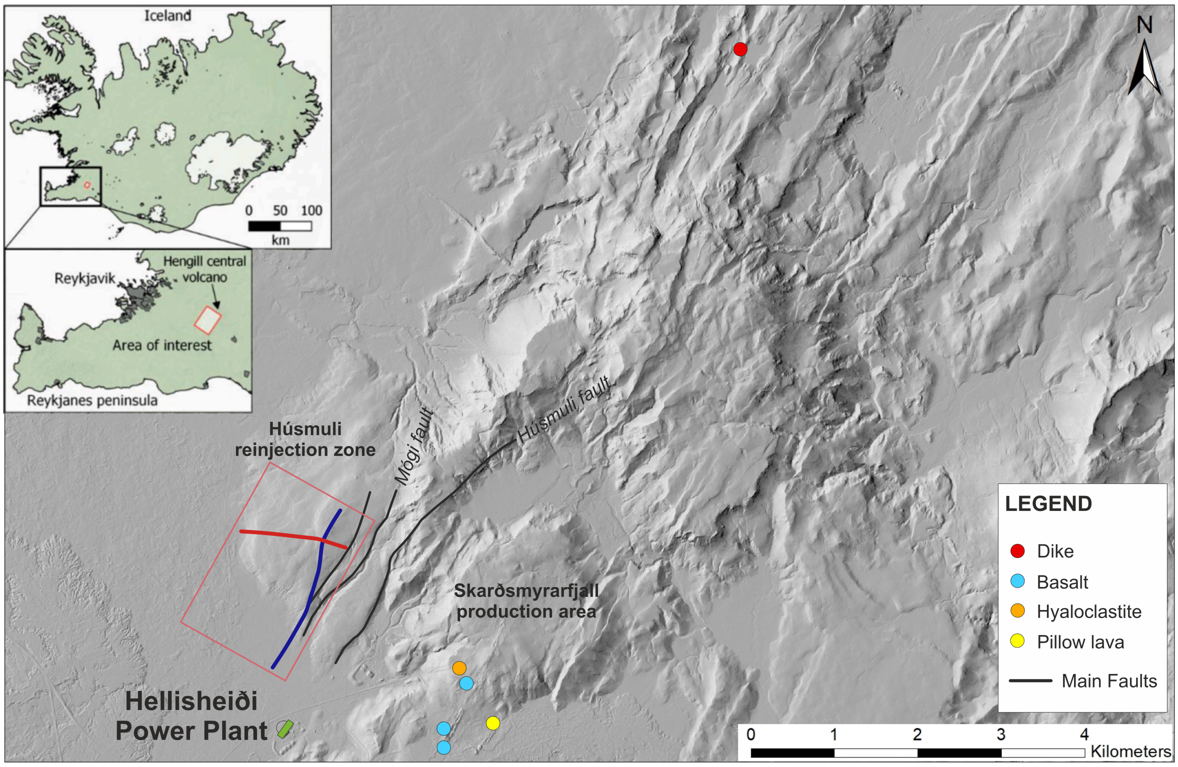

Figure 3.1: Topographical map of map of the vicinity of the Hellisheiði Power Plant and area of interest (red square). The blue and red lines are the established seismic lines, and correspond to the inline (IL) and crossline (XL) respectively. The locations where the samples where collected are marked with different colors depending on the lithology collected.

A series of samples were collected to serve two primary purposes: firstly, to subject them to laboratory analysis to determine their petrophysical and mechanical properties, and secondly, to study their acoustic properties in order to generate a velocity model for the future interpretation of the 2D seismic profiles. Given the heterogeneity of volcanic systems, a well-designed experimental study must first determine the most representative samples for addressing the objectives of the research. In this case, the goal was to gain an understanding of the mechanical behavior of rocks and to explore the factors that influence that behavior. In addition, due to the unavailability of cores or direct samples of rocks at depth, outcrops on the surface were sampled for analysis. This approach introduces significant uncertainty in the results since it is unclear whether the surface rocks accurately represent those in the reservoir. To address this issue, blocks characterized by different pore size and content, textures, and mineralogical composition were collected.

Great care was taken to ensure that the samples collected were of high quality and sufficiently diverse to enable comprehensive analysis. First, a visual reconnaissance survey of the different outcrops was conducted to identify the lithologies present in the area. Subsequently, the best outcrops were selected to sample rocks that were less altered by surface processes. The location of the sampled outcrops can be found in Figure 3.1. In some of the locations, more than one type of rock was collected since different characteristics were identified. The main geological formations that make up the subsurface of Húsmuli, as described in the literature, were identified in the outcrops and sampled: hyaloclastite, various types of basalts, and intrusive rocks (dikes). Although pillow lavas from specific levels within the hyaloclastites were sampled, their analysis has not been included in this study as they were found sporadically and considered not relevant for the research purposes. Figure 3.2 showcases some of the sampled outcrops.

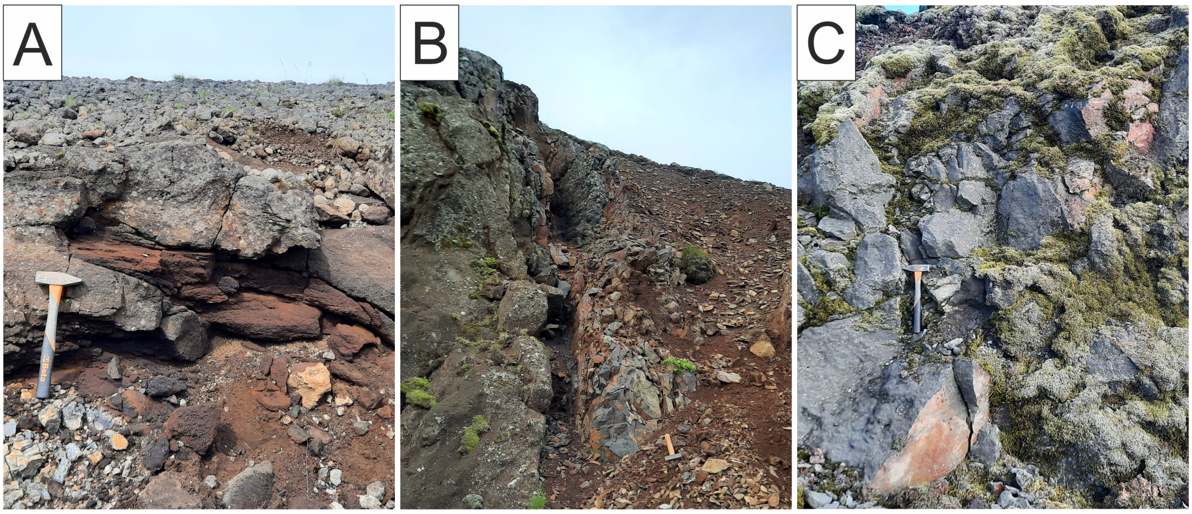

Figure 3.2: Outcrops sampled for hyaloclastite (A), dike (B) and basalt (C).

The sampled outcrops, as shown in Figure 3.1, are not located on the surface of the study area. This is due to the extensive weathering of the Húsmuli site, which has led to the surface being covered with moss and vegetation. In addition, the deposition of post-glacial lavas has further covered the outcrops, making them inaccessible. Because of that, the sampling was conducted in the NE-SW striking fissure swarm, and most of the samples were collected from outcrops situated in Skarðsmyrarfjall production area. The only exception was the dike, which was sampled further north near the Nesjavellir Power Station, which also produces geothermal water from this structure.

The methodology employed in this study was designed to ensure the collection of high-quality samples in a systematic and consistent manner. It was essential to collect samples that were large enough to extract adequate cores for subsequent laboratory testing. The first step in the process was to identify and collect the volcanic rock blocks from the outcrops. The coordinates of the outcrop were recorded using a GPS device, the approximate dimensions of the blocks were measured, and each block was given a unique sample code. To facilitate subsequent analysis and interpretation, pictures of the outcrops and the blocks were taken. The blocks were then wrapped in film to protect them from damage during transport, and all relevant information about each sample was recorded in a notebook, including a preliminary description.

3.2. Sample Preparation

The process of preparing the samples began with cutting the collected blocks using a saw to obtain fresh surfaces that allowed for the examination of their textures. After careful examination, the blocks were classified into different groups based on their texture. From each of these classified groups, one block was selected, resulting in a total of six blocks that included one hyaloclastite, one dike, and four basalts. In addition, a small gabbro block, which was provided by Dr. Karl-Heinz Wolf as an analogue of the crystalline rocks that can be found at the base of the Hengill volcano, was also included.

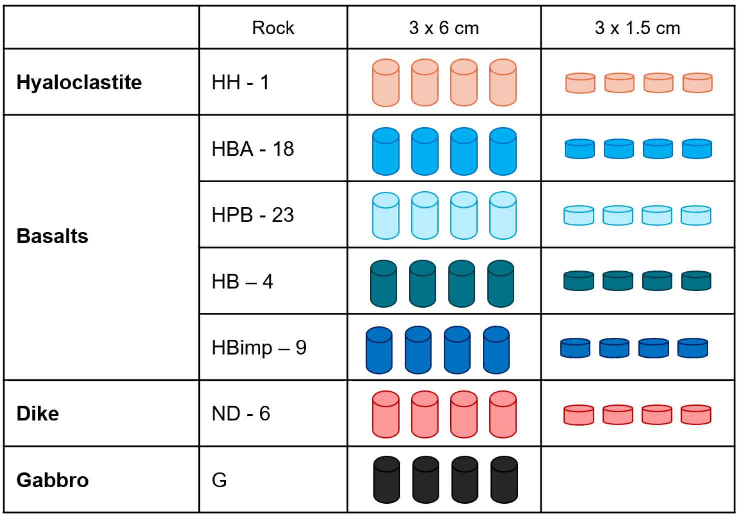

Figure 3.3: Prepared rock samples for laboratory testing. Samples were obtained by drilling and cutting rock cylinders of various sizes from six different blocks, including hyaloclastite, dike, basalts, and a gabbro analogue. The color code used for each sample will be used consistently throughout the report to display the results.

To ensure representative results, four cores per laboratory test and block were extracted. The size of these cores ranges from 1.5 millimeters (mm) in length with a diameter of 30 mm to 60 mm in length with a diameter of 30 mm. To obtain the desired sample sizes, rock cylinders with a diameter of 30 mm were drilled and extracted from each block. Unfortunately, the gabbro block was too small to extract samples of 30 x 15 mm. The names of the prepared samples are presented in Figure 3.3. Throughout the sample preparation process, the heterogeneity of the texture within each block was considered to ensure that the cores obtained represented the different variations present in the original block. The cylinders were then cut using a saw, ensuring that both ends of the samples were parallel. The drilling and cutting of the rock cylinders required the use of water during the process to prevent overheating of the samples. As a result, the samples were soaked and needed to be dried before testing. To achieve this, the samples were placed in an oven at 40 °C for a minimum of 48 hours to ensure that they were completely dry before testing.

3.3. Petrophysical parameters

3.3.1. Porosity and Bulk Density determination

The porosity of each core sample was determined using a helium pycnometer, a device that measures porosity by monitoring the change in pressure of helium gas within a calibrated volume. Gas is used as the displacing fluid in the pycnometer because it can penetrate even the finest connected pores. The resulting matrix volume obtained from the helium pycnometer includes not only the actual matrix volume but also the volume of pores that are not connected. In subsequent chapters, both connected and non-connected porosity will be taken into account when describing the porous system. The measured porosity will be the value used to perform calculations that relate geomechanical and petrophysical parameters.

The bulk density of the rock samples was determined by calculating the ratio of the mass of the sample to its bulk volume, which was estimated by assuming that the sample is a perfect cylinder and measuring its dimensions using a caliper. It's important to note that the density calculation relies on the assumption that the sample is homogeneous and without any voids or cracks. In reality, rocks often contain pores, cracks, and other types of heterogeneities that can affect the density calculation. However, for the purpose of this study, these effects were ignored and the bulk density method was used to determine the density of the rock samples.

3.3.2. Permeability

To accurately measure the permeability of the rock cores, the Ruska Gas Permeameter is utilized. This tool uses gas to measure permeability by monitoring the pressure drop and temperature of the gas as it flows through the core. The rock core samples used in this experiment have precise dimensions of 30 mm in diameter and 15 mm in height. To prevent gas from flowing outside the core during the experiment and ensure accuracy, each core is fitted with a rubber sleeve. Three pressure drops, 0.25, 0.5, and 1 atmosphere, are used in the experiment to obtain the permeability value using Darcy's Law, which utilizes the length and diameter of each core. However, the pore size distribution makes it impossible to measure all pressure drops in all samples. In some samples with a preferential flow path or excessively large pore size, the measured permeability is beyond the range of the instrument. For other samples, permeability was below the range of the instrument. In these cases, it will be noted that the permeability is higher or lower than the instrument's measurable limits. It should be noted that Darcy's Law is typically used to determine permeability in liquid flow, not gas flow. Therefore, the permeability values obtained may be overestimated due to gas slippage in small pores, also known as the Klinkenberg effect (Klinkenberg 1941).

3.3.3. MicroCT Image Processing and Analysis

The amount and characteristics of the pore fraction in rocks can have an impact on their mechanical behavior when subjected to stress conditions. Microcomputed tomography (micro-CT) experiments with 3D image analysis are an additional technique for analyzing porosity. This imaging method involves capturing hundreds to thousands of X-ray projection images at various angles of rotation around a specimen. As X-ray radiation passes through the sample, it is absorbed to varying degrees depending on the densities of different parts of the object. Each analysis method has its advantages and limitations. Coletti et al. (2016) compared micro-CT results with those obtained from three other porosity characterization methods, focusing on total porosity and pore size ranges. They concluded that using a variety of techniques can provide a more comprehensive characterization of the pore system, as no single method can completely describe the entire range of pore sizes. Bugani et al. (2007) pointed out the challenge of comparing results between different porosity characterization methods. Instead of another multi-technique comparison, this study highlights the strengths of using micro-CT coupled with 3D image analysis for characterizing the pore fraction of volcanic rocks. The limitations of this approach are also discussed.

In this study, the porosity of samples measuring 30 mm in diameter and 60 mm in length was analyzed using micro-CT scans with a resolution of 60 micrometers. The software Avizo© was employed to determine the total porosity, as well as connected and unconnected porosity. The software DragonFly© was utilized to measure the pore-wall surface and plot the pore size distribution of connected and unconnected porosity for all the samples.

Figure 3.4 shows the workflow followed in Avizo. The first step in the analysis involves importing the files generated during sample scanning into Avizo and visualizing a 3D image of the sample (image 1). To avoid including pores from the rock surface in the analysis, a prism is cropped from the interior of the rock (images 2 and 3). The next step is to apply a median filter and unsharp masking filters (figures 4 and 5). The median filter is a type of image filter used to reduce noise in a dataset. It is

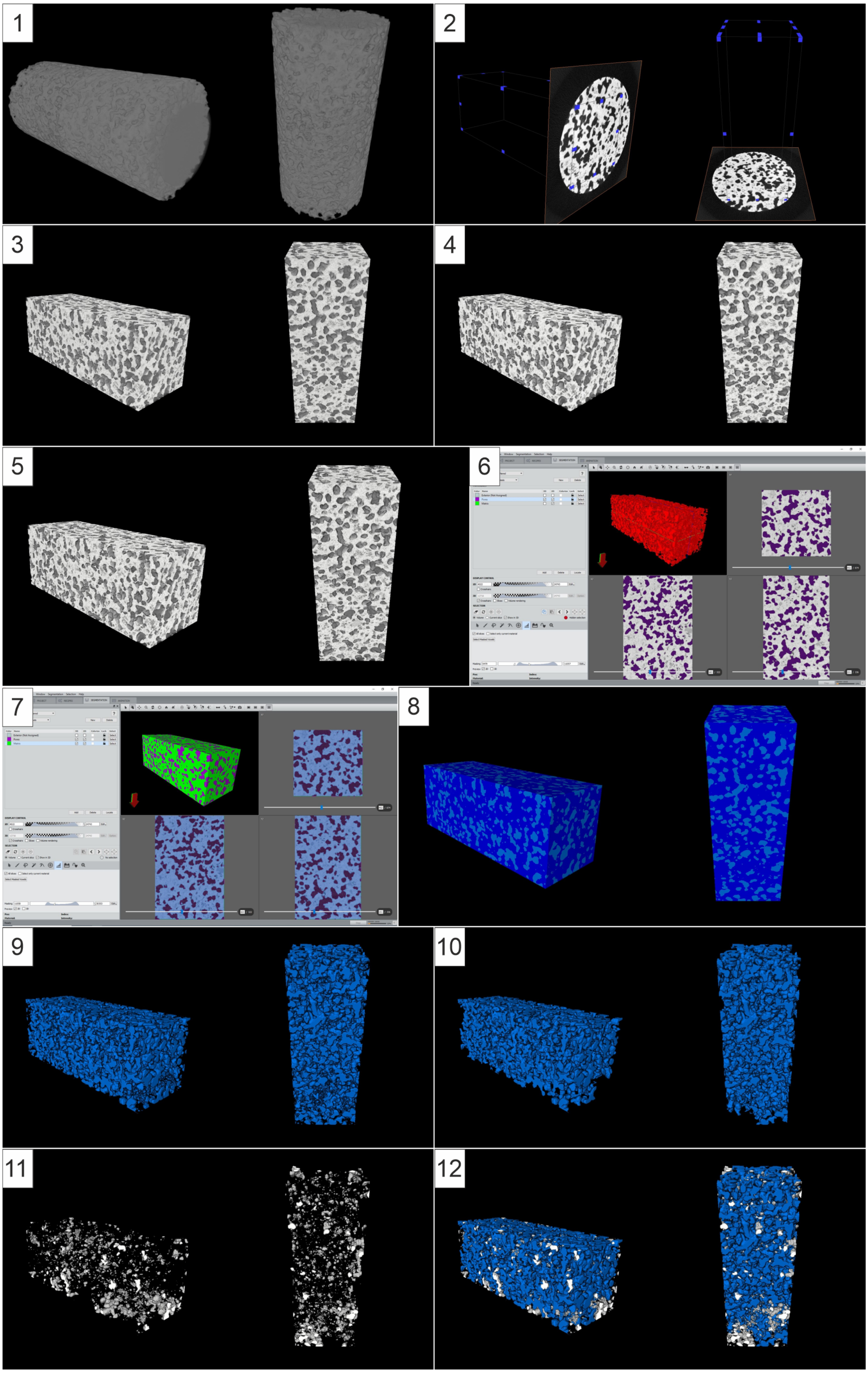

Figure 3.4: Workflow of Image Analysis of a MicroCT Scan (sample HPB-23-B). This figure illustrates the 12 steps involved in the image analysis process, from the import of the raw data to the final segmentation of the regions of interest.

applied to 3D images and replaces each voxel value in the image with the median value of the voxels within a given neighborhood (in this case, 6 voxels). By doing this, the median filter can smooth out small variations in intensity and remove small speckles from the image while preserving the edges and details of the object. The unsharp masking filter, on the other hand, is an image processing technique used to enhance the edges and details of an image. This technique involves creating a blurred version of the original image and then subtracting the blurred version from the original image to produce a high-pass filtered image. This high-pass filtered image is then added back to the original image to create the final sharpened image. This technique improves the quality of micro-CT images, making it easier for software to distinguish between different features within the sample. After filtering and enhancing the image, two fields are selected to separate the matrix from the porosity, which is done by manually selecting a threshold (images 6 and 7). Once selected, the different fields are established (image 8). From this point, the porosity field can be isolated and displayed in 3D (image 9). The connected and non-connected porosity can be filtered using the Axis Connectivity tool, in this case, the connected porosity was extracted along the X-axis of the sample (from top to bottom). At this point, the connected porosity (image 10) and non-connected porosity (image 11) can be visualized separately or together (image 12). Quantitative data on the different porosities analyzed were exported from each of the files generated in each step of the process and analyzed in Excel.

After visualizing the connected and unconnected porosity fields separately, .tiff files were exported and subsequently imported into DragonFly© for analysis. Once imported into this software, the analyzed sample can be visualized with the matrix and porosity fields already differentiated. These fields are selected again, and from them, the pore-wall surface can be computed and the pore size distribution can be plotted. The data can then be exported and analyzed in Excel.

3.4. Determination of the Geomechanical Properties

3.4.1. Unconfined Compression and Active-source acoustics Test

The Unconfined Compression Test (UCS) is used to derive the unconfined compressive strength of a rock specimen, which stands for the maximum axial compressive stress that a specimen can bear under zero confining stress. In addition to measuring axial load, this test also measures axial and radial strain, which is used to calculate the sample's Young's modulus and Poisson's ratio. Figure 3.5 shows a scheme of the experimental setup. In this type of experiment, a cylindrical sample of 30 mm

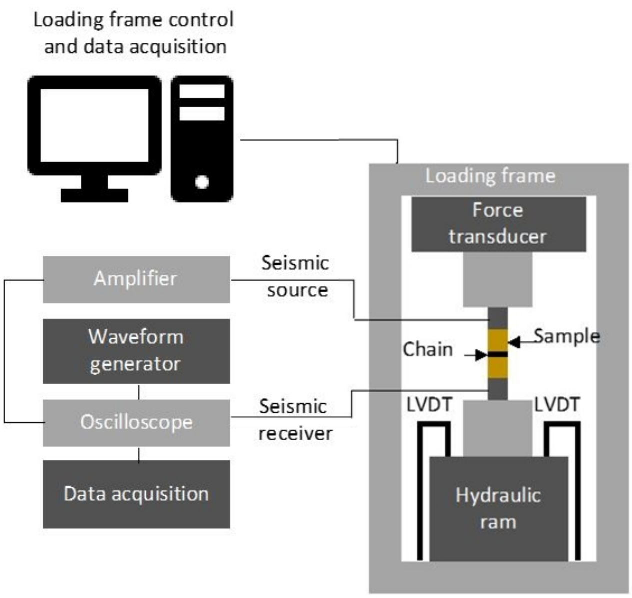

Figure 3.5: Experimental set-up for UCS experiment. LVDT stands for linear variable differential transducer. Modified from Janssen et al. 2021.

in diameter and 60 mm in height is positioned between two steel pistons. The first piston moves consistently, which leads to the deformation of the sample at a steady strain rate of 10^{-5} s^{-1}. Alternatively, the movement continues until the sample fails macroscopically. During the test, P- and S- wave velocities are also measured using sensors placed inside metallic cups in contact with the top and bottom of the sample. The acoustic parameters used are listed in Table 3.1. The metallic cups are carefully chosen to be made of steel to prevent permanent deformation of the cups and the setup. All tests have been performed at room temperature and both acoustic and steel strain calibration for the axial strain corrections have been done to obtain more accurate results.

Frequency	Amplitude	Offset	Waveform	Burst
1 MHz	800 mVpp	0	Sine	5 ms

Table 3.1: Parameters and settings of acoustic generator for active-source acoustic testing on rock samples

Steel Strain Calibration

To calibrate the strain of the steel pieces used in the set-up, an unconfined compression test was performed on a steel cylinder with the same dimensions as the rock samples. Since the steel cylinder has its own inherent strain value, this value can be subtracted from the total strain measured in the test set-up with the rock samples. The left side of Figure 3.6 illustrates this process. To obtain accurate strain values of the rock samples, the strain values of the set-up were plotted to generate both linear and polynomial correction functions. These functions will be applied to the collected data based on the applied stress, resulting in corrected axial strain values of the rock samples. The purpose of this calibration is to subtract the corresponding strain of the set-up from the total strain measured in the test, enabling the accurate measurement of the deformation of the rock samples.

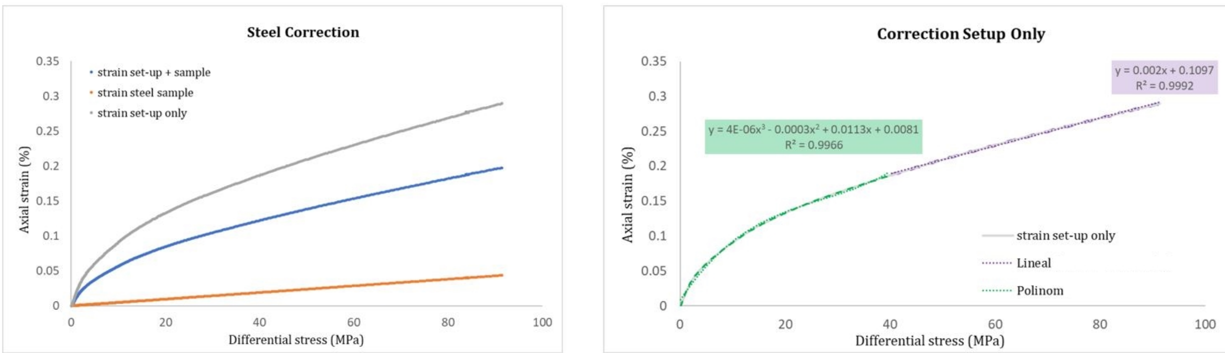

Figure 3.6: Steel Strain Calibration Plots obtained from an Unconfined Compression Test performed on a steel dummy.

Acoustic Calibration

In order to obtain accurate first arrival times, the wave acoustic velocities must be corrected due to the presence of steel cups surrounding the source and receiver, as previously mentioned. The thickness of the steel that the waves pass through needs to be calibrated to ensure accurate measurements. To achieve this, the first arrival times of the P and S waves were plotted under varying stresses, as shown in Figure 3.7. The time taken for the waves to pass through the metallic end-caps is then subtracted from the total time it takes for the wave to propagate from the source to the receiver. In addition, the strain of the sample is accounted for in the calculations as it shortens under increasing load. This allows the velocity at which the waves pass through the sample to be calculated as a function of stress, ensuring accurate measurements.

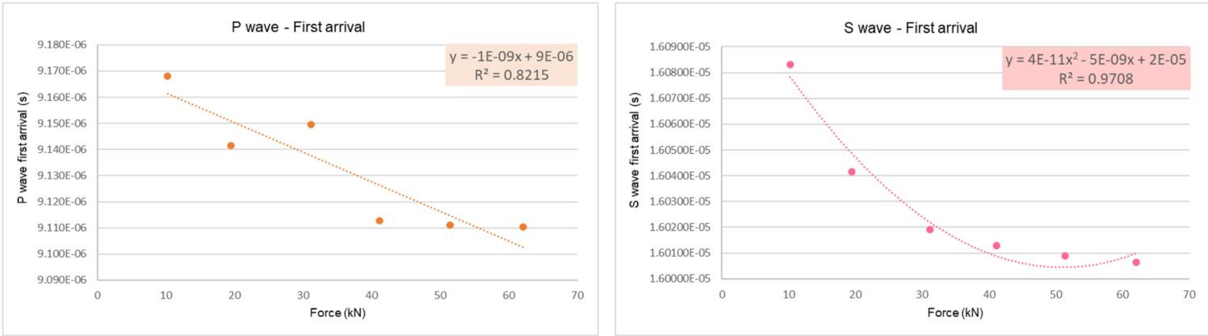

Figure 3.7: Steel Acoustic Calibration for P and S wave first arrivals through a steel dummy.

3.4.2. Splitting Tensile Strength Test (Brazilian)

The Brazilian Test is a widely used method for determining the tensile strength of rock samples. In this test, cylindrical samples with a diameter of 30 mm and a height of 15 mm are prepared and placed between two hardened steel platens. The contact surfaces of these platens feature a semicircular groove that acts as a stress concentrator. A compressive load is applied to the sample through the platens, causing the sample to split diametrically along the semicircular groove. In this experiment, the movement of the pistons is constant at a steady strain rate of $10^{-5}\,\mathrm{s}^{-1}$. The tensile strength of the rock sample is calculated based on the magnitude of the applied load and the dimensions of the rock sample. A scheme of the experimental setup is shown in Figure 3.8.

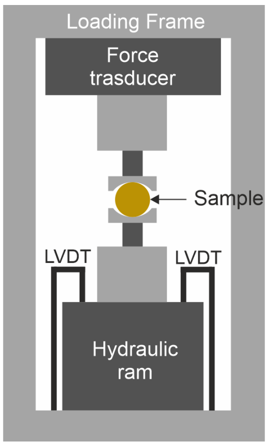

Figure 3.8: Experimental set-up for the Brazilian experiment. LVDT stands for linear variable differential transducer.

3.5. Thermal Shock Test

As previously described in Chapter 2, the Húsmuli geothermal system is utilizing reinjection of geothermal water with dissolved CO2 at a temperature of 60ºC to enhance its productivity, while the reservoir itself is at a temperature between 260ºC and 285ºC. This rapid cooling of the reservoir due to the injection of cool water can generate thermal stresses, which may result in the formation of cracks and fractures in the rock matrix, thereby impacting the permeability of the reservoir. This could potentially increase the capacity for CO_2 storage, but also lead to more rapid cooling of the reservoir. Although the Húsmuli system is predominantly fracture-driven, the current study aims to investigate the potential impact of a thermal shock on the primary porosity of the reservoir rocks.

Laboratory experiments have been conducted to investigate the impact of rapid cooling on rock damage. To simulate the injection of colder fluids into a higher-temperature reservoir, the samples are gradually heated to the desired temperature and then rapidly brought back to the target temperature. This process is commonly known as thermal shock (Bellopede et al. 2006). In this study, thermal shock experiments were performed on samples of 30 mm diameter and 60 mm height of HBimp-9 basalt, which has similar textural characteristics to those observed in CarbFix mineralized CO_2 basalt cores reported in the literature. Furthermore, the petrophysical and mechanical characteristics resulting from previous tests on all rocks included in this study suggest that this type of basalt is more likely to be found at similar depths as the main feed zones in Húsmuli compared to the other basalts.

Before conducting the thermal cracking experiment, a control group consisting of 4 samples was established, on which all tests included in this study were performed without subjecting the samples to thermal shock. Subsequently, another 4 samples from the same block were selected as the Thermal Shock group, and their porosities were measured using the helium pycnometer before subjecting them to thermal shock. The experimental setup is shown in Figure 3.9. The samples were placed in an oven and gradually heated to 270ºC, then maintained at this temperature for 48 hours before being quickly extracted and immersed in a tank of water at a constant temperature of 60ºC. The process was carried out carefully, without hitting the samples, so that the possible generation of fractures was conditioned only by the thermal shock. Afterward, the samples were extracted from the tank, and their temperature was measured to confirm cooling to 60ºC. After completing the experiment, the samples' porosity was measured again, and they were subjected to UCS testing. The results were later compared to the values obtained before the experiment and to those obtained by the control group.

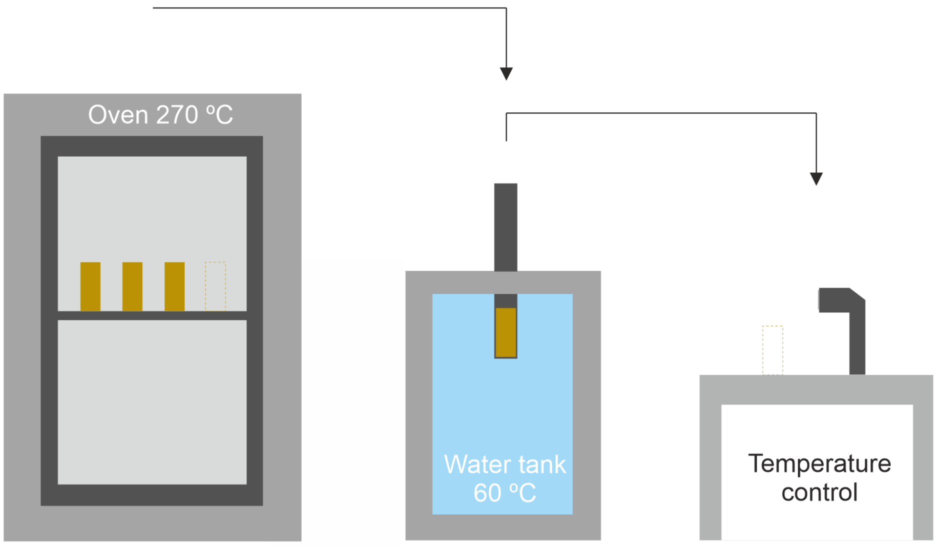

Figure 3.9: Experimental set-up for the Thermal Shock experiment.

4
Results

4.1. Petrophysical study

4.1.1. Porosity, Bulk density and Permeability

The porosity values of various rock samples were analyzed using a helium pycnometer, which provided the measurements of the effective porosity displayed in Figure 4.1. It is worth noting that the measurement of effective porosity using this method included the pores located on the surface of the samples as part of the connected porosity. However, it is possible that some of these pores may not be connected *in situ*, meaning that the effective porosity values may have been overestimated to some degree. Despite this potential limitation, the porosity values were found to be consistent across all samples of the same rock type, indicating that the method was reliable for comparing porosity values within a given sample set.

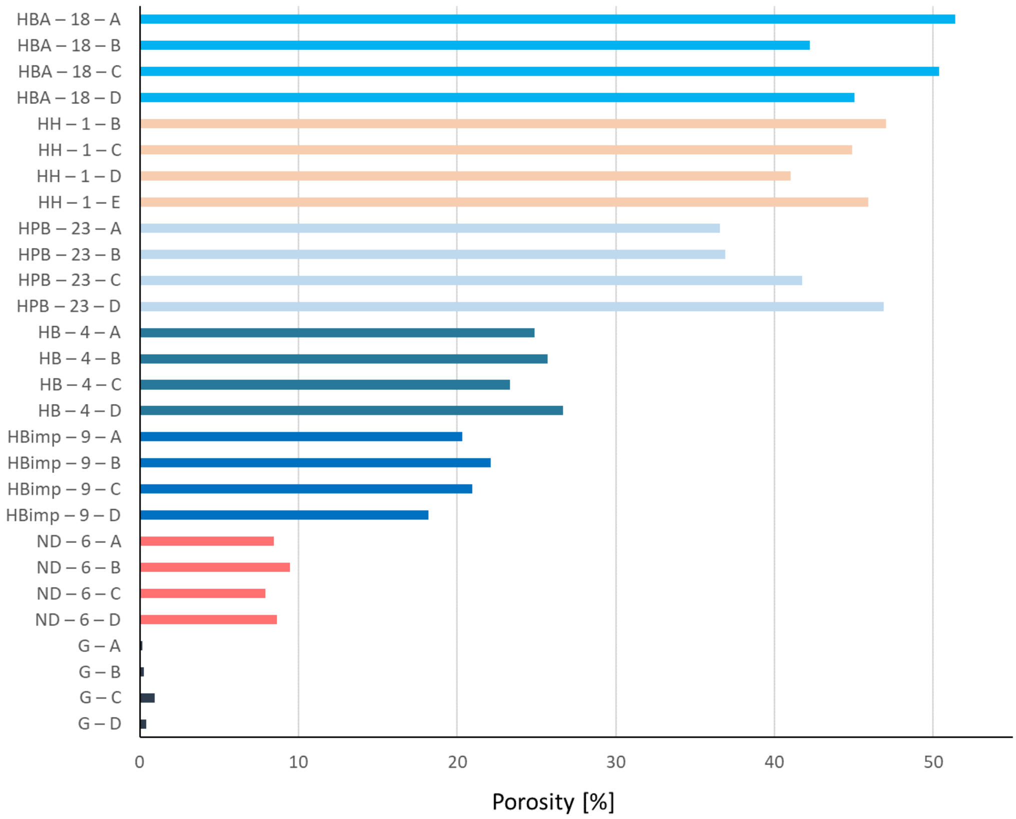

Figure 4.1: Porosity values (in percentage) of seven different rock types, with four samples per rock type. Different studied rock materials are distinguished by colors: orange: hyaloclastite; red: dike; black: gabbro; blue: basalts.

The basalt HBA-18 exhibits the highest porosity values, ranging from 42.20% to 51.37%. The hyaloclastite HH-1 has a porosity range of 40.99% to 47.03%, followed by the basalt HPB-23 with values between 36.54% and 46.87%. The basalt HB-4 has a porosity range of 23.34% to 26.66%, while the basalt HBimp-9 ranges between 18.19% and 20.31%. The samples with the lowest porosity are the dike ND-6, with a porosity range of 7.90% to 9.45%, and the gabro G, with values between 0.18% and 0.92%. Overall, minimal variation in porosity was observed across most samples (Figure 4.2). HPB-23, HBA-18, and HH-1, displayed slightly higher variability. HB-4 and HBimp-9 were found to exhibit very similar porosity values, while ND-6 and G showed the least variability. Of note, ND-6 and G have different type of porosity than the other samples, these have secondary porosity. ND-6 exhibited small, visually identifiable fractures of varying orientations and lengths, while G displayed porosity that may be attributed to micro-fractures that are not discernible or discontinuities between phenocrysts.

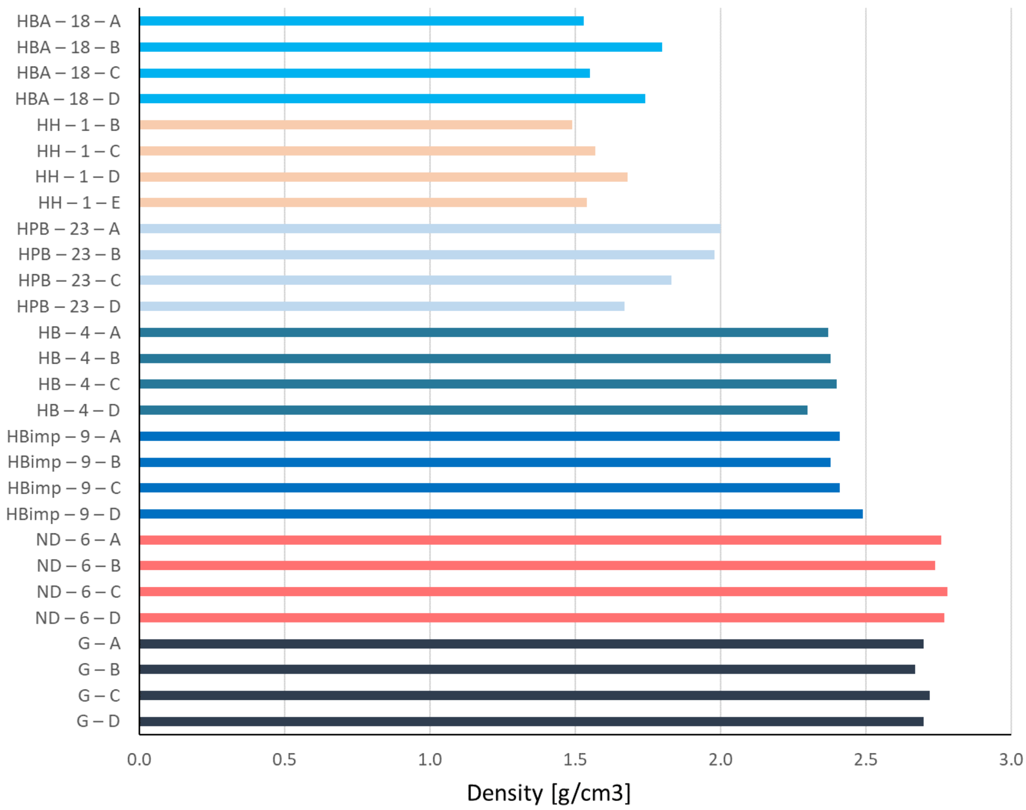

Figure 4.2: Bulk density values (in g/cm^3) of seven different rock types, with four samples per rock type. Different studied rock materials are distinguished by colors: orange: hyaloclastite; red: dike; black: gabbro; blue: basalts.

Through an analysis of the porosity measurements and volume of the samples, the bulk densities of the samples were determined. The rock with the highest density among all the studied rocks is the dike ND-6 with a density ranging from 2.74 to 2.78 g/cm^3. Following closely is the analogue gabbro G with a density between 2.67 and 2.72 g/cm^3. Basalts HBimp-9 and HB-4 have densities that range from 2.38 to 2.49 g/cm^3 and 2.30 to 2.40 g/cm^3 respectively. The density of basalt HPB-23 ranges from 1.67 to 2.00 g/cm^3. The less dense basalt is HBA-18 with values ranging from 1.53 to 1.8 g/cm^3. The rock with the lowest density among all the studied rocks is the hyaloclastite HH-1 with values ranging from 1.49 to 1.68 g/cm^3.

The Ruska permeameter was used to measure the permeability of the different sets of rock samples. The results for some samples are contained in Figure 4.3. The basalt HBA-18 has a permeability that

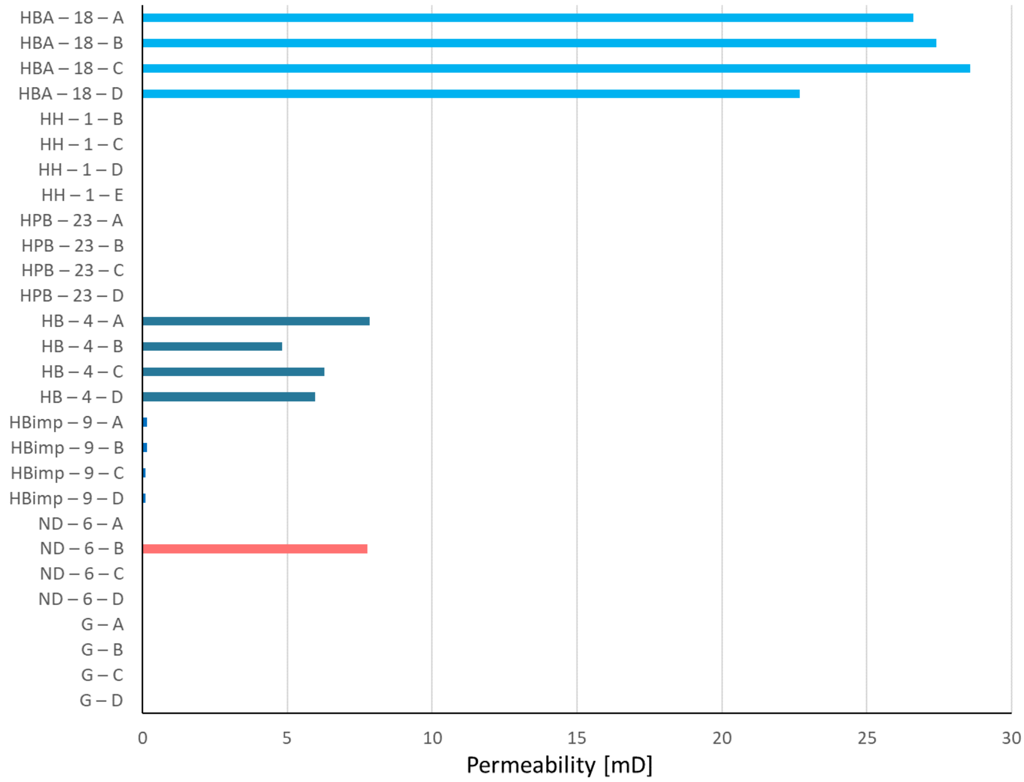

Figure 4.3: Permeability values measured with the Ruska permeameter. The permeability of HH-1 and HPB-23 are above the range of measurement. The permeability of G and most samples of ND-6 are below the range of measurement. Therefore, the permeability values for these rocks have not been determined. Different studied rock materials are distinguished by colors: orange:red: dike; black: gabbro; blue: basalts.

ranges between 22.70 and 28.58 mD. The permeability for HB-4 oscillates between 4.82 and 7.86 mD. The basalt with the lowest measured permeability is HBimp-9 with values between 0.11 and 0.17 mD. In just one sample of four, the permeability of dike ND-6 has been measured, and for this sample, a permeability of 7.76 mD has been obtained. However, limitations in the measurement range made it impossible to obtain results for certain samples. Notably, values above 33 mD or below 0.03 mD were outside the measurement range of the Ruska permeameter and therefore could not be assessed. Specifically, the HPB-23 and HH-1 sample permeabilities were above the measurement range, while G and most of the ND-6 samples were below. For those samples where permeability could be measured, the results were consistent and exhibited low variability. Regarding the HH-1 samples, it is worth noting that the unconsolidated nature of the material may have influenced the final permeability measurement. Specifically, the morphology of the sample and the placement into the rubber sleeve may have led to gas flow between the sample and the sleeve, potentially affecting the accuracy of the measurement. Despite efforts to improve the experimental procedure, the poor quality of the sample and its limited capacity to remain intact during manipulation prior to the experiment made it difficult to obtain a more precise measurement.

The permeability values for sample ND-6-B were determined, but it should be noted that the results may not be representative of the rock due to the presence of small fractures. Fluids flowing through these fractures may not accurately reflect the overall permeability of the rock, resulting in a high level of uncertainty in the measured values. Similar to the observed trend in porosity, the variability of permeability is greater for HBA-18 and decreases for HB-4, with very low variability for HBimp-9.

Table 4.1 displays the mean values of porosity, bulk density, and permeability for each of the four sample sets of every rock type.

	HBA - 18	HH - 1	HPB - 23	HB - 4	HBimp - 9	ND - 6	G
Porosity [%]	46.38	44.68	40.34	24.99	21.53	8.71	0.44
Bulk density [g/cm3]	1.68	1.56	1.87	2.36	2.38	2.76	2.7
Permeability [mD]	26.33	>33	>33	6.23	0.14	<7.76	-

Table 4.1: Porosity, permeability and bulk density averages per rock type.

4.1.2. MicroCT scan analysis

In Figure 4.4, the seven samples scanned with the microCT can be observed along with their corresponding microCT scans. The scans were performed at a resolution of 60 μm. The samples are presented from left to right according to their porosity, with the least porous sample being located on

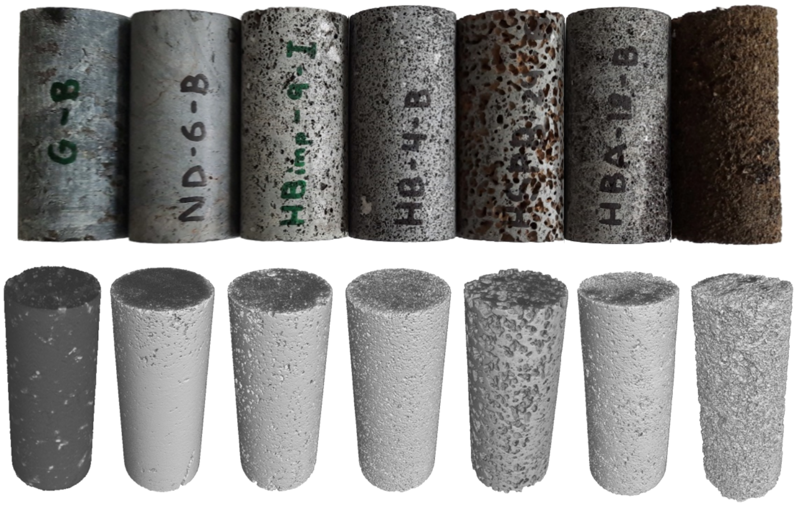

Figure 4.4: MicroCT scans visualization images (bottom) and reference sample picture (top).

the far left and the most porous sample on the far right. It is noticeable that there are visible differences in porosity among the samples, mainly in terms of size and distribution of pores. Moreover, the colors of the samples and the presence of phenocrysts are also evident, with some samples exhibiting these features. This gives an insight of the varying mineral compositions of the matrices in the different samples.

During the image analysis, several differences in pore size and distribution were observed, this be can easily observed in Figure 4.5 and Table 4.2. As outlined in Chapter 3, the scans were cropped into prism-shaped volumes. These new volumes, ranging from 17.46 cm^3 to 22.28 cm^3, contain the following permeability values. The highest porosity measured using this technique was observed in the

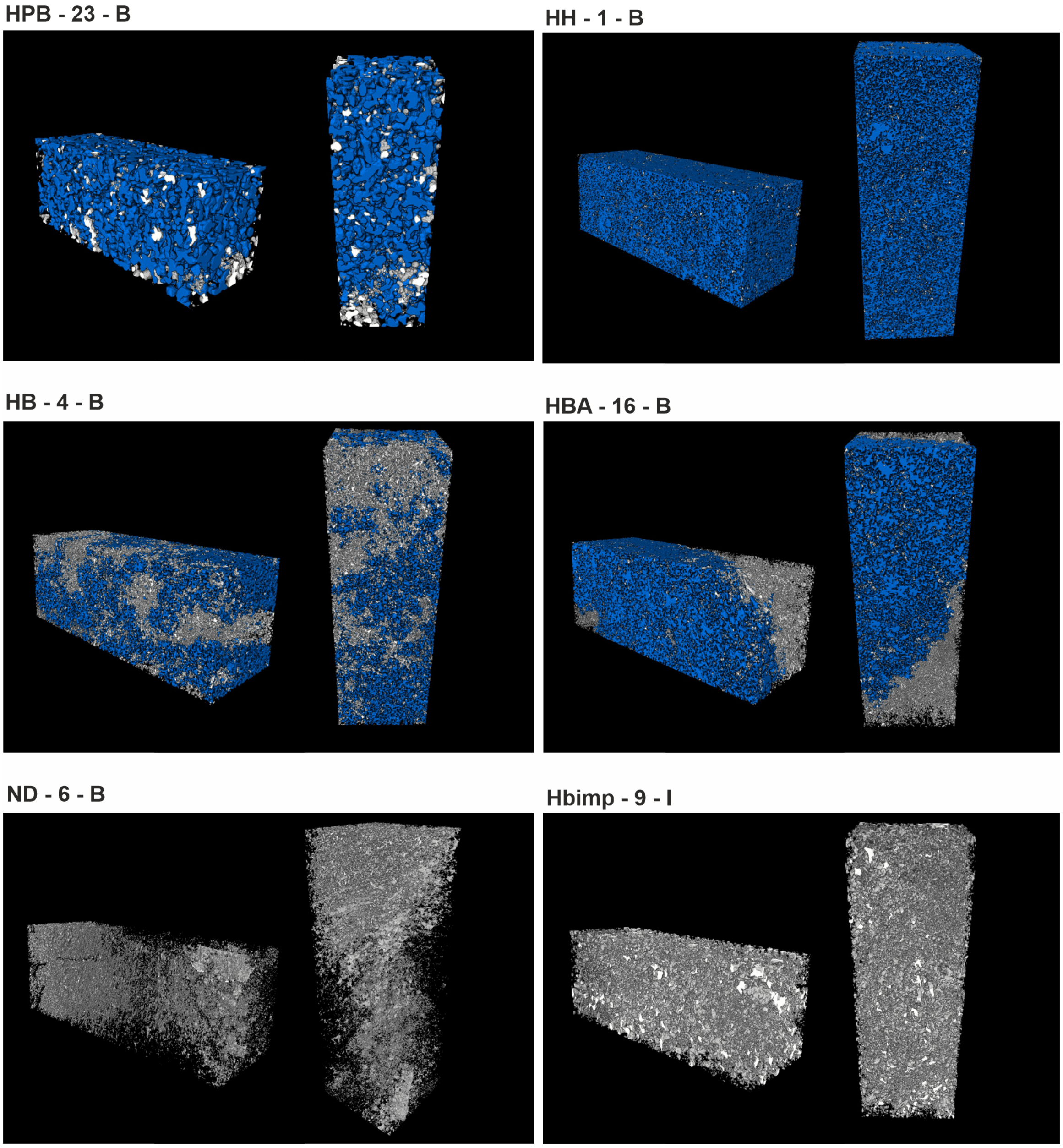

Figure 4.5: Pore-structure visualization from microCT scans (resolution of 60 μm). Connected porosity in blue, unconnected porosity in white.

hyaloclastite HH-1-B, with a value of 32.25%. This was followed by basalt HPB-23-B at 29.06% and basalt HBA-18-B at 22.61%. Basalt HB-4-B exhibited a porosity of 19.16%, while basalt HBimp-9-I had a porosity of 13.19%. The dike ND-6-B had the lowest porosity, with a total of 2.68%. Interestingly, the G-B sample did not show any porosity above 60 μm, although some porosity was actually measurable using the helium pycnometer.

The percentage of unconnected porosity from each sample's total porosity varies. The HBimp-9-I and ND-6-B samples only exhibit unconnected porosity above 60 μm, while the other four samples show different proportions of connected and unconnected porosity. According to the data, the hyaloclastite HH-1-B exhibits a connected porosity of 31.66% and a relatively low percentage of unconnected pores at 0.56%. The connected porosity of HPB-23-B is slightly lower at 27.91%, with unconnected porosity measuring at 1.15%. HBA-18-B displays a connected porosity of 19.23%, while the percentage of unconnected pores is relatively high at 3.36%. For HB-4-B, the connected and unconnected porosity values are 15.98% and 3.18%, respectively.

	Cropped Volume [cm^3]	Pycnometer Φ [%] *	Total Φ [%]	Connected Φ [%]	Unconnected Φ [%]	Surface of connected pores [cm^2]	Surface of unconnected pores [cm^2]
ND – 6 – B	23.28	8.44	2.68	0	2.68	0	132.96
HBimp – 9 – I	21.90	21.8	13.19	0	13.19	0	297.24
HBA - 18 – B	22.09	42.2	22.61	19.23	3.38	499.12	150.12
HB – 4 – B	21.49	25.71	19.16	15.98	3.18	478.12	135.97
HPB – 23 – B	19.07	36.89	29.06	27.91	1.15	213.01	18.47
HH – 1 – B	17.46	47.03	32.25	31.68	0.56	787.63	29.90

* In sample volume of 42.4 cm^3.

Table 4.2: Summary Table of microCT scans analysis results.

The generated pore-size distributions allow for the quantification of the differences between the samples, shown in Table 4.2. In order to have a graphical representation of the pore-size distribution, these distributions have been plotted for both connected and unconnected porosity in Figures 4.6 and 4.7.

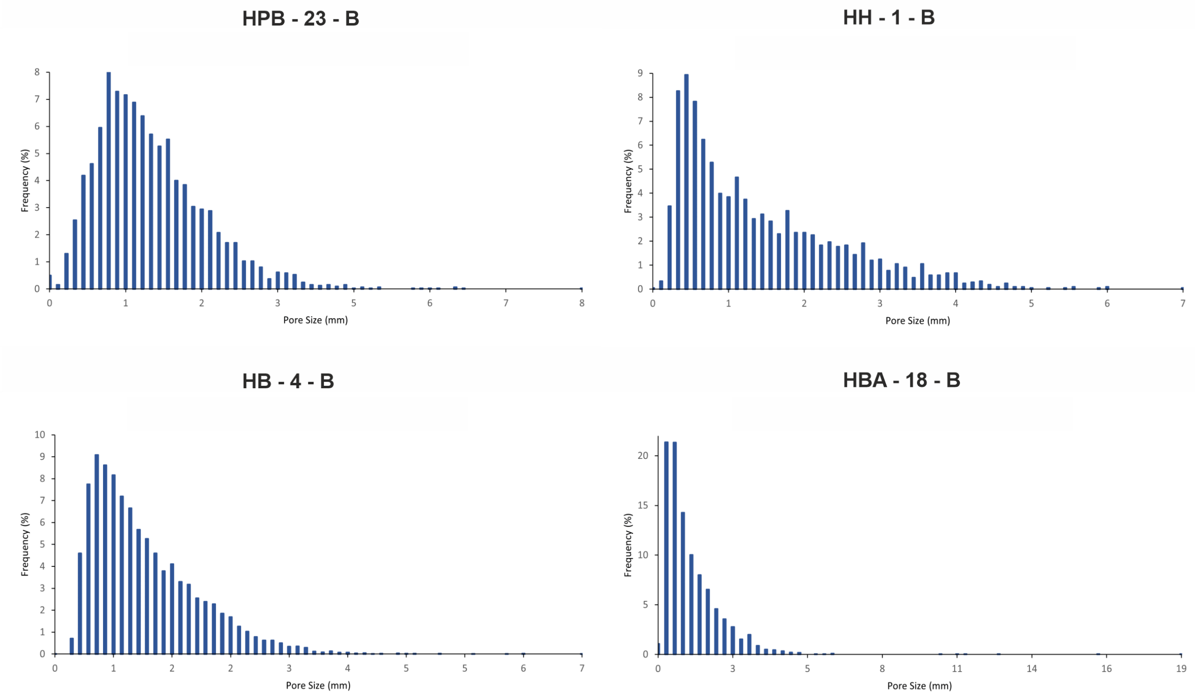

Figure 4.6: Pore-size distribution of connected porosity.

The pore-size distribution plots of unconnected porosity generally show a log-normal distribution. However, the HPB-23 sample has a high number of outliers above and below the mode value. In contrast, the plot of pore-size distribution of connected porosity for the same sample shows a log-normal distribution with very few outliers. Additionally, the plots of the pore-size distribution of connected porosity generally show a log-normal distribution, except for HBA-18, which exhibits an exponential distribution. The HH-1-B sample's distribution is log-normal but tends to resemble an exponential distribution.

Since the hyaloclastite HH-1-B is an unconsolidated material and the dike ND-6 has secondary porosity instead of primary porosity, the focus will be solely on the basalt samples for comparison purposes. The graphs reveal that the HPB-23-B basalt sample displays the highest pore-size values, for both connected and unconnected porosity, compared to the other basalt samples. The connected porosity has a mode value of 0.90 mm, while the unconnected porosity has a mode value of 0.94 mm. Additionally, the pore-size heterogeneity of the unconnected pores in this sample is much greater than that of the connected pores. The unconnected porosity of this sample has a higher number of small and large pores than the connected porosity. The HB-4-B basalt sample comes next, but with a significant gap from the previous one. The mode value for connected porosity is 0.56 mm, and for unconnected porosity, it is 0.79 mm. Interestingly, the difference in size of the most abundant pore between the two porosities is quite large. Additionally, the heterogeneity of pore size is greater for the unconnected porosity in this rock as well. The HBA-18-B basalt has a mode value of 0.30 mm for connected porosity and 0.75 mm for unconnected porosity. This indicates a significant increase in the difference between the most prevalent pore size for connected and unconnected porosities for this sample. The HBimp-9-I sample, which only exhibits connected porosity, has a pore-size mode value of 0.72 mm.

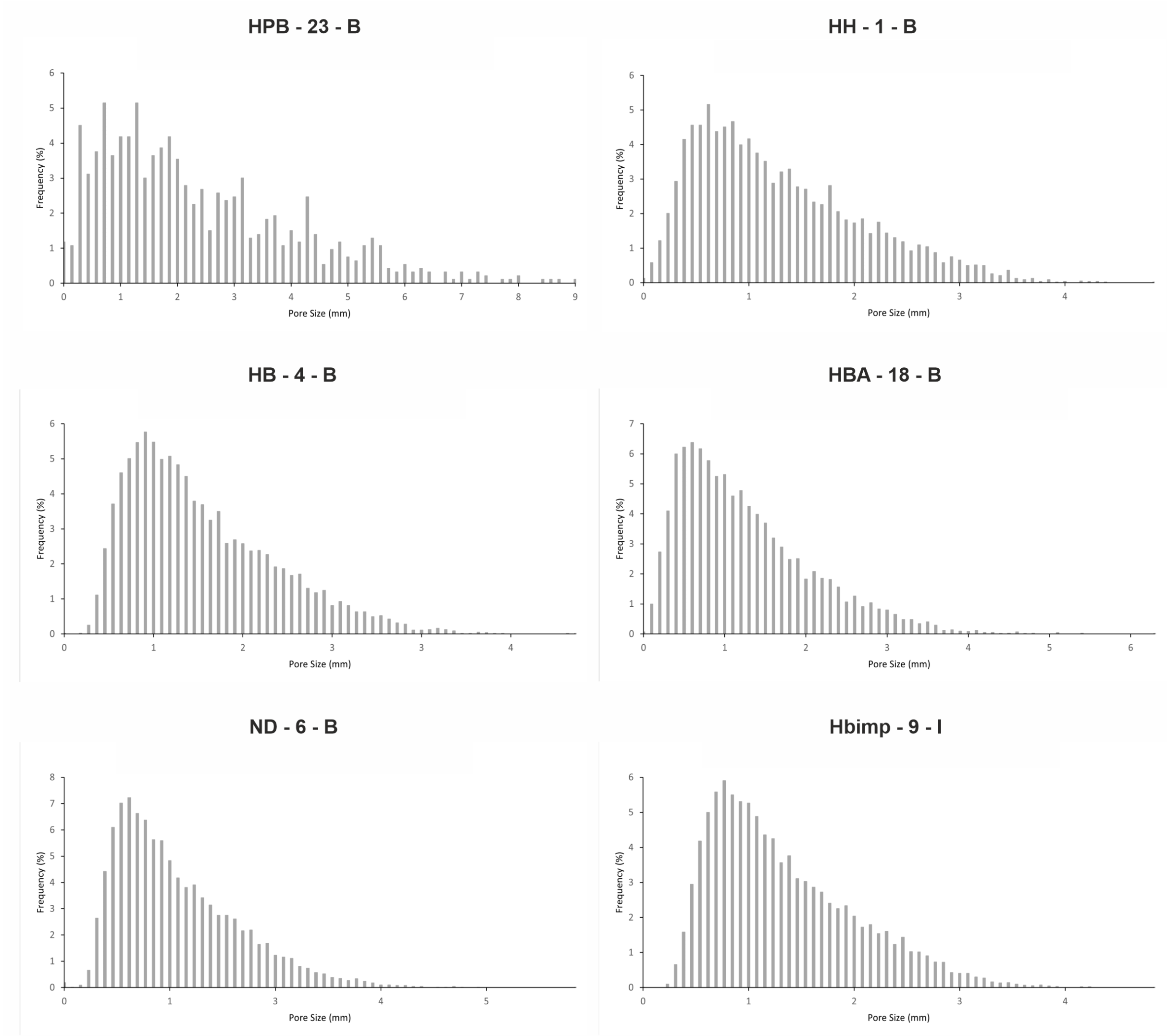

Figure 4.7: Pore-size distribution of unconnected porosity.

Combining all of this information, it can be said that the basalt with the largest pore size, for both connected and unconnected porosity, is HPB-23-B, followed by HB-4-B and HBA-18-B, and lastly with only unconnected porosity, HBimp-9-I. However, in general, the pore size distribution in basalt samples is fairly similar for all analyzed samples except for HPB-23-B, which has much larger pores. The ND-6-B dike has a pore size mode value of 0.78 mm, which is similar to most basalts. On the other hand, the HH-1-B hyaloclastite has a mode value of 0.47 mm for connected porosity and 0.81 mm for unconnected porosity.

Additionally, measurements of pore-wall surface area were conducted and found to have a direct relationship with pore size. Notably, the samples with the smallest pore size, such as HBimp-9-I, HBA-18-B and HH-1-B, exhibited a higher surface area-to-volume ratio, indicating a higher amount of pore surface per unit volume.

4.2. Geomechanical Properties

4.2.1. Unconfined Compression Test

Table 4.3 presents a summary of the results obtained from the Unconfined Compression Test, including Maximum Stress the samples can withstand, Young's Modulus, Poisson's ratio, the average S and P wave velocities and the Vp/Vs ratio for each sample.

	Φ [%]	Max Stress [MPa]	Young Modulus	Poisson's Ratio	Vp [m/s]	Vs [m/s]	Vp/Vs ratio
HBA – 18 – A	51.37	12.58	7.61	0.23	2006	2872	1.43
HBA – 18 – B	42.20	13.95	7.66	0.40	1935	2942	1.52
HBA – 18 – C	50.36	11.76	5.84	0.22	2956	1830	1.62
HBA – 18 – D	45.05	26.71	6.69	0.11	4312	2742	1.60
HH – 1 – B	47.03	2.37	2.23	0.05	-	-	-
HH – 1 – C	44.90	3.23	0.56	0.03	-	-	-
HH – 1 – D	40.98	1.49	0.34	0.02	-	-	-
HH – 1 – E	45.91	2.42	0.62	0.01	-	-	-
HPB – 23 – A	36.54	29.51	7.31	0.16	3017	1806	1.67
HPB – 23 – B	36.89	21.92	6.81	0.12	3166	1833	1.73
HPB – 23 – C	41.75	20.32	6.03	0.18	3057	1795	1.70
HPB – 23 – D	46.87	9.64	3.10	0.17	2817	1727	1.63
HB – 4 – A	24.87	74.82	15.31	0.15	3899	2423	1.60
HB – 4 – B	25.71	81.72	18.32	0.22	3710	2306	1.61
HB – 4 – C	23.34	101.67	18.84	0.21	3923	2462	1.59
HB – 4 – D	26.66	75.56	18.96	0.23	3962	2563	1.55
HBimp – 9 – A	20.31	65.22	16.80	0.33	3762	2332	1.61
HBimp – 9 – B	22.10	59.70	13.36	0.25	3514	2154	1.63
HBimp – 9 – C	20.97	58.45	14.99	0.26	3405	2105	1.62
HBimp – 9 – D	18.19	95.20	20.89	0.24	3733	2316	1.61
ND – 6 – A	8.44	193.26	28.54	0.16	4646	3065	1.52
ND – 6 – B	9.45	130.14	27.23	0.33	4541	3208	1.42
ND – 6 – C	7.90	161.21	32.30	0.27	4621	3335	1.39
ND – 6 – D	8.64	121.24	24.82	0.15	4664	3253	1.43
G – A	0.18	108.27	47.35	0.18	5897	4042	1.46
G – B	0.27	71.58	29.98	0.19	5501	3422	1.60
G – C	0.92	119.60	49.89	0.10	5855	4058	1.44
G – D	0.4	74.36	40.68	0.24	5714	3875	1.47

Table 4.3: Summary Table of Unconfined Compression Test Results.

In addition to the data collected in the previous table, the results per sample and rock have been plotted in Figures 4.8 and 4.9, which show the 'stress vs strain' and 'axial strain vs radial strain' plots respectively. This facilitates the analysis and comparison between the different samples.

Rock G, the gabbro, exhibits a range of maximum stress values between 71.58 MPa and 119.60 MPa. No permanent deformation before breaking is observed for samples G-A and G-C. However, some

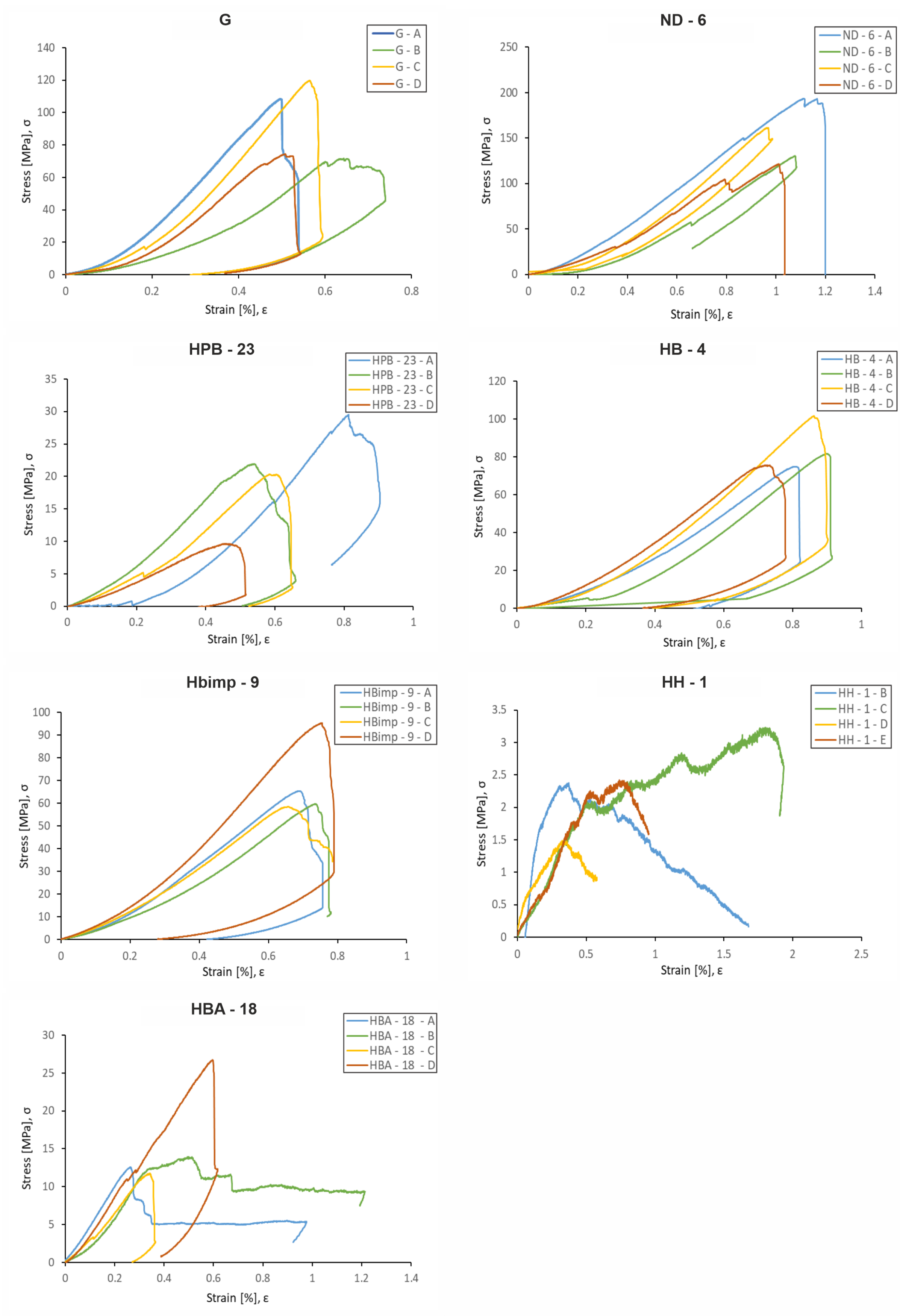

Figure 4.8: Stress vs Strain Plots per sample, per rock.

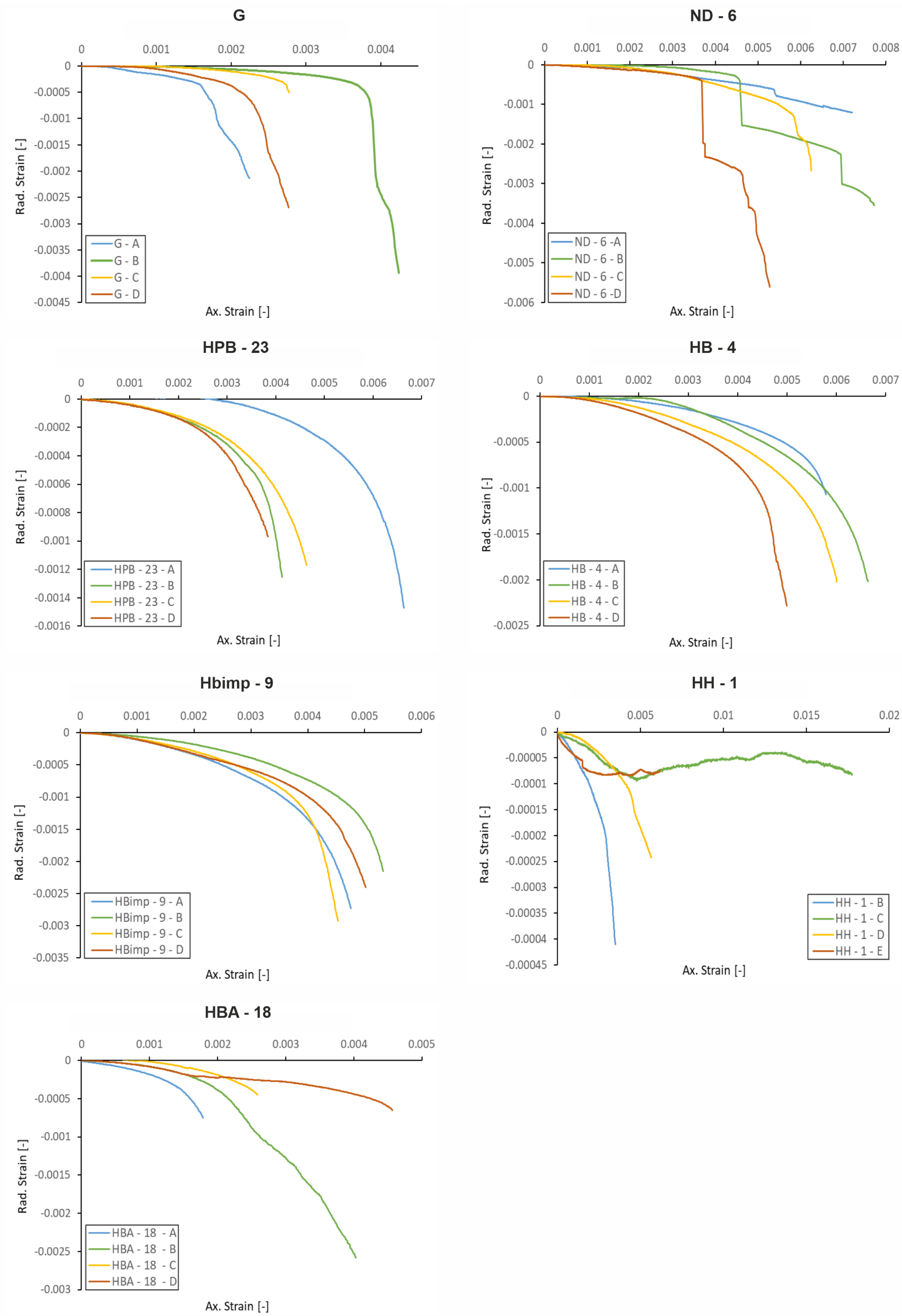

Figure 4.9: Radial Strain vs Axial Strain Plots per sample, per rock.

breaking have occurred before macroscopic failure for G-B and G-D. The porosity of the samples does not show any relationship with their maximum stress; however, a positive relationship is observed between the maximum stress and the Young's modulus. The value of Young modulus for this rock oscillates between 29.98 GPa to 49.89 GPa. The radial strain vs. axial strain plots for all G samples show a similar deformation process, with some samples exhibiting greater radial deformation than others. The samples' deformation order in decreasing magnitude is as follows: samples A, D, C, and B. On the other hand, no relationship has been observed between Poisson's ratio, which is between 0.10 and 0.23, and the maximum stress.

In the case of the dike (ND-6), it exhibits the highest maximum stress of all tested samples, between 121.24 MPa and 193.26 MPa; however, its Young's modulus is lower than that of the G rock samples, ranging between 24.82 GPa and 32.3 GPa. All stress-vs-strain plots show that the samples reach a yield point before breaking. Interestingly, the sample that reaches the maximum stress does not have the highest Young's modulus value. No observed relationship is found between the porosity and the maximum stress, nor between Poisson's ratio, which has values between 0.15 and 0.26, and other parameters. The curves of radial strain vs. axial strain show some differences among the samples. Samples B and C resemble each other, while A and D exhibit different behavior. The trajectory of the curves of B and C reveals a small elastic radial expansion until the sample suddenly breaks. These samples are the ones that reach the lowest maximum stress values for ND-6.

The basalt material known as HPB-23 shows a direct relationship between its maximum stress and Young's modulus. Specifically, the values of maximum stress and Young's modulus for HPB-23 fall within the ranges of 9.64 to 29.51 MPa and 3.1 to 7.31 GPa, respectively. Interestingly, the sample with the lowest porosity reaches the highest maximum stress, and this is the only sample in which this relationship is observable, despite the fact that maximum stress varies greatly for each sample, whose porosities vary up to 10%. No relationship is observed between Poisson's ratio and other parameters. The values of this parameter range between 0.12 and 0.18. The radial strain vs. axial strain graphs have a very similar shape, and sample A is notably shifted to the right compared to the others. This is due to the fact that at the beginning of the experiment, this rock experiences some permanent deformation. This may be due to the fact that the top and bottom of the sample were not completely parallel.

In the case of basalt HB-4, this material can withstand axial stress ranging between 74.82 MPa and 101.67 MPa. This material has a Poisson's ratio that falls within the range of 15.31 GPa to 18.96 GPa, and a Young's modulus that ranges between 0.14 and 0.22. Sample C corresponds to the sample with the highest porosity and is the one that withstands the highest maximum stress. Samples B, C, and D have similar values of Young's modulus and Poisson's ratio for different values of maximum stress. Sample A has a similar curve and a similar maximum stress to D and B, but it has lower Young's modulus and Poisson's ratio. No relationship is found between porosity, maximum stress, or other parameters. All four samples break suddenly without accumulating permanent deformation previously. Radial strain vs. axial strain plots are similar to each other, and the Poisson's ratio values are very similar for B, C, and D and slightly lower for A.

Regarding basalt HBimp-9, it can withstand stresses ranging from 58.5 MPa to 95.20 MPa. Its Young's modulus has values ranging from 13.36 GPa to 20.89 GPa, and its Poisson's ratio ranges between 0.24 and 0.33. For this rock, all stress vs. strain plots exhibit a similar behavior, and sample D, which has the lowest porosity, supports the highest maximum stress. This sample also has the maximum value of Young's modulus for this rock and the minimum value of Poisson's ratio. However, this relationship between properties could not be found for the rest of the samples. Samples A, B, and C exhibit similar values of porosity, maximum stress, and Young's modulus. When the rock breaks, it does so suddenly, without accommodating deformation in small fractures as observed in the graphs. Regarding radial strain vs. axial strain plots, all curves exhibit a similar behavior.

Moving on to the hyaloclastite HH-1, the stress vs. strain plots exhibit a zigzag pattern, which can lead to errors in calculating Young's modulus and Poisson's ratio, as there is no linear regime and the deformation experienced by the sample from the beginning of the test is permanent. This rock can withstand maximum stresses ranging from 1.49 MPa to 3.23 MPa. Its Poisson's ratio ranges between 0.34 GPa and 2.23 GPa. Additionally, its values of Poisson's ratio fall between the range of 0.01 and 0.05. Sample C has the highest value of maximum stress, while samples B and E have similar maximum stresses, and sample D has the lowest. However, no relationship has been found between porosity and maximum stress in this sample, nor with other parameters such as Poisson's ratio or Young's modulus. The radial strain vs. axial strain graphs for the different samples are very different from each other, with the Poisson's ratio values being the lowest of the entire investigation. Samples B and D exhibit greater radial deformation than E and C.

Finally, the basalt HBA-18 shows no significant correlation between the maximum stress, porosity, or other parameters. The maximum stress that it can withstand ranges from 11.76 MPa to 26.71 MPa. Its Poisson's ratio falls between the range of 5.84 GPa and 7.66 GPa, while its Young's modulus falls within the range of 0.11 to 0.40. Sample D withstands a much higher maximum stress than the other three samples. The deformation behavior of the samples after rupture is very different, although they show similar linear regimes. Samples such as D and C, after reaching their maximum stress, cannot accommodate any more deformation. In contrast, samples A and B continue to deform and accommodate a lot of deformation until they break definitively again. Regarding the radial strain vs. axial strain plots, the samples show a similar behavior to each other.

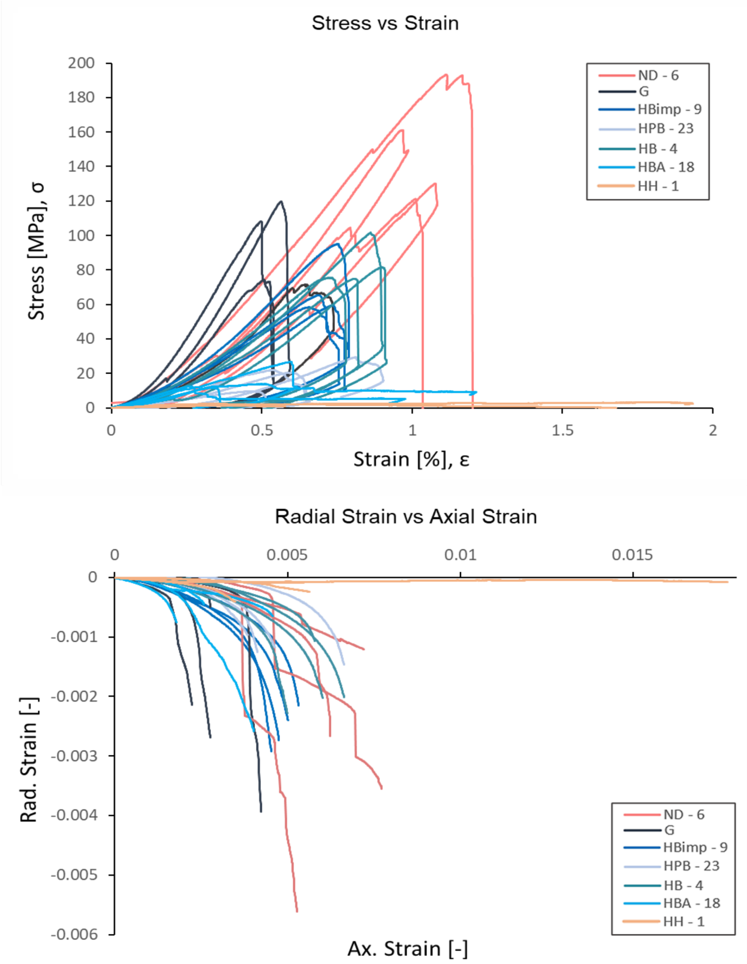

Figure 4.10: Comparison of 'Stress vs Strain' & 'Radial Strain vs Axial Strain' Plots of all samples.

After comparing the different samples within each rock, the samples were compared with each other across all rocks. To accomplish this, two plots were generated, one showing stress vs strain and the other showing axial strain vs radial strain, displaying all the results together (refer to Figure 4.10). In these graphs, five units can be identified: Gabbro unit, ND-6 unit, HBimp-9 and HB-4 unit, HPB-23 and HBA-28 unit, and HH-1 unit.

The gabbro (G) is the stiffest of the materials and deforms less axially. However, it does not reach the high maximum stresses of ND-6. ND-6 has the lowest Young's modulus of the group, meaning it deforms slightly more, although less than the basalts. HBimp-9 and HB-4 have similar petrophysical and mechanical properties, although HB-4 is slightly more porous. The basalts with the lowest Young's modulus are HBA-18 and HPB-23, with the latter being more porous and reaching lower maximum stress values but similar Young's modulus values to HBA-18. However, HBA-18 reaches higher Poisson's ratio values and deforms more radially. HH-1 is the rock that reaches the lowest maximum stress and has the lowest Poisson's ratio, indicating that it deforms very easily radially compared to other lithologies. Additionally, this rock also has a very low Young's modulus, indicating that it undergoes significant axial deformation.

4.2.2. Active-Source Acoustics Test

During the Unconfined Compression Test, the P-wave and S-wave velocities were measured using an active-source acoustic test. The results plotted by sample are displayed in Figure 4.11.

The acoustic velocities of the different rock samples in this study have been determined through the analysis of P- and S-waves. The rock sample with the highest average P-wave velocity is the gabbro (G), with velocities ranging from 5501 to 5897 m/s, followed by the basalt HB-4, with velocities ranging from 3710 to 3962 m/s. The dike (ND-6) has a narrower range of P-wave velocities, with values ranging from 4541 to 4664 m/s. The basalt HBimp-9 has a lower P-wave velocity range, between 3405 and 3762 m/s, while the basalt HPB-23 has a still lower range, with velocities ranging from 2817 to 3166 m/s. The basalt HBA-18 has the lowest P-wave velocity range, but it is also the most variable, with velocities ranging from 1935 to 4312 m/s. As for the S-wave velocities, the gabbro once again has the highest range, with values ranging from 3422 to 4058 m/s, followed by the basalt HBA-18, with a range of 1830 to 2942 m/s. The other rocks have lower ranges of S-wave velocities, with the dike (ND-6) ranging from 3065 to 3335 m/s, the basalt HB-4 ranging from 2306 to 2563 m/s, the basalt HBimp-9 ranging from 2105.19 to 2332.27 m/s, and the basalt HPB-23 ranging from 1727 to 1833 m/s. Finally, no acoustic data could be acquired for the hyaloclastite HH-1.

Upon analyzing the data acquired from the active-source acoustics test, it is evident that there is a certain degree of variability among the different samples of each lithology. Notably, the greatest variability is observed among the samples of rock HBA-18, with sample HBA-18-D standing out as an outlier. The results obtained from this sample are significantly different from the other three samples, as clearly depicted in Figure 4.11. In contrast, the results for the other rock types appear consistent, with a variability ranging between 100 and 300 m/s for different samples.

For all samples, the graphs show that the velocity of waves increases as the applied stress increases, especially the velocity of P waves. This increase is particularly notable for rocks HBimp-9 and HB-4, slightly less for HPB-23, HBA-18, and ND-6, and almost imperceptible for G. Once again, if we take the mean velocities to observe the overall trend, the four first units differentiated by their mechanical properties can be distinguished: Gabbro unit, ND-6 unit, HBimp-9 and HB-4 unit, HPB-23 and HBA-28 unit.

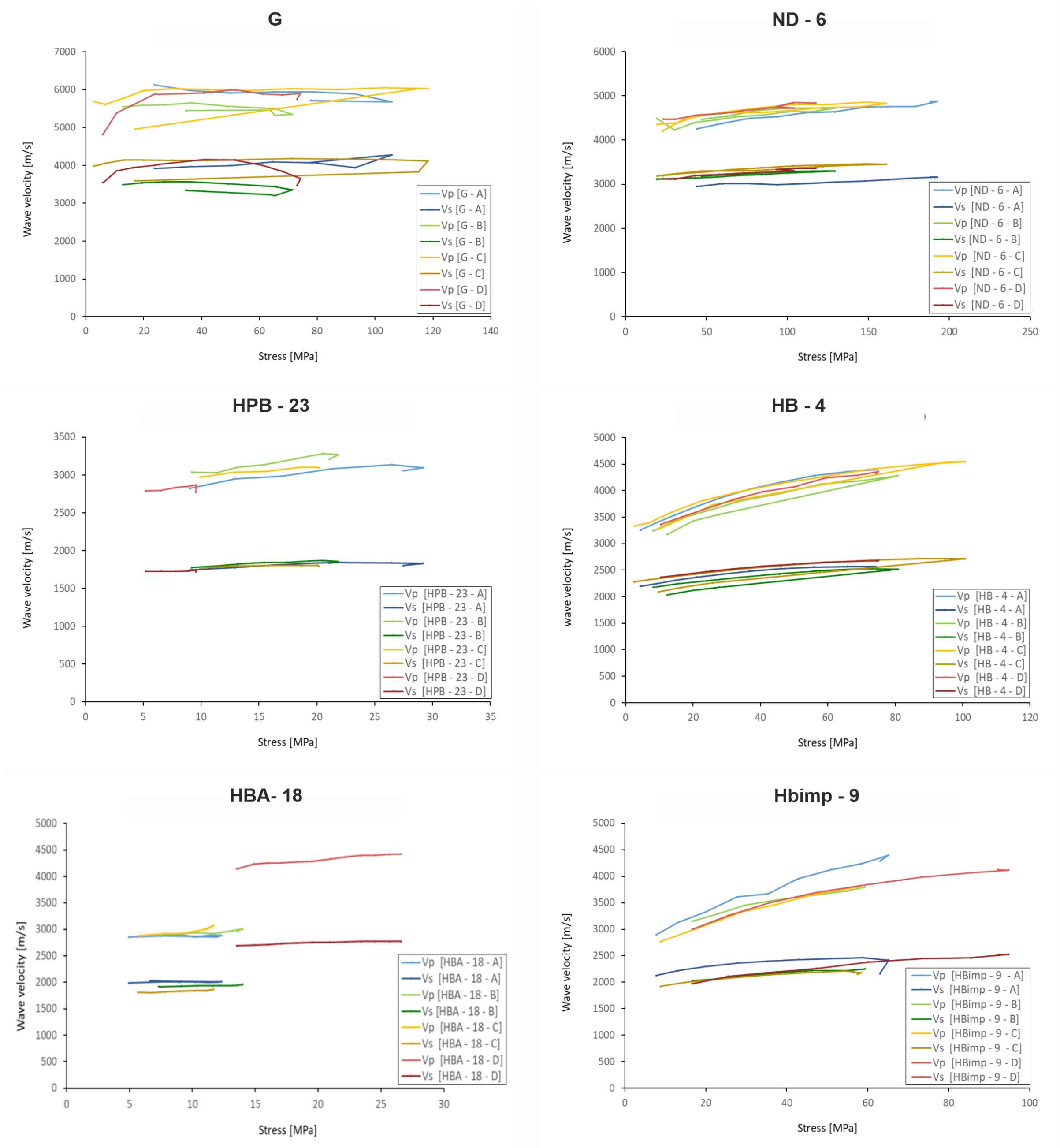

Figure 4.11: Active-Acoustic Test results for different rock samples under axial stress conditions. The graphs display the P- and S-wave velocities for six different rock types, including gabbro, dike (ND-6), basalt HBimp-9, basalt HB-4, basalt HPB-23, and basalt HBA-18, measured at different levels of axial stress in MPa. Each line in the plot corresponds to a different sample of the respective rock type.

4.2.3. Splitting Tensile Strength Test (Brazilian)

The Splitting Tensile Strength Test has been performed on all rocks except for G due to lack of material. The results per sample are presented in Figure 4.12 and the average values per rock in Table 4.4.

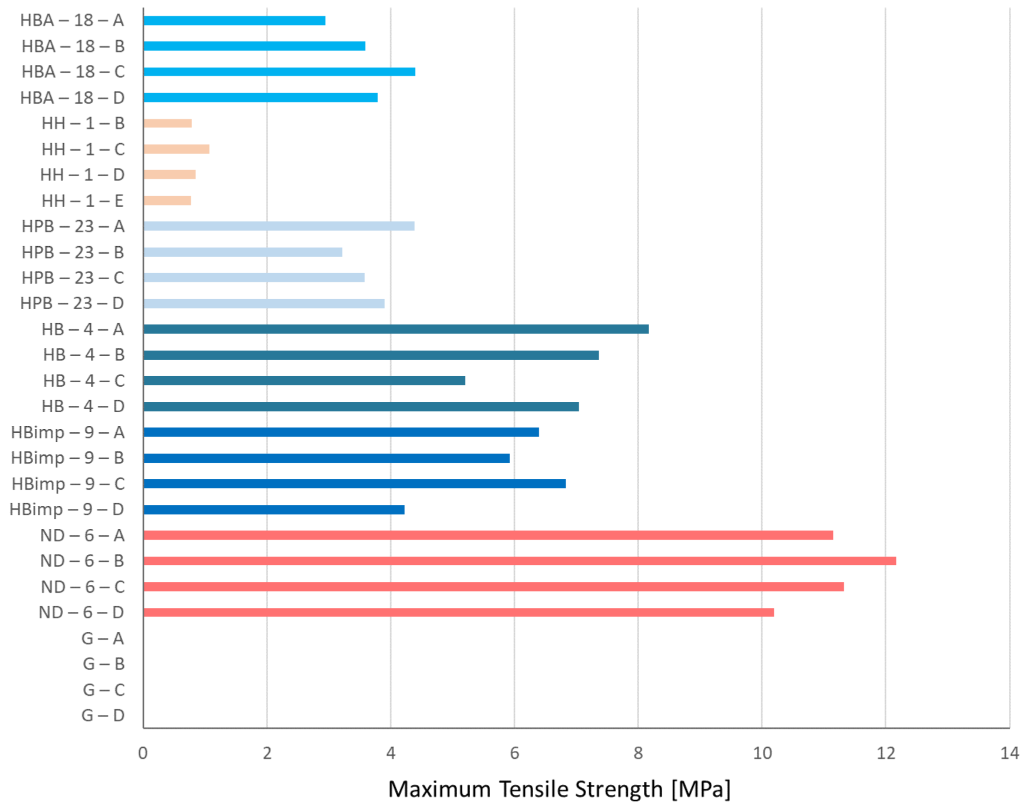

Figure 4.12: Maximum Tensile Strength values per sample, per rock.

	HBA - 18	HH - 1	HPB - 23	HB - 4	HBimp - 9	ND - 6	G
Max. Tensile Strength [MPa]	3.68	0.87	3.77	6.94	5.84	11.21	-

Table 4.4: Average Maximum Tensile Strength values per rock.

The maximum tensile strength values for different types of rocks have been determined through laboratory experiments. The dike (ND-6) has the highest tensile strength values, ranging from 10.2 to 12.17 MPa. The basalt HB-4 follows with a maximum tensile strength range of 5.2 to 8.17 MPa, while the basalt HBimp-9 has a range of 4.23 to 6.83 MPa. The basalt HPB-23 has a maximum tensile strength range of 3.22 to 4.39 MPa, and the basalt HBA-18 has a range of 2.95 to 4.4 MPa. The hyaloclastite HH-1 has the lowest maximum tensile strength range among the rocks, varying between 0.78 and 3.79 MPa.

4.3. Thermal Shock Experiment Results

4.3.1. Observed changes in porosity

In order to carry out this experiment, samples A, B, C, and D from the HBimp-9 rock have been established as the control group. The samples subjected to thermal shock (E, F, G, and I) have been compared with the control group with respect to their mechanical properties and to themselves before the test to evaluate changes in porosity.

The porosity values were measured with a helium pycnometer before and after the experiment. The results by sample are depicted in Figure 4.13. The average porosity of the control group is around 20.39%, while that of the TS group before the test is 20.91%. The average porosity after the test is 21.41%. The results of the UCS test are presented in Figure 4.14, allowing for comparison with the control group. After the thermal shock, there is an increase in porosity of 0.5% on average with respect to the values measured before the test.

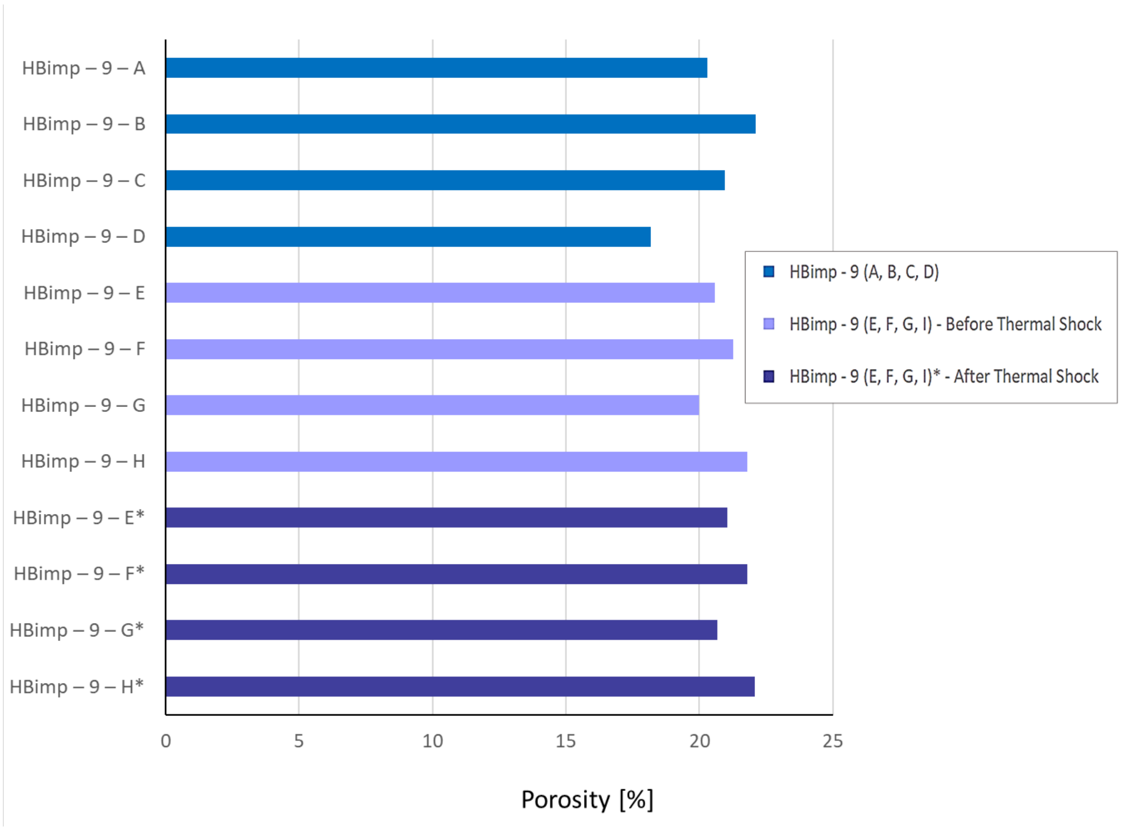

Figure 4.13: Porosity values for HBimp-9 samples. Control group (A, B, C, D) and thermal shock group (E, F, G, I) before and after the test.

4.3.2. Changes in Mechanical Properties after Thermal Shock

With respect to the mechanical properties, the mean maximum stress value for the control group is 69.64 MPa, and 64.76 MPa for the TS after the test. The Young's modulus reaches an average value of 16.51 GPa in the control group, while for the TS after the test, the value of this parameter is on average 16.02 GPa. Similarly, the Poisson's ratio of the control group is 0.27 on average, while for the TS after the test it is 0.3.

The mean maximum stress value has decreased by around 4.88 MPa, and the Young's modulus has decreased by 0.49 GPa. The value of Poisson's ratio has increased by 0.03.

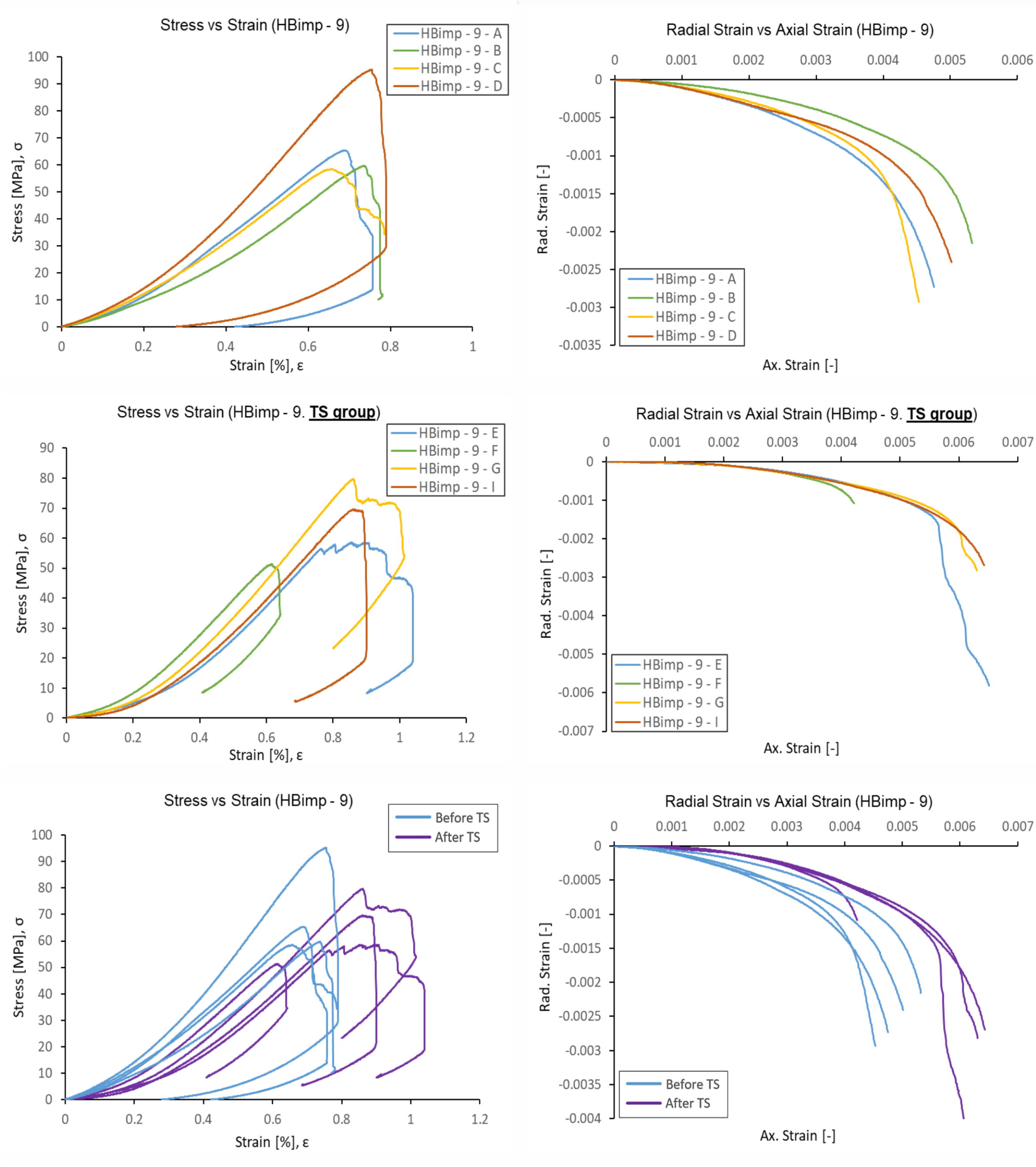

Figure 4.14: Stress vs Strain & Radial Strain vs Axial Strain Plots of Control group and Thermal Shock group after the test.

4.3.3. Changes in Wave velocities after Thermal Shock

In Figure 4.15, the results of the active-source test carried out during the UCS test are shown. The average velocity of P and S waves measured through the TS samples during the test is 3977 m/s and 2300 m/s, respectively. For the control group, these values are 3603 m/s and 2227 m/s. This means that after performing the thermal shock, there was a relative increase of 10% in the P-wave velocity (from 3603 m/s to 3977 m/s), and a relative increase of 3% in the S-wave velocity (from 2227 m/s to 2300 m/s).

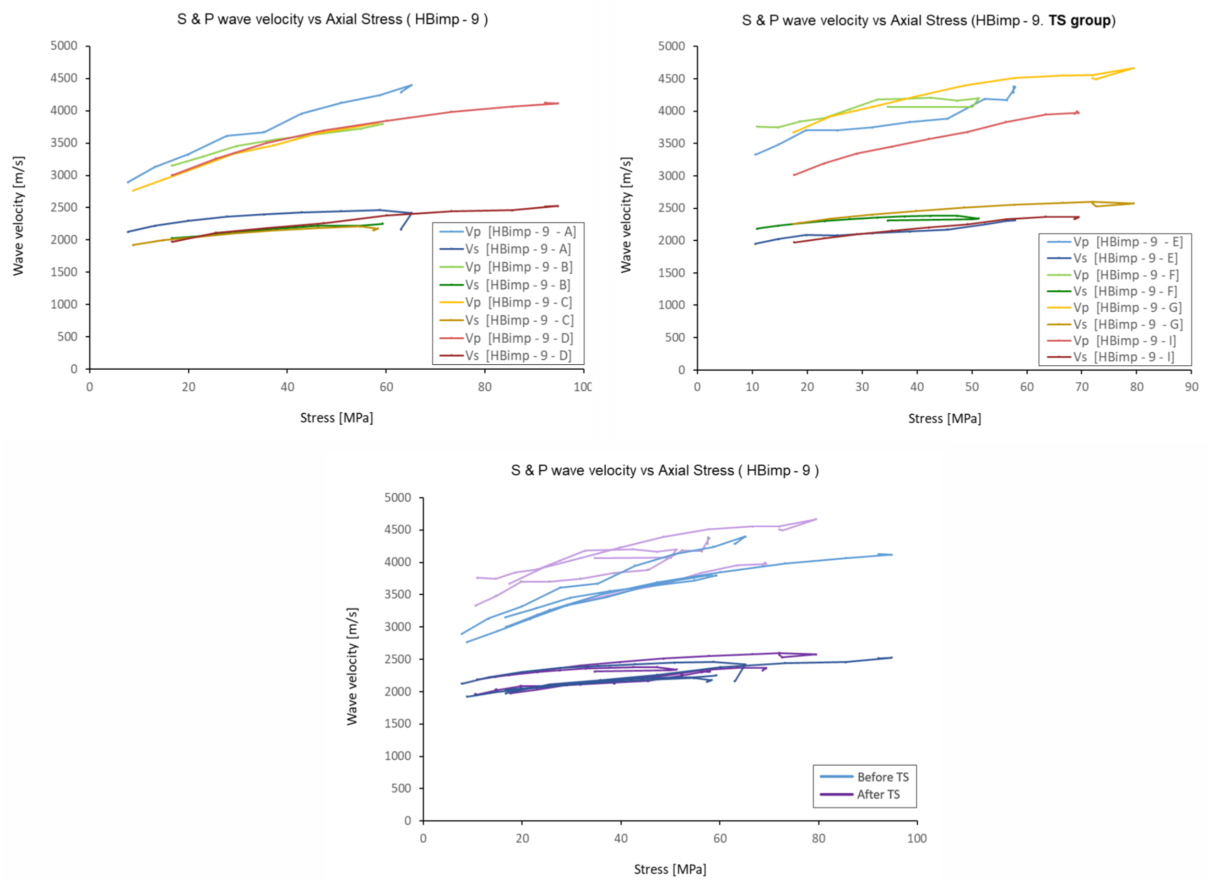

Figure 4.15: Active-Source Acoustics Test results for P & S wave velocity of Control group and Thermal Shock group after the test.

	Φ [%]	Increase in porosity [%]	Max Stress [MPa]	Young's Modulus	Poisson's Ratio	Vp [m/s]	Vs [m/s]	Vp/Vs ratio
HBimp – 9 – A	20.31	-	65.22	16.797	0.3320	3762.02	2332.27	1.61
HBimp – 9 – B	22.10	-	59.70	13.364	0.2491	3514.71	2154.88	1.63
HBimp – 9 – C	20.97	-	58.45	14.985	0.2641	3405.02	2105.19	1.62
HBimp – 9 – D	18.19	-	95.20	20.8885	0.2353	3733.00	2316.83	1.61
HBimp – 9 – E	20.57	0.48	58.57	16.050	0.3548	3923.43	2172.49	1.8
HBimp – 9 – F	21.28	0.53	51.36	16.835	0.2473	4028.54	2316.27	1.74
HBimp – 9 – G	19.99	0.69	79.64	15.599	0.2648	4324.79	2488.08	1.73
HBimp – 9 – I	21.80	0.29	69.47	15.614	0.3274	3632.51	2223.66	1.63

Table 4.5: Summary Table of Unconfined Compression and Active-Source Acoustics Results for both Control group and Thermal Shock group.

5 Discussion

The official model of the Husmuli reinjection site, as presented in Chapter 2.2 of this work, indicates that the subsurface of the area of interest is composed of the crystalline base of the Hengill volcano, upon which sits a succession of hyaloclastite and lava flows. This succession is intersected by sub-vertical intrusions. Since no drilling samples were available, the rocks studied were sampled from surface outcrops in a way that would provide a representative set of samples based on the lithologies and rock textures present in the area.

The findings of this study provide significant insights into the petrophysical and mechanical properties of rocks collected from the surface of the Hellisheiði geothermal field, validating their potential use as reservoir analogs, and exploring the feasibility of using thermal fracturing as a mechanism to enhance their effective porosity and CO_2 storage capacity. In this discussion section, the findings of the study are analyzed and their implications are discussed in relation to the research question. Furthermore, the limitations of the study are acknowledged, and recommendations for future research are proposed.

5.1. Petrophysical properties

After obtaining effective porosity values using a helium pycnometer and calculating bulk density values for each sample, a consistent trend was observed: samples with lower porosity values tended to have higher bulk density values. This relationship is depicted in Figure 5.1 and suggests that rocks with higher porosity tend to be less dense overall. However, it was also noticed that some samples, such as G and HH-1, did not conform perfectly to this linear trend.

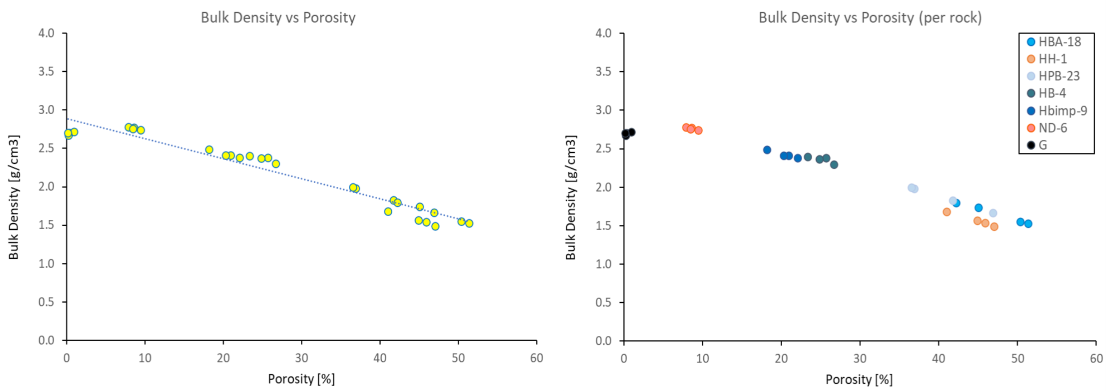

Figure 5.1: Comparing the relationship between Density and Porosity. The left plot shows all samples together with a trendline, while the right plot distinguishes between different rock types for a more detailed analysis.

These deviations from the general pattern could be due to could potentially be attributed to variations in the matrix density of the samples, which are dependent on their mineralogical and compositional differences. The precise effects of such variations should be carefully considered, particularly in volcanic systems where temperature changes may cause mineral alteration at different depths, leading to changes in composition.

The obtained permeability data did not provide enough information to plot any significant relationships between permeability and density or porosity. As explained in Chapter 4, the permeability of the gabbro (G) could not be measured due to the insufficient material available in the block. Additionally, some rocks had permeability values that exceeded the measurement limit of the instrument used, such as hyaloclastite HH-1 and basalt HPB-23, while others had permeability values that were below the limit, such as certain samples of dike ND-6. Despite these limitations, the data suggests that rocks with high porosity tend to exhibit higher permeability values. However, it is important to note that other factors, such as pore size, may also play a significant role in determining permeability. For instance, the basalt HPB-23 had lower porosity than basalt HBA-18, but exhibited higher permeability, likely due to differences in their pore-size distribution.

The porosity of the samples has been extensively studied using different methods. Differences have been observed between porosity measured with the helium pycnometer and porosity measured using image analysis software. The porosity measured by the helium pycnometer includes the surface porosity of the sample as part of the connected porosity, which may not be the case *in situ*. Moreover, it can measure connected porosity below 60 µm, but cannot provide information on unconnected porosity. Conversely, the image analysis software can differentiate between connected and unconnected porosity as long as the scale is greater than 60 µm. Thus, the microCT scans provide a conservative estimate of total porosity and an overestimated value of unconnected porosity.

Porosity is a critical factor that directly affects the ability of geological formations to store CO_2 as minerals. This is not only because it directly affects the storage capacity of rocks, but also because the surface area of the pore walls is where CO_2 dissolved in water reacts and precipitates as carbonates. Therefore, the efficiency of the reactive process can be increased by increasing the available reactive surfaces in contact with the fluid since more minerals are available to release cations that will subsequently react with CO_2 to form carbonates. In samples where connected and unconnected porosity could be measured, it was observed that there is potentially more available surface in the unconnected porosity of HBA-18 and HB-4 than in that of HPB-23. This can be explained by the pore size distribution of each sample and the relationship between the volume and surface area of a sphere. Assuming that the pores have a pseudo-spherical morphology, as the sphere grows in size, both its surface area and volume increase, but not in the same proportion. The surface area will increase by a factor of 4, while its volume will be multiplied by a factor of 8. Therefore, a pore size distribution with an abundance of small pores over large ones will have more available surface area.

A comprehensive study was conducted to measure the porosity of the samples, but for the purpose of this chapter, the porosity measured using the helium pycnometer will be used to compare with other parameters and identify trends. Based on the results of the porosity, bulk density, and permeability analysis, as well as observations of the rock blocks, the samples can be classified into three distinct units or units according to their petrophysical properties:

- Unit 1 is comprised solely of the Hyaloclastite HH-1, an unconsolidated sedimentary rock composed of volcanic-glass clasts. Due to its unique nature, this rock type requires a separate classification, as it cannot be directly compared to the other rocks in this study. Unit 1 has the lowest density, with a mean value of 1.51 g/cm^3, one of the highest permeabilities, above 33 mD, and the second-highest porosity, 44.68%, only surpassed by basalt HBA-18.

- Within unit 2, the HBA-18 and HPB-23 basalts exhibit notable similarities in terms of their nature, as well as their porosity (ranging from 40.34% to 46.38%), density (between 1.68 and 1.87 g/cm^3), and permeability values. In fact, they have the highest observed permeability values for basalts in this study. As such, they can be meaningfully grouped together based on these shared characteristics.

- Unit 3 groups together the HBA-4 and HBimp-9 basalts, which share similar characteristics. Like the basalts in unit 2, these samples have comparable average porosity values, ranging from

21.53% to 24.99%, as well as similar density values, ranging from 2.36 to 2.38 g/cm^3. While their average permeability values are considerably different, ranging from 6.23 to 0.14 mD, these two basalts are more closely related to each other than to the rest of the samples, making them a distinct subgroup within the larger dataset.

- Unit 4 is represented by the ND-6 dike, which is classified as its own distinct unit not only due to its nature but also its distinctive properties. Its porosity, at 8.71%, is the second lowest observed in this study and stands in stark contrast to the porosities of units 1, 2, and 3. Its density, averaging at 2.76 g/cm^3, is similarly distinct from the other rocks. The dike's permeability is dominated by fractures, which hindered measurement in all samples and allowed measurement only in the samples whose fractures aligned with the primary flow direction of the measurement instrument. Therefore, its permeability can be estimated to be between <0.03 and 7.76 mD.

- Unit 5 is represented by the Gabbro G, which is a plutonic igneous rock. However, unlike the dike, their textures are completely different, making it impossible to include them in the same unit. The gabbro has a coarse-grained phaneritic texture, with minerals large enough to be identifiable without magnification. On the other hand, the dike is a narrow, sheet-like body of igneous rock with a fine-grained texture. Although the gabbro has a density value similar to that of the dike at 2.7 g/cm^3, its porosity value is extremely low, averaging around 0.44%. Additionally, the Gabbro G has been considered an analog rock for the crystalline basement of the Hengill system. However, it has not been sampled in the area of interest.

5.2. Geomechanical properties and Wave velocities

Extensive studies have been conducted on the relationship between mechanical properties and petrophysical characteristics, and while comparing different samples from the same rocks, clear relationships may not be immediately apparent. However, these relationships can be observed and better understood by taking into account the average values of the samples. This could be attributed to the variability of the samples themselves, which are taken from heterogeneous rock blocks and aim to capture such heterogeneity. The graphs in Figures 5.2 and 5.3 show an inverse relationship between porosity and the ultimate compressive strength, as well as a direct relationship between Young's modulus and the maximum strength of the samples. Although, theoretically, materials with higher Poisson's ratios are typically more brittle and less capable of withstanding deformation, and those with lower ratios are more ductile and can sustain more deformation before failure, no relationship could be established between these parameters and Poisson's ratio, as evident in Figure 5.4. It is important to note that these relationships between different mechanical parameters are found only when comparing rocks with primary porosity. The rocks G and HH-1 show a slight deviation from this trend, probably because they are a material with porosity dominated by fractures and an unconsolidated material.

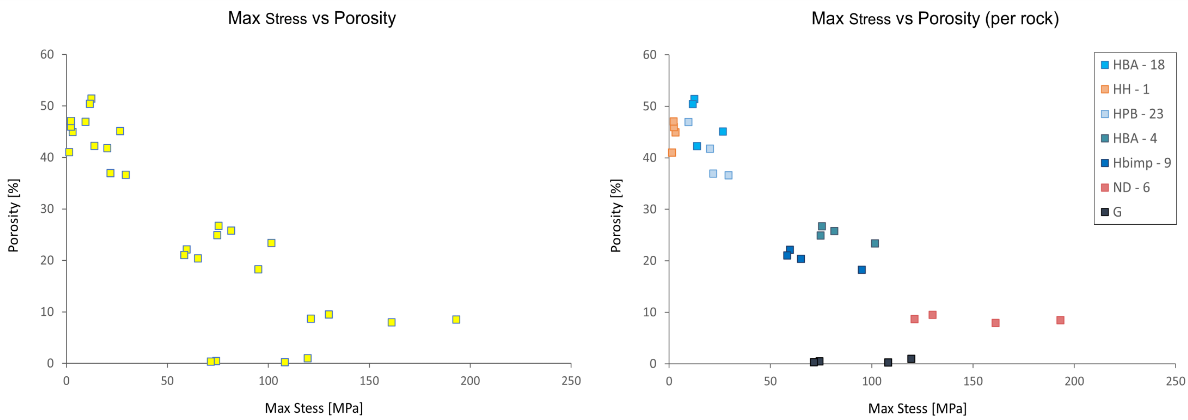

Figure 5.2: Relationship between maximum stress and porosity.

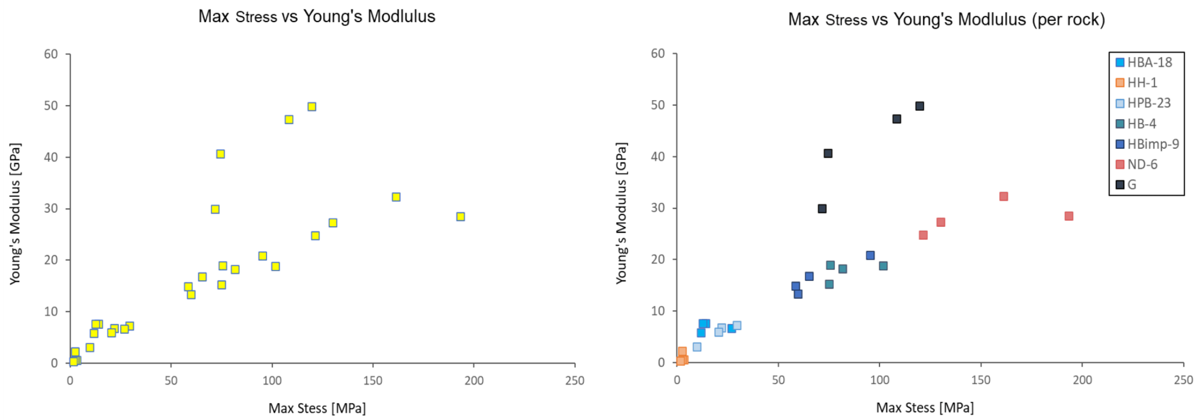

Figure 5.3: Relationship between maximum stress and Young's modulus.

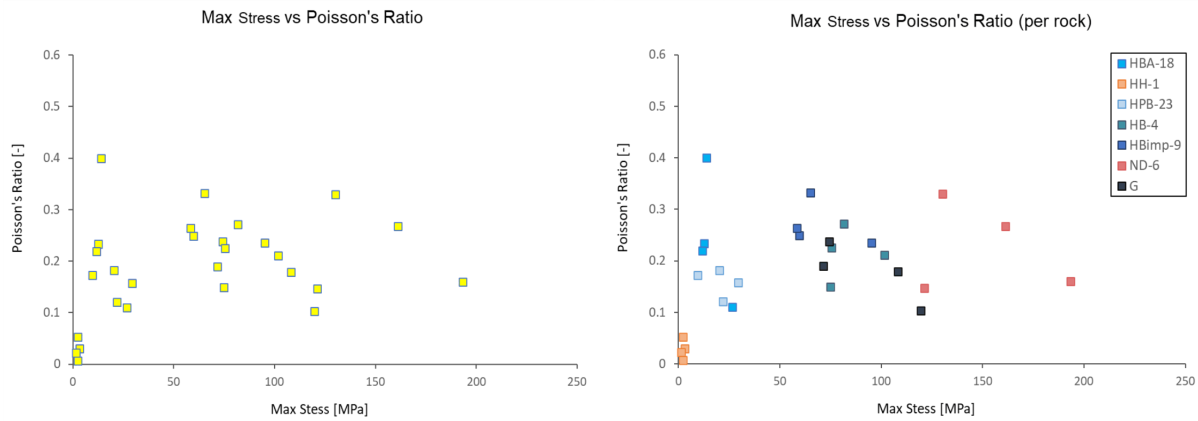

Figure 5.4: Relationship between maximum stress and Poisson's ratio.

It can be said that a clear relationship has been found between three parameters: porosity, ultimate strength, and Young's modulus. After analyzing the geomechanical properties of the rocks, the same units established based on petrophysical parameters in the previous section were identified: Unit 1, hyaloclastite HH-1; Unit 2, basalts HBA-18 and HPB-23; Unit 3, basalts HB-4 and HBimp-9-; Unit 4, dike ND-6; Unit 5, gabbro G.

After obtaining the mechanical properties of the different rocks, it is worth questioning whether these surface-collected samples would maintain the same properties if they had been buried to the depths at which the main feed zones are located. To answer this, and given that the experiments were conducted without considering the confining pressure, only the vertical stress (S_v) in the area of interest will be taken into account. The S_v model for Húsmuli was developed by Batir et al. (2012) based on the integrated weight of overburden, on the lithologic model from the mud log of the well HN-16 and the bulk densities in Gudfinnsson et al. (2010).

The results of this analysis should be approached with caution since the maximum stress that rocks can withstand increases with confining pressure, meaning that the conclusions derived from this analysis will be conservative. In Figure 5.5, the main feedzones found in the drilled wells in Húsmuli are represented by horizontal dashed lines at their subsurface depth. These feedzones are mainly located from approximately 900 m below the surface to a depth of 2180 m. Vertical lines of different colors indicate the average maximum stress that the different rocks studied in this work can sustain. The ultimate strength of HBimp-9 and HB-4 basalts, gabbro G, and dike ND-6 are above the S_v at those depths. However, this is not the case for Basalt HBA-18 and hyaloclastite HH-1, which have a lower ultimate strength than S_v for the subsurface region where the feedzones are located. Basalt HPB-23 is in an intermediate situation, with its ultimate strength being higher than S_v up to a depth of 1700 m.

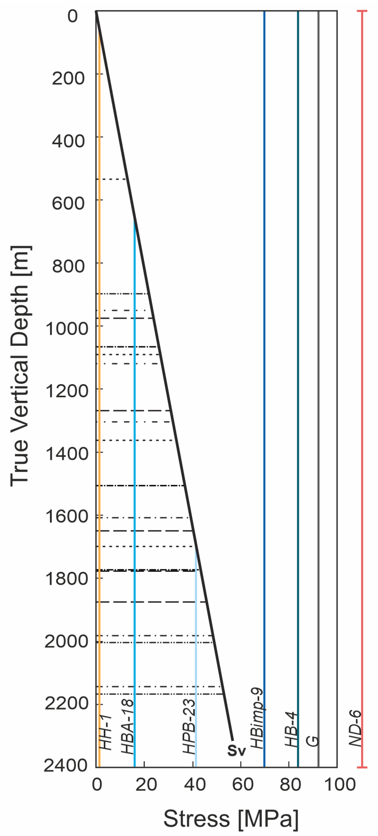

Figure 5.5: Vertical stress (S_v) profile with depth in Húsmuli and feedzone depth locations, overlaid with maximum stress of studied rocks. The Sv increases with depth, reaching a maximum stress of 50 MPa at a depth of 2200 meters. The main feedzones are located between 900 and 2200 meters.

The rocks with maximum stress below S_v are the three that exhibited the highest porosity. When S_v exceeds the ultimate strength of rocks, they will fracture and compact, reducing their porosity and altering the petrophysical and mechanical properties conditioned by it. Based on the results obtained, it is expected that rocks with maximum stress above S_v will maintain their petrophysical and mechanical properties even after burial to the mentioned depths, and therefore, the results obtained for these rocks can be considered representative of the rocks in the reservoir. On the other hand, HH-1, HBA-18, and HPB-23 will not be representative of those found at depth but rather will be fractured and compacted by the overburden. This leads to the idea that there is a maximum porosity limit for volcanic rocks at depth. Since porosity conditions the ultimate strength of the materials and its relationship with S_v determines whether there is compaction or not, it can be inferred where this porosity limit could be. At a depth of 2200 m, S_v is approximately 50 MPa, and consulting Figure 5.2, materials could exceed a maximum stress of 50 MPa if they have a porosity of 30% or less. However, this value could be higher if confining pressure is taken into account.

Similar to the mechanical properties, acoustic data shows some variability when each rock sample is observed separately. However, by comparing the average velocity values of the different samples, correlations can be established. As shown in the graph above in Figure 5.8, both P- and S- wave velocities are directly related to porosity, so that as porosity increases, wave velocity decreases. The same units described based on mechanical properties can be distinguished based solely on the P- and S-wave velocities measured as they pass through the samples, with the exception of rock HH-1, which could not be tested.

The results of the Splitting Tensile Strength test also correlate with the previously identified units based on acoustic and mechanical properties. Specifically, the Brazilian test was performed on all the rock samples except for rock G, and the results showed that the tensile strength of the rocks is inversely proportional to their porosity. This is consistent with the previously observed trend where higher porosity correlates with lower mechanical and acoustic properties. Additionally, the Splitting Tensile Strength Test (Brazilian) results helped identify the same units that were previously observed through mechanical and acoustic properties, except for rock G, which was not tested. This provides further evidence that these units accurately represent the different behaviors of the rocks studied.

5.3. Comparative Analysis of Porosity-Mechanical Property Relationships in Existing Literature

In order to validate the results of the present study, a comparison of the relationship between porosity and four mechanical properties, namely P and S wave velocity, maximum stress the samples can withstand, Young's modulus, and Poisson's ratio has been done. The value of porosity used is the connected porosity measured with the helium pycnometer. The results obtained in this research have been plotted alongside those reported in previous studies. Three different databases have been employed to obtain the data from numerous studies (Heap et al. 2020b, Di Muro et al. 2021 and Tsuji et al. 2008). All three databases, which can be consulted in Appendix B, include data on connected porosity for each sample, while Di Muro et al. (2021) additionally provides information on P wave velocity, ultimate compressive strength, and Young's modulus. The data in Heap et al. (2020b) are divided into two groups for the same lithologies but different samples, with one group containing values of Poisson's ratio and the other providing values of Young's modulus. Tsuji et al.(2008) collects data on P and S wave velocity for a limited number of samples.

The unpublished experimental data found in Heap et al. (2020b) includes Young's modulus values obtained from 276 uniaxial compression experiments carried out on volcanic rocks in the laboratory at the University of Strasbourg. The dataset comprises various types of volcanic rocks such as dacites, andesites, basalts, tuffs, and welded pyroclastic rocks. However, for comparison purposes, this study only considers andesites, basalts, and tuffs. The samples used in the experiments were sourced from different volcanic areas including Volcán de Colima (Mexico), Whakaari/White Island volcano (New Zealand), Kumamoto prefecture (Japan), Gunung Merapi (Indonesia), Mt. Etna (Italy), Stromboli (Italy), Volvic (Chaîne des Puys, France), Krafla (Iceland), and Campi Flegrei (Italy). The porosities of the samples were measured using either the triple weight water saturation technique or helium pycnometer. The data set found in Di Muro et al. (Di Muro et al. 2021) was obtained from conducting uniaxial compression tests on samples of lava, dikes, and gabbro collected from various locations at Piton de la Fournaise (Réunion Island, France). The permeability of the samples was also determined using a helium pycnometer. In addition, the P-wave velocity of each cylinder was measured along its axis at ambient pressure. The measurements of P- and S-wave velocity collected in Tsuji et al. (2008) were obtained from basaltic pillow lava samples that were gathered from 3 cores drilled in the eastern flank of the Juan de Fuca Ridge. The active-source acoustics test was conducted while subjecting the samples to confining pressures of up to 40 MPa.

Two plots have been created for each property relationship. The first plot compares the results of all samples from this study with the results of other authors, while the second plot presents the samples from this study categorized by lithologies. By examining the data in this manner, a more comprehensive analysis of the relationships between porosity and various mechanical properties of igneous rocks can be achieved. The grouping of samples by lithology provides a means of examining any trends or variations in the relationships within specific rock types, while the comparison with results from other studies enhances the validity and generalizability of the findings.

The first property examined in relation to the porosity of the sample is its ultimate compressive strength. The graphs in Figure 5.6 show that the maximum stress the samples can bear decreases as porosity increases. The comparison was made with the Di Muro et al. (2021) database, which contains information on three main rock types: basalt, dike, and gabbro. The highest values of maximum stress and the lowest porosity values correspond to the gabbros, followed by the dikes, and then the basalts. The results obtained in this study are consistent with those from the Di Muro et al. (2021) database, except for the gabbros. The UCS values of the analog gabbro studied in this research (G) were found to be twice as low as those of the gabbros in the Di Muro et al. (2021) database. This can be attributed to the textural differences in the various samples, mainly the size of the crystals that compose them and their contact points. These contact points between crystals can act as planes of weakness through which the rock fractures. Another sample that deviates slightly from the main trend is the hyaloclastite (HH-1). However, this is an unconsolidated rock, and therefore it can support lower levels of stress than a consolidated rock. The results obtained for the dike (ND-6) and the basalts (HBA-18, HPB-23, HB-4, and HBimp-9) in this study are consistent with the data used for comparison.

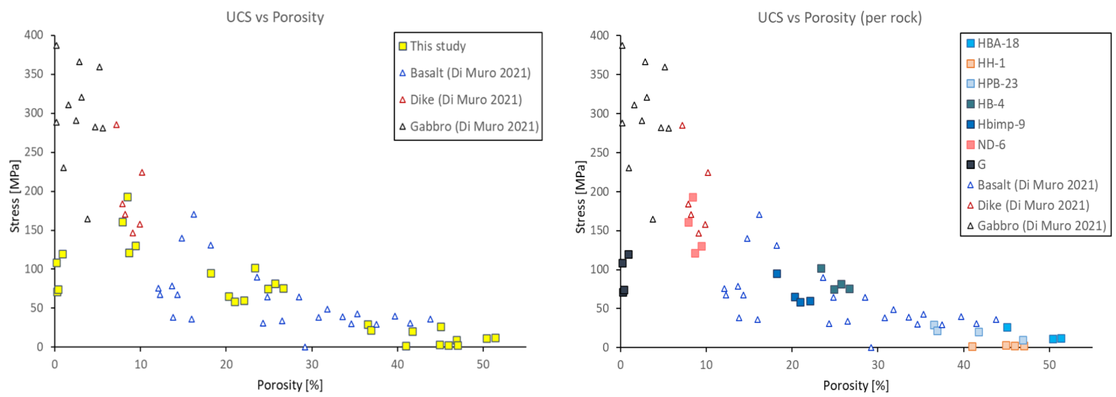

Figure 5.6: UCS-Porosity relationship

As previously mentioned in this chapter, the young modulus has been found to be linked to the UCS. These two properties are directly proportional to each other, while their relationship with porosity is inversely proportional. This means that as porosity increases, the young's modulus decreases. Figure 5.7 compares the values of young's modulus measured in this study with those in the Di Muro et al. (2021) and Heap et al. (2020b) databases. The Heap et al. 2020b database contains data on basalt, andesite, and tuff. The values for basalt in both databases are aligned, with slightly greater dispersion in the Di Muro et al. (2021) database. The results of this study are consistent with both databases, especially for basalt and dikes. The Heap et al. (2020b) database includes data on andesite, which is considered comparable to basalt since both are fine-grained extrusive igneous rocks. The slight difference in young modulus between andesite and basalt may be due to variations in mineralogical composition between rocks. The values for hyaloclastite (HH-1) are similar to those for the Heap et al. (2020b) Tuff. This is expected since both rocks are sedimentary, formed by accumulation of volcanic clasts. The values for gabbros differ significantly, as is also seen in the UCS-porosity relationship.

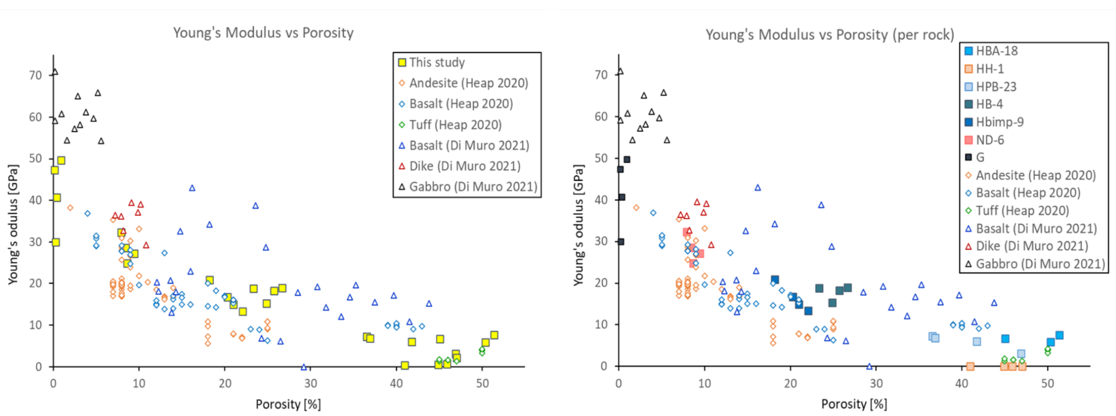

Figure 5.7: Young's Modulus-Porosity relationship

The average P and S wave velocities of each sample have been plotted against the porosity, as shown in Figure 5.8. As the porosity increases, both P and S wave velocities decrease. The above figure clearly shows how similar the results are for each group of samples with different lithologies. However, for the basalt HBA-18, the distribution appears to be random and inconsistent among the various samples. As a result, basalt HBA-18 is considered an outlier when analyzing the correlation between wave velocity values and porosity. These values have been compared in Figure 5.5 (bottom) with the P-wave velocity values from the Di Muro et al. (2021) database and the P and S wave velocity values from the Tsuji et al. (2008) database, which contains information on samples of basaltic pillow lavas. A correlation can be observed between the samples of gabbros (G) and dikes (ND-6) with the velocities measured in the pillow lavas. It is worth highlighting that the range of values among the low porosity samples is not only similar, but the trends are also comparable, despite a slight variation in values that may be attributed to differences in mineral composition. The P-wave velocity data from the Di Muro et al. (2021) database shows greater dispersion. However, when comparing the trend lines, similarities can be distinguished with the results of this study, especially if the effect of the HBA-18 sample is not taken into account. Due to the lack of S-wave velocity data in this database, it was not possible to make a comparison with the findings presented in this study.

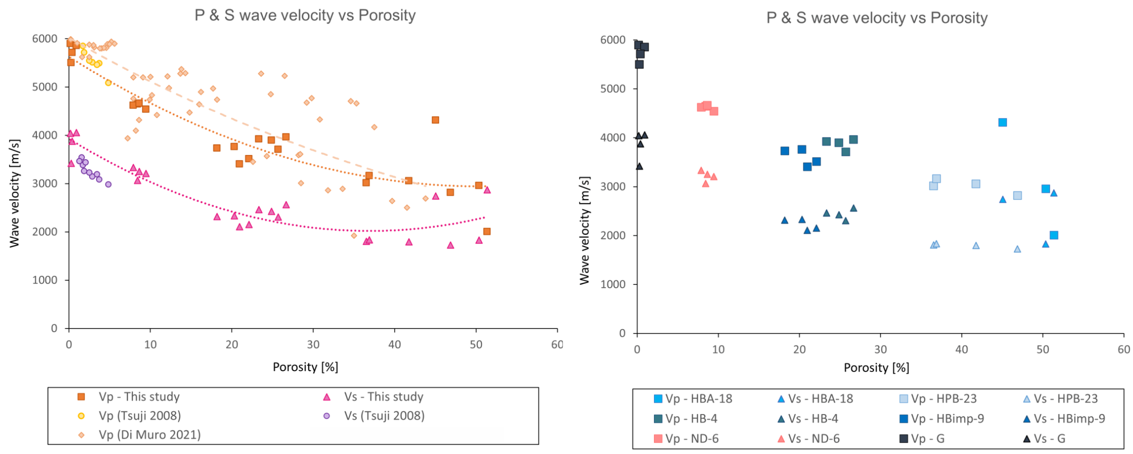

Figure 5.8: S and P wave velociyy-Porosity relationship

The findings of this study coincide with those of the Heap et al. (2020b) database, where values of Poisson's ratio do not show any correlation with porosity (See Figure 5.9). Both the data in this database as well as the data derived from this study, are scattered and show that significantly different values of Poisson's ratio can be recorded for similar porosity values. This suggests that Poisson's ratio is not related to any of the measured geomechanical properties in the studied samples.

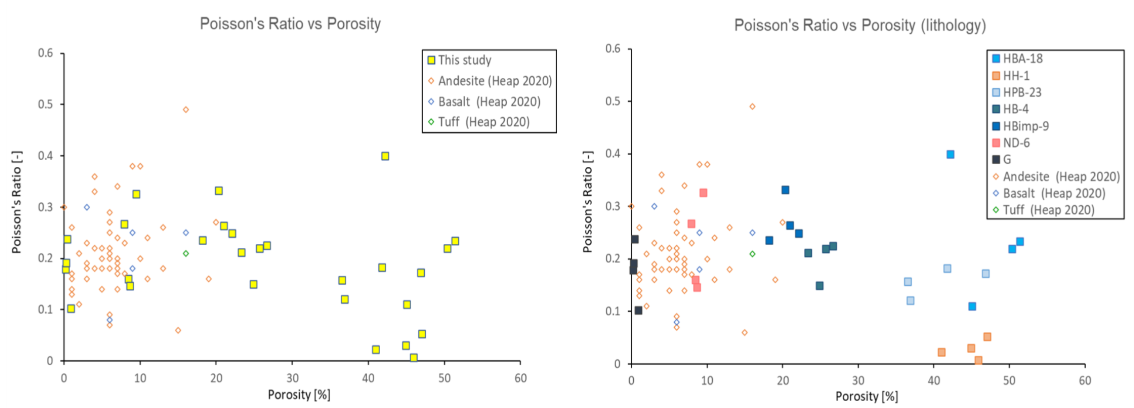

Figure 5.9: Poisson's Ratio-Porosity relationship

The influence of porosity on the Poisson's Ratio is more subtle than for the Young's Modulus, which consistently decreases with increasing porosity. This, in principle, could be attributed to the heterogeneity of volcanic rocks. However, the relationship between Poisson's ratio and porosity is also not straightforward for homogeneous isotropic sedimentary rock samples. Conflicting results have been reported by different authors (1 and 2), where 1 found that the Poisson's ratio increases with porosity for the Zubair Sandstone in Iraq, while 2 observed the opposite effect for the Rotliegend Sandstone in Germany (see Figure 5.10). Furthermore, according to Lutz (2021), the Poisson's Ratio may increase, decrease, or remain unchanged depending mainly on the shape of the pores and the Poisson's ratio of the matrix phase.

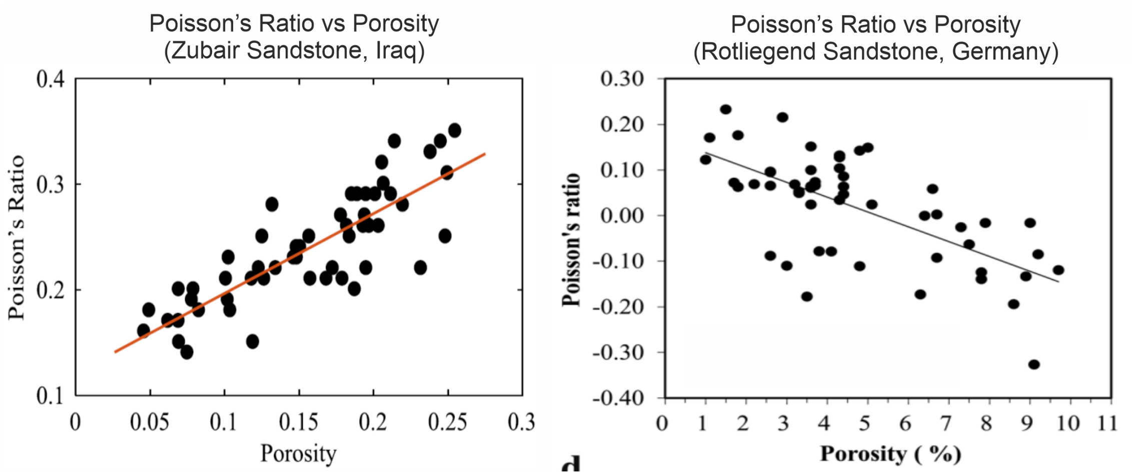

Figure 5.10: Poisson's Ratio-Porosity relationship for Zubair Sandstone and Rotliegend Sandstone.

5.4. Thermal Shock Experiment: Impact on Rock Properties

After performing the thermal shock test, all mechanical results indicate that microfractures have been generated or, at least, slight changes in the mechanical properties of the TS group have occurred. However, the acoustic data is contradictory to this, since the wave velocity increases instead of decreasing, as would happen if fractures had been generated.. Taking into account the variability of the samples from the same rock and the variability of the wave velocities through the samples belonging to the control group, which are between 220 and 357 m/s for S and P waves, respectively, it can be concluded that the results of this thermal shock are inconclusive since if changes have occurred in the samples, they are not significant enough to stand out from the natural variability of the rock. On the other hand, it is worth noting that to address the issue of sample variability, future research should conduct mechanical tests on the same samples before and after the thermal shock, without reaching the breaking point, in order to compare the results more accurately. On the other hand, it should be noted that although the reservoir and injection conditions in terms of temperature have been simulated, the effect that both overburden pressure and injection pressure can have in combination with thermal shock to generate fractures in the vicinity of well has not been taken into account.

5.5. Engineering Implications for the Hellisheiði Geothermal Field

As previously mentioned, the mineral storage of CO_2 is a rising technology that will be upscaled in the future. With the increasing concern about greenhouse gas emissions, more space in the subsurface will be used and therefore, the understanding of the subsurface and the consequences of these injections becomes crucial.

In theory, a significant portion of Iceland's subsurface has the potential for CO2 storage, but the majority of its old rocks have extremely low permeability, either due to compaction or secondary mineralization (Snæbjörnsdóttir et al. 2014). Therefore, the most practical option for onshore CO2 storage is the young and permeable basaltic formations that cover approximately one third of Iceland and are located in the active rift zone. Natural analogues have shown that each cubic meter of basaltic rock can store up to 70 kg of CO_2 (Wiese et al. 2008). To maximize the efficiency of this process, it would be interesting to increase the storage capacity of the reservoir.

As previously discussed in Chapter 2, fluid flow in the subsurface of Husmuli is primarily dominated by fractures. However, the majority of the injected CO_2 is mineralized within the porous matrix of the basalts, which offers a longer residence time for fluids and thus an extended reaction period (Matter et al. 2016). Although volcanic rocks have high porosity, not all of it is connected, and therefore, it cannot store CO_2. To maximize storage capacity and the reactive surface area that comes into contact with the injected fluid, it is essential to connect the previously unconnected porosity to the effective porosity.

One of the aims of this research is to explore the possibility of increasing storage capacity by creating fractures using thermal shock. However, the results of the experiment conducted at current injection and reservoir temperatures of 60ºC and 270ºC respectively have been inconclusive. It is possible that a larger temperature difference could be achieved by injecting cooler water to create the desired effect, although past attempts to do so have encountered problems. Gunnarsson 2011 found that the injectivity of wells is highly dependent on the temperature of the injected water, and colder water is considerably more effective in achieving the desired result due to the fracture-dominated flow. If we consider the flow through a fracture as similar to the flow between two plates, the laminar flow along a fracture follows the relation given in Equation 5.1:

$$q = \frac{d^3 \cdot h}{12 \cdot \mu \cdot l} \Delta P \tag{5.1}$$

where d is the width of the fracture, is the viscosity of the fluid, l is the length (parallel to the flow) of the fracture, h is the height (perpendicular to the flow), and P is the pressure difference driving the flow. Temperature plays an important role in the viscosity of fluids, with higher temperatures leading to lower viscosity and density of water. One would therefore expect that warmer water would have higher injectivity than colder water. However, as noted by Gunnarsson et al. (2015), the measured injectivity was actually greater for colder fluids, as illustrated in Figure 5.11. The author's explanation for this temperature-dependent injectivity is based on the thermal expansion of permeable fractures.

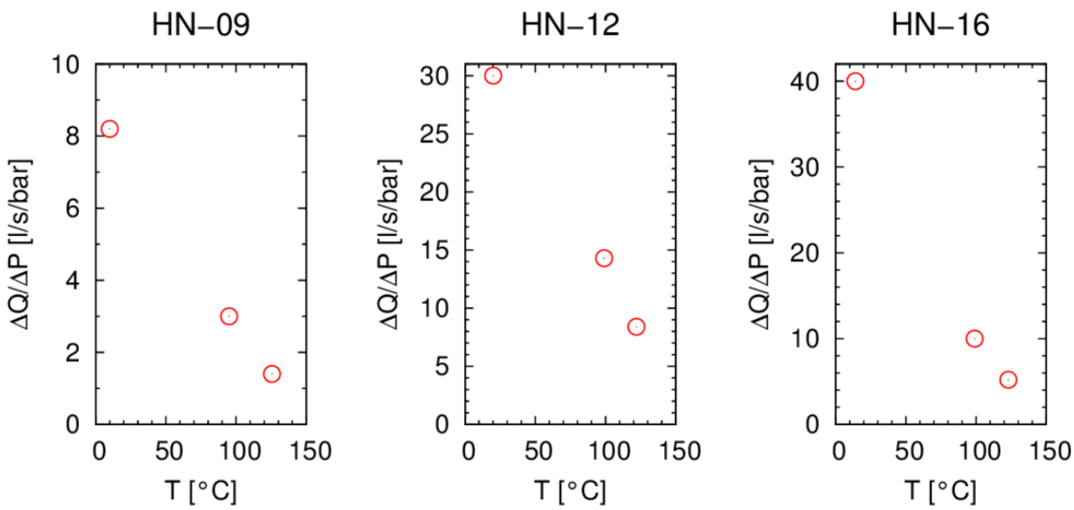

Figure 5.11: Injectivity in three wells in the Húsmúli Area measured for different temperatures of the injected water. Source: Gunnarsson et al. 2015.

According to Gunnarsson 2011, injecting cold water increases injectivity, but this generates induced seismicity, which is one of the problems associated with fractured reservoirs. Initially, this seismic activity was seen as positive because it was believed that it was creating new permeability. However, in

2011, this seismic activity reached a maximum, generating two local magnitude 4 events (Bessason et al. 2012). Although induced seismicity has never been a problem in Iceland, it indicates that the fractures in the reservoir reactivate due to thermal contraction and the resulting decrease in fault friction. This can lead to the opening of new flow paths and increase the risk of thermal breakthrough between production and reinjection wells.

The potential benefits of increasing effective porosity and permeability through thermal shock resulting from a larger temperature difference may not yield a positive outcome as it could put the reservoir's integrity at risk and increase the chance of thermal breakthrough. Despite the absence of any current issues regarding induced seismicity in Iceland, it may become a concern in the future. Consequently, thermal fracturing as a means to enhance CO2 storage capacity may not be a suitable approach in this scenario. The results of the thermal shock test under reservoir conditions conducted in this study did not show significant changes in the geomechanical properties of the samples, so injection at a temperature of 60ºC would not compromise the reservoir's integrity. However, the effect that this temperature change may have on fractures should be thoroughly studied in future research.

5.6. Additional Engineering Implications and Applications

The presented work reveals several implications that could affect the behavior and stability of the reservoir during geothermal production activities and CO_2 injection. The following points elaborate on some of the implications:

- One of the main engineering applications of the data obtained in this work is that it can be used to populate future geological models and improve the understanding of the reservoir's behavior. The data gathered on the mechanical properties of the rocks, the propagation of fractures, and the effects of fluid injection can be integrated into numerical simulations to better predict and optimize geothermal energy production. The insights gained from this work can also inform future research and exploration efforts by identifying areas of interest and potential challenges in volcanic geothermal reservoirs.

- This study can also serve as a starting point for further research on the impact that thermal shock can have on volcanic rocks. Additionally, future research could be conducted to investigate the behavior of these rocks under cyclic loading tests. Investigating which method of generating microfractures is the most efficient in increasing the permeability and CO_2 storage capacity of the reservoir would be an interesting avenue of research.

- The succession of rocks with different mechanical properties is likely to generate fractures due to stresses in the contact zones between lithologies. Fracture propagation can occur when the stresses exceed the rock's strength, leading to failure and the initiation of new fractures. The presence of fractures can significantly affect fluid flow in the reservoir. Knowledge of the mechanical properties of the rocks is essential to estimate the maximum injection pressure for each material. In some cases, the mechanical characterization of the rocks can be used to avoid the generation of fractures in certain parts of the reservoir, whereas in other cases, they can be used to deliberately induce fractures in specific locations.

- The injection of fluid into a rock formation can not only generate new fractures but also start the propagation of existing fractures. Formations with low Young modulus, which measures the stiffness of the rock, are more likely to propagate fractures.

- Dilatancy is the change in the volume of a rock due to deformation. Hyaloclastite, a clastic lithology composed of volcanic glass fragments, is particularly susceptible to dilatancy. The change in volume can alter the stress distribution and the stability of other rock formations, affecting the reservoir's integrity. Dilatancy can also lead to the formation of new fractures and the reactivation of existing ones.

6 Conclusion

As part of the SUCCEED Project (*Synergetic Utilisation of CO2 Storage Coupled with Geothermal Energy Deployment*), a field campaign was carried out in the summer of 2021 at the Husmuli reinjection site in the Hellisheiði geothermal field in Iceland. One of the objectives of the campaign was to collect surface outcrop samples for the study of their petrophysical and mechanical properties, to assess the feasibility of injecting captured and produced CO_2 into the reservoirs for enhancing geothermal production. The results of this investigation offer valuable knowledge about the petrophysical and mechanical characteristics of rocks gathered from the Hellisheiði geothermal field surface, verifying their potential as reservoir analogs and examining the possibility of utilizing thermal fracturing to improve their effective porosity and CO_2 storage capacity. In light of the evidence gathered in this study, the following conclusions can be drawn:

1. Clear interdependent relationships can be observed between Porosity, Bulk density, Ultimate strength Young's Modulus and Wave velocities when considering the average values per rock. Although no significant relationships were found between the measured parameters when comparing individual samples, this study highlights the importance of taking a broader perspective in analyzing rock properties. In general terms, the rocks studied showed a negative correlation between porosity and other parameters such as bulk density, ultimate strength, and Young's modulus. An increase in porosity resulted in a decrease of these properties. The ultimate strength and Young's modulus demonstrate a direct correlation, indicating that any increase in one of these parameters corresponds to an increase in the other. The data obtained in this research exhibits a strong correlation with results obtained by other authors, suggesting that this methodology and this findings can be effectively applied to research on volcanic rocks in other regions of the world. This study demonstrates that porosity is the main factor influencing the mechanical properties of volcanic rocks, with other factors such as mineralogical composition having a lower impact.

2. Volcanic rocks have a significant proportion of unconnected porosity. Connecting this porosity can increase the reactive surface area of the rock in contact with the fluid reinjected into the reservoir as well as the storage capacity of the reservoir, thereby making the mineral storage process more efficient.

3. Five units have consistently been distinguished based on petrophysical properties, mechanical tests, and active acoustics measurements. Ordered from higher porosity and lower mechanical parameters, these units are: Unit 1 consists of hyaloclastite HH-1, Unit 2 includes basalts HBA-18 and HPB-23, Unit 3 consists of basalts HB-4 and HBimp-9, Unit 4 is made up of dike ND-6, and Unit 5 comprises gabbro G.

4. This study has confirmed the potential usefulness of certain rocks sampled on the surface as reservoir analogs, based on experimental results compared with the model of vertical stress in the target area. It can be concluded that hyaloclastite HH-1 and basalts HBA-18 and HPB-23, which comprise unit 1 and unit 2, are likely to undergo fracturing and compaction by the overburden at the depth of the primary feedzones, as their maximum strength is lower than the vertical stress for the intervals where the feedzones are located. Conversely, the ultimate strength of

basalts HBimp-9 and HB-4, gabbro G, and dike ND-6, corresponding to unit 3, unit 4, and unit 5, respectively, exceeds the maximum vertical stress at those depths, making them representative of the reservoir rocks. A porosity limit of approximately 30% for volcanic rocks at the feedzone depth has been identified based on the relationship found between porosity and ultimate strength. This has significant implications for the selection of representative data to populate future geological models.

5. The results of a thermal shock conducted to simulate reservoir temperature conditions (270ºC) and injection temperature (60ºC) showed no significant changes. Although the differences observed in the mechanical parameters contradict the changes in the P- and S-wave velocities through the sample after the experiment, it is considered that these differences do not exceed the natural variability within the block of rock. Therefore, it can be concluded that the thermal shock does not significantly affect the petrophysical and mechanical properties of the rocks, and that this temperature difference is not sufficient to increase effective porosity. However, it should be noted that a drastic increase in this temperature difference may compromise the integrity of the reservoir, and as such, the use of thermal shock as a method to increase CO2 storage capacity should be studied in greater detail in the future.

References

Aradóttir, E., H. Sigurdardóttir, B. Sigfússon, and E. Gunnlaugsson (2011). “CarbFix: a CCS pilot project imitating and accelerating natural CO_2 sequestration”. In: *Greenhouse Gases Science and Technology* 1, pp. 105–118.

Arnason, K. and I. Magnusson (2001). “Geothermal activity in the Hengill area: Results from resistivity mapping”. In: *Orkustofnun Report* 91, p. 250.

Bandilla, K. (2020). “Carbon Capture and Storage”. In: *Future Energy. Improved, Sustainable and Clean Options for our Planet (Third Edition)*. Ed. by T. M. Letcher and L. House. Princeton, NJ, United States, pp. 669–690.

Batir, J., N. Davatzes, and R. Asmundsson (2012). “Preliminary model of fracture and stress state in the Hellisheidi geothermal field, Hengill volcanic system, Iceland”. In: *Thirty-Seventh Workshop on Geothermal Reservoir Engineering*.

Bellopede, R., A. Ferrero, L. Manfredotti, P. Marini, and M. Migliazza (2006). “The effect of thermal stresses on the mechanical behavior of natural building stones”. In: *Fracture and Failure of Natural Building Stones*, pp. 397–425.

Benson, S. and D. Cole (2008). “CO_2 sequestration in deep sedimentary formations”. In: *Elements* 4, pp. 325–331.

Bessason, B., E. Ólafsson, G. Gunnarsson, Ó. Flóvenz, S. Jakobsdóttir, S. Björnsson, and Þ. Árnadóttir (2012). “Protocol for Induced Seismicity in Geothermal Systems”. In: *Orkuveita Reykjavíku*.

Bloomfield, K. and J. Moore (1999). “Geothermal electrical production CO_2 emissions study”. In: *Proceedings of Geothermal Resource Council Annual Meeting*, p. 6.

Blower, J., J. Keating, H. Mader, and J. Phillips (2003). “The evolution of bubble size distributions in volcanic eruptions”. In: *Journal of Volcanology and Geothermal Research* 120.1-2, pp. 1–23.

Bodvarsson, G. (1960). “Hot springs and the exploitation o[natural heat resources”. In: *On the Geology and Geophysics o[Iceland.*, pp. 46–55.

Bodvarsson, G. (1961). “Physical characteristics of natural heat resources in Iceland”. In: *Jökull* 11, pp. 29–38.

Bugani, S., M. Camaiti, L. Morselli, E. Van de Casteele, and K. Janssens (2007). “Investigation on porosity changes of Lecce stone due to conservation treatments by means of X-ray nano- and improved micro-computed tomography: Preliminary results”. In: *X-Ray Spectrometry* 36, pp. 316–320.

CarbFix (2021). *Coda Terminal: A scalable onshore CO_2 mineral storage hub in Iceland*. URL: `https://www.carbfix.com/codaterminal` (visited on 01/09/2023).

CarbFix (2022). *Protecting Our Climate by Turning CO_2 Into Stone*. URL: `https://www.carbfix.com/protecting-our-climate-by-turning-co2-into-stone.` (visited on 12/07/2022).

Cashman, K. (2020). “Crystal size distribution (CSD) analysis of volcanic samples: advances and challenges”. In: *Frontiers in Earth Science* 8, p. 291.

Clifton, A. and S. Kattenhorn (2007). “Structural architecture of a highly oblique divergent plate boundary segment.” In: *Tectonophysics* 419, pp. 27–40.

Climeworks (2022). *Orca: the first large-scale plant*. URL: `https://climeworks.com/roadmap/orca` (visited on 01/09/2023).

Climeworks (2023). *Climeworks takes another major step on its road to building gigaton DAC capacity.* URL: `https://climeworks.com/news/climeworks-announces-groundbreaking-on-mammoth` (visited on 01/09/2023).

Coletti, C., G. Cultrone, L. Maritan, and C. Mazzoli (2016). “Combined multi-analytical approach for study of pore system in bricks: How much porosity is there?” In: *Materials Characterization* 121.

Colombier, M., F. Wadsworth, L. Gurioli, B. Scheu, U. Kueppers, A. Di-Muro, and D. Dingwell (2017). “The evolution of pore connectivity in volcanic rocks”. In: *Earth and Planetary Science Letters* 462, pp. 99–109.

Di Muro, A., F. Schwarzlmüller, U. Kuepper, M. Heap, and D. Dingwell (2021). “Petrophysical Characterisation of Volcanic Ejecta to Constrain Subsurface Lithological Heterogeneities: Implications for Edifice Stability at Basaltic Volcanoes”. In: *Volcanica* 4.1, pp. 41–66.

Duffield, W. and J. Sass (2003). “Geothermal energy: Clean power from the earth’s heat”. In: *USGS Circular 1249, U.S. Geological Survey*.

Eggertsson, G., Y. Lavallée, J. Kendrick, and S. Markússon (2020). “Improving fluid flow in geothermal reservoirs by thermal and mechanical stimulation: The case of Krafla volcano, Iceland.” In: *Journal of Volcanology and Geothermal Research* 391, p. 106351.

Einarsson, P. (1991). “Earthquakes and present-day tectonism in Iceland”. In: *Tectonophysics* 189, pp. 261–279.

Einarsson, P. (2001). “Structure and evolution of the Iceland hotspot.” In: *Deutsche Geophysikalische Gesellschaft, Mitteilungen* 1/2001, pp. 11–14.

Einarsson, P. (2008). “Plate boundaries, rifts and transforms in Iceland”. In: *Jökull* 58, pp. 35–58.

Foulger, G. (1995). “The Hengill geothermal area Iceland: variation of temperature gradients deduced from the maximum depth of seismogenesis.” In: *Journal of Volcanology and Geothermal Research* 65, pp. 119–133.

Franzson, H. (1988). *Nesjavellir: Permability in geothermal reservoir*. Reykjavik Energy Group (OR).

Franzson, H. (1998). “The Nesjavellir high-temperature field, SW-Iceland, reservoir geology”. In: *Proceedings 19th Annual PNOC-EDC Geothermal Conference*. Manilla, Phillippines, pp. 13–20.

Franzson, H., E. Gunnlaugsson, K. Árnason, K. Sæmundsson, B. Steingrímsson, and B. Harðarson (2010). “Subglacial and intraglacial volcanic formations in Iceland”. In: *Proceedings World Geothermal Congress*. Bali, Indonesia.

Fridriksson, T., A. Mateos, P. Audinet, and Y. Orucu (2017). “Greenhouse Gases from Geothermal Power Production”. In: *42nd Workshop on Geothermal Reservoir Engineering*, pp. 13–15.

Gislason, S., W. Broecker, E. Gunnlaugsson, S. Snæbjörnsdóttir, K. Mesfin, H. Alfredsson, E. Aradottir, B. Sigfusson, I. Gunnarsson, M. Stute, J. Matter, M. Arnarson, I. Galeczka, S. Gudbrandsson, G. Stockman, D. Wolff-Boenisch, A. Stefansson, E. Ragnheidardottir, T. Flaathen, A. Gysi, J. Olssen, K. Didriksen, S. Stipp, B. Menez, and E. Oelkers (2014). “Rapid solubility and mineral storage of CO2 in basalt”. In: *Energy Procedia* 63, pp. 4561–4574.

Gislason, S. and E. Oelkers (2003). “Mechanism, rates, and consequences of basaltic glass dissolution: II. An experimental study of the dissolution rates of basaltic glass as a function of pH and temperature”. In: *Geochimica et Cosmochimica Acta* 67.20, pp. 3817–3832.

Grant, M. and P. Bixley (2011). “Geothermal Reservoir Engineering”. In: *Science Ltd, Elsevier* 2nd ed. Oxford, UK., pp. 261–279.

Gudfinnsson, G., H. Helgadottir, C. Feucht, and H. Ingólfsson (2010). “Húsmúli – well HN-16: Drilling, 1st and 2nd stage. Drilling for surface casing at 95 m, production casing at 660 m and production part in 2204 m depth”. In: *Icelandic*. Iceland GeoSurvey, Reykjavík.

Gunnarsson, G. (2011). “Mastering Reinjection in the Hellisheiði Field, SW-Iceland: A Story of Successes and Failures. Proceedings, 36th Workshop on Geothermal Reservoir Engineering.” In: *Report ÍSOR*. Stanford, California.

Gunnarsson, G., A. Arnaldsson, and A. Oddsdóttir (2011). “Model Simulations of the Hengill Area, Southwestern Iceland”. In: *Transport in Porous Media* 90, pp. 3–22.

Gunnarsson, G., B. Gunnarsson, and B. Júlíusson (2015). “Reinjection into a Fractured Reservoir – Induced Seismicity and Other Challenges in Operating Reinjection Wells in the Hellisheiði Field, SW-Iceland”. In: *Proceedings World Geothermal Congress*.

Gutknecht, V., S. Snæbjörnsdóttir, B. Sigfússon, E. Aradóttir, and L. Charles (2018). “Creating a carbon dioxide removal solution by combining rapid mineralization of CO_2 with direct air capture”. In: *Energy Procedia* 146, pp. 129–134.

Harðarson, B., G. Einarsson, H. Franzson, and E. Gunnlaugsson (2009). “olcano-tectonic-geothermal interaction at the Hengill triple junction, SW Iceland”. In: *GRC 2009, Annual Meeting*.

Harðarson, B., H. Tryggvason, C. Feucht, G. Guðfinnsson, and M. Sigurgeirsson (2011). *Húsmúli – Hola HN-17 [Húsmúli – Well HN-17]*. Report Iceland GeoSurvey: ÍSOR-2011/022.

Hawkins, D. (2004). “No exit: thinking about leakage from geologic carbon storage sites”. In: *Energy* 29, pp. 1571–1578.

Heap, M., D. Gravley, B. Kennedy, H. Gilg, E. Bertolett, and S. Barker (2020a). “Quantifying the role of hydrothermal alteration in creating geothermal and epithermal mineral resources: The Ohakuri ignimbrite (Taupō Volcanic Zone, New Zealand)”. In: *Journal of Volcanology and Geothermal Research* 390, p. 106703.

Heap, M., M. Villeneuve, F. Albino, J. Farquharson, E. Brothelande, F. Amelung, J. Got, and P. Baud (2020b). “Towards more realistic values of elastic moduli for volcano modelling”. In: *Journal of Volcanology and Geothermal Research* 390, p. 106684.

Heap, M. and M. Violay (2021). “The mechanical behaviour and failure modes of volcanic rocks: a review.” In: *Bull Volcanol* 83.33.

Helgadóttir, H., S. Snæbjörnsdóttir, S. Níelsson, T. Gunnarsdóttir, B. Matthíasdóttir, G. Harðarson, H. Einarsson, H. Franzson, and S. Gunnarsdóttir (2010). “Geology and Hydrothermal Alteration in the Reservoir of the Hellisheiði High Temperature System, SW-Iceland”. In.

Hreinsdóttir, S., P. Einarsson, and F. Sigmundsson (2001). “Crustal deformation at the oblique spreading Reykjanes Peninsula, SW Iceland: GPS measurements from 1993 to 1998.” In: *J. Geophys.* 106.13, p. 816.

Imperial-College-London (2020). *SUCCEED Project*. URL: `https://www.imperial.ac.uk/energy-futures-lab/succeed/about/` (visited on 01/18/2022).

Ingolfsson, O., O. Sigmarsson, F. Sigmundsson, and L. Símonarson (2008). “The dynamic geology of Iceland”. In: *Jökull* 58, pp. 1–2.

Jakobsson, S. and M. Gudmundsson (2008). “Subglacial and intraglacial volcanic formations in Iceland”. In: *Jökull*, pp. 179–196.

Janssen, M., A. Barnhoorn, D. Draganov, K.-H. Wolf, and S. Durucan (2021). “Seismic Velocity Characterisation of Geothermal Reservoir Rocks for CO_2 Storage Performance Assessment”. In: *Applied Sciences* 11.3641.

Jóhannesson, H. and K. Sæmundsson (1999). “Geological map of Iceland, scale 1.000.000.” In: Icelandic Institute of Natural History.

Johnson, G. and S. P. Jakobsson (1985). “Structure and petrology of the Reykjanes Ridge between 62º55’N and 63º48’N”. In: *J. Geophys.* 90, pp. 10073–10083.

Karlsdóttir, M., O. Pálsson, H. Pálsson, and L. Maya-Drysdale (2015). “Life cycle inventory of a flash geothermal combined heat and power plant located in Iceland”. In: *Int. J. Life Cycle Assess* 20, pp. 503–519.

Karlsdóttir, M., O. Pálsson, H. Pálsson, and C. Science (2010). “LCA of combined heat and power production at Hellishei Ði geothermal power plant with focus on primary energy efficiency”. In: *12th Int. Symp. Dist. Heat. Cool.* 9, pp. 184–191.

Khodayar, M., G. Axelsson, and B. Steingrímsson (2015). *Potential Structural Flow Paths for Tracers and Source Faults of Earthquakes at Húsmúli, Hengill, South Iceland*. Report Iceland GeoSurvey: ÍSOR-2015/035, 42 p.

Klinkenberg, L. (1941). “The Permeability Of Porous Media To Liquids And Gases”. In: *Drilling and Production Practice*, pp. 200–213.

Kristjánsson, B., G. Axelsson, G. Gunnarsson, I. Gunnarsson, and F. Óskarsson (2016). "Comprehensive Tracer Testing in the Hellisheiði Geothermal Field in SW-Iceland". In: *Proceedings 41st Workshop on Geothermal Reservoir Engineering* 90. Stanford, California.

Matter, J., M. Stute, S. Snæbjörnsdottir, E. Oelkers, S. Gislason, E. Aradottir, B. Sigfusson, I. Gunnarsson, H. Sigurdardottir, E. Gunnlaugsson, G. Axelsson, H. Alfredsson, D. Wolff-Boenisch, K. Mesfin, D. Taya, J. Hall, K. Dideriksen, and W. Broecker (2016). "Rapid carbon mineralization for permanent disposal of anthropogenic carbon dioxide emissions". In: *Science* 352, pp. 1312–4.

Metz, B., O. Davidson, H. De-Coninck, M. Loos, and L. Meyer (2005). *IPCC Special Report on Carbon Dioxide Capture and Storage*. New York.

Oelkers, E., S. Gislason, and J. Matter (2008). "Mineral carbonation of CO_2". In: *Elements* 4, pp. 331–335.

Orkustofnun (2006). *Energy in Iceland: Historical Perspective, Present Status, Future Outlook*. Reference Booklet on Iceland's Energy Resources. Ministries of Industry and Commerce. Reykjavik, Iceland.

Orkustofnun (2021a). *Energy Statistics in Iceland*. Ministries of Industry and Commerce. Reykjavik, Iceland.

Orkustofnun (2021b). *Fuels and Energy Transition*. Ministries of Industry and Commerce. URL: `https://nea.is/fuels/` (visited on 11/23/2022).

Ratouis, T., S. Snæbjörnsdóttir, G. Gunnarsson, I. Gunnarsson, B. Kristjánsson, and E. Aradóttir (2019). "Modelling the Complex Structural Features Controlling Fluid Flow at the CarbFix2 Reinjection Site, Hellisheiði Geothermal Power Plant, SW-Iceland". In: *Proceedings, 44th Workshop on Geothermal Reservoir Engineering*. SGP-TR-214. Stanford, California: Stanford University, p. 18.

Reykjavik Energy Group (OR) (2021). *Environmental data annual report*. Reykjavik, Iceland.

Sæmundsson, K. (1974). "Evolution of the axial rifting zone in northern Iceland and the Tjörnes fracture zone". In: *Geological Society of America Bulletin* 85.4, pp. 495–504.

Sæmundsson, K. (1979). "Outline of the geology of Iceland". In: *Jökull* 29, pp. 7–28.

Sæmundsson, K. (2016). "Hengill". In: *Ilyinskaya, Larsen and Gudmundsson: Catalogue of Icelandic Volcanoes*. IMO, UI, CPD-NCIP.

Sella, G., T. Dixon, and A. Mao (2002). "Revel: A model for recent plate velocities from space geodesy". In: *Journal of Geophysical Research* 107, pp. 2081–2110.

Shea, T., B. Houghton, L. Gurioli, K. Cashman, J. Hammer, and B. Hobden (2010). "Textural studies of vesicles in volcanic rocks: an integrated methodology". In: *Journal of Volcanology and Geothermal Research* 190.3-4, pp. 271–289.

Sigfusson, B., S. Gislason, J. Matter, M. Stute, E. Gunnlaugsson, I. Gunnarsson, E. Aradottir, H. Sigurdardottir, K. Mesfin, H. Alfredsson, D. Wolff-Boenisch, M. Arnarsson, and E. Oelkers (2015). "Solving the carbon-dioxide buoyancy challenge: The design and field testing of a dissolved CO2 injection system". In: *International Journal of Greenhouse Gas Control* 37, pp. 213–9.

Sigfússon, B., M. Arnarson, S. Snæbjörnsdóttir, M. Karlsdóttir, E. Aradóttir, and I. Gunnarsson (2018). "Reducing emissions of carbon dioxide and hydrogen sulphide at Hellisheidi power plant in 2014-2017 and the role of CarbFix in achieving the 2040 Iceland climate goals". In: *Energy Procedia* 146, pp. 135–145.

Siratovich, P., M. Heap, M. Villenuece, J. Cole, B. Kennedy, J. Davidson, and T. Reuschlé (2016). "Mechanical behaviour of the Rotokawa Andesites (New Zealand): Insight into permeability evolution and stress-induced behaviour in an actively utilised geothermal reservoir." In: *Geothermics* 64, pp. 163–179.

Snæbjörnsdóttir, S. (2011). "The Geology and Hydrothermal Alteration at the Western Margin of the Hengill Volcanic System". Master's thesis. Reykjavík: University of Iceland.

Snæbjörnsdóttir, S., F. Wiese, T. Fridriksson, H. Ármansson, G. Einarsson, and S. Gislason (2014). "CO_2 storage potential of basaltic rocks in Iceland and the oceanic ridges". In: *Energy Procedia* 63, pp. 4585–4600.

Stefánsson, R., G. Gudmundsson, and P. Halldorsson (2008). “Tjörnes fracture zone. New and old seismic evidences for the link between the North Iceland rift zone and the Mid-Atlantic ridge”. In: *Tectonophysics* 447.1, pp. 117–126.

Tómasdóttir, S. (2018). “Flow Paths in the Húsmúli Reinjection Zone, Iceland”. Master’s thesis. Uppsala, Sweden: Department of Earth Sciences, Uppsala University.

Toramaru, A. (2020). “Measurement of bubble size distributions in vesiculated rocks with implications for quantitative estimation of eruption processes”. In: *Journal of Volcanology and Geothermal Research* 43.1-4, pp. 71–90.

Tsuji, T. and G. Iturrino (2008). “P-Velocity-porosity relationships in oceanic basalt from eastern flank of the Juan de Fuca Ridge: The effect of crack closure on seismic velocity”. In: *Exploration Geophysics* 39, pp. 41–51.

United-Nations (2015). *Adoption of the Paris Agreement, 21st Conference of the Parties*. Framework Convention on Climate Change. Paris, France.

Voltolini, M., D. Zandomeneghi, L. Mancini, and M. Polacci (2011). “Texture analysis of volcanic rock samples: quantitative study of crystals and vesicles shape preferred orientation from X-ray microtomography data”. In: *Journal of Volcanology and Geothermal Research* 202.1-2, pp. 83–95.

Weaver, J., G. Eggertsson, J. Utley, P. Wallace, A. Lamur, and J. Kendrick (2020). “Thermal liability of hyaloclastite in the Krafla geothermal reservoir, Iceland: the impact of phyllosilicates on permeability and rock strength.” In: *Geofluids*.

Weydt, L., A. Ramírez-Guzmán, A. Pola, B. Lepillier, and J. Kummerow (2020). “Petrophysical and mechanical rock property database of the Los Humeros and Acoculco geothermal fields (Mexico)”. In: *Earth Syst Sci Data* 390, pp. 1–39.

Wiese, F., T. Fridriksson, and H. Armannsson (2008). *CO2 Fixation by Calcite in High-temperature Geothermal Systems in Iceland*. Tech. rep. ISORí2008/003. Iceland Geosurvey.

Wright, H., K. Cashman, E. Gottesfeld, and J. Roberts (2009). “Pore structure of volcanic clasts: Measurements of permeability and electrical conductivity.” In: *Earth and Planetary Science Letters* 280.1-4, pp. 93–104.

Xu, T., E. Sonnenthal, N. Spycher, and K. Pruess (2006). “TOUGHREACT - A simulation program for non-isothermal multiphase reactive geochemical transport in variably saturated geologic media: Applications to geothermal injectivity and CO2 geologic sequestration”. In: *Computers and Geosciences* 32, pp. 146–165.

Ziegler, M., M. Rajabi, O. Heidbach, G. Hersir, and K. Ágústsson (2016). “The stress pattern of Iceland”. In: *Tectonophysics* 107.

A

Energy Statistics in Iceland 2020

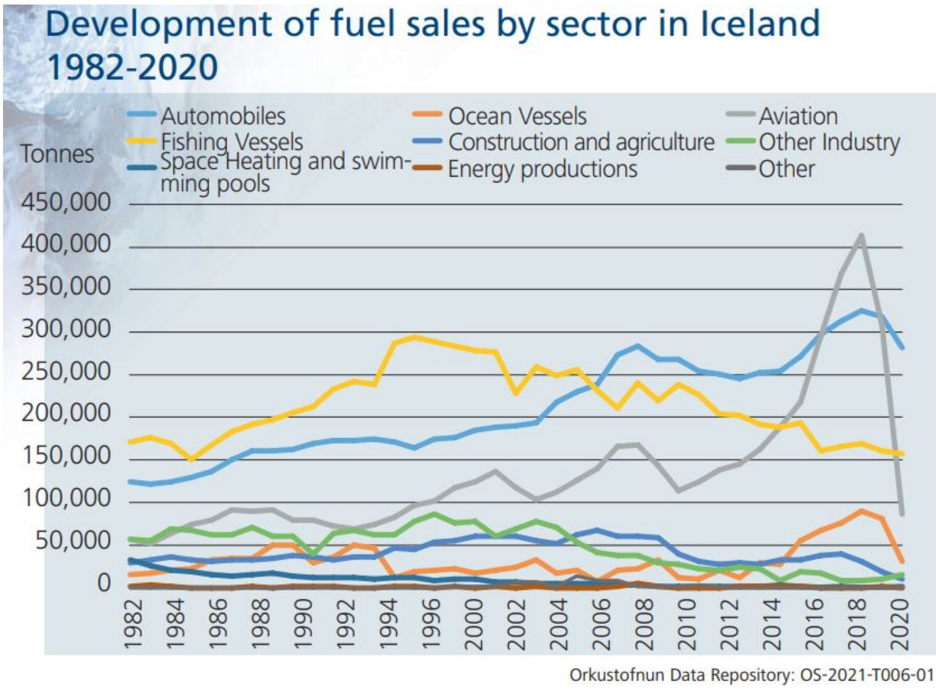

Figure A.1: statisticsss.

B

Databases: Comparative Analysis

Di Muro 2021

Rock	Porosity [%]	Dry P-wave velocity (km/s)	Vp (m/s)	Max. Stress [Mpa]	Young's Modulus [Gpa]
Basalt	29.2	4.68	4680	-	-
Basalt	23.6	5.28	5280	89.9	38.8
Basalt	26.5	5.23	5230	33.7	6.2
Basalt	24.8	4.85	4850	64.7	28.8
Basalt	43.8	2.69	2690	36	15.3
Basalt	41.5	2.5	2500	31.1	10.8
Basalt	39.7	2.64	2640	40.1	17.2
Basalt	35	1.92	1920	-	-
Basalt	28.2	3.59	3590	-	-
Basalt	28.4	3.61	3610	-	-
Basalt	22.6	3.45	3450	-	-
Basalt	24.3	3.57	3570	31	6.9
Basalt	14.8	4.47	4470	139.7	32.6
Basalt	16	4.64	4640	36.3	23
Basalt	16.2	4.9	4900	170.4	43.1
Basalt	18.2	4.74	4740	131	34.3
Basalt	17.7	4.97	4970	-	-
Basalt	30.8	4.33	4330	38.6	19.3
Basalt	37.5	4.17	4170	29.7	15.5
Basalt	35.3	4.66	4660	43.1	19.7
Basalt	34.6	4.71	4710	30	16.7
Basalt	29.8	4.77	4770	-	-
Basalt	31.8	2.86	2860	48.7	14.3
Basalt	33.6	2.89	2890	39	12.1
Basalt	28.5	3.01	3010	64.4	17.8
Basalt	13.7	5.28	5280	79	20.8
Basalt	12.3	4.98	4980	67.7	18.1
Basalt	12.1	5.22	5220	75.4	20.4
Basalt	13.8	5.37	5370	38.6	13.1
Basalt	10	5.21	5210	-	-
Basalt	14.3	5.29	5290	67.5	18
Dike	7.9	4.76	4760	184.3	36.2
Dike	10.2	4.83	4830	224.4	39.1
Dike	9.9	4.74	4740	158.1	37.1
Dike	9.1	5.2	5200	146.6	39.5
Dike	7.9	5.2	5200	-	-
Dike	8.6	4.32	4320	-	-
Dike	10.8	4.42	4420	-	29.3
Dike	7.2	3.94	3940	285.3	36.5

Dike	8.2	4.1	4100	170.5	32.8
Gabbro	5.2	5.94	5940	359.7	65.9
Gabbro	2.5	5.62	5620	290.9	57.3
Gabbro	0.2	5.99	5990	387.3	71
Gabbro	2.9	6.18	6180	366.2	65.1
Gabbro	1.6	5.62	5620	311.1	54.5
Gabbro	5.6	5.9	5900	280.9	54.4
Gabbro	3.1	5.82	5820	320.8	58.2
Gabbro	4.7	5.89	5890	282.3	59.7
Gabbro	3	5.87	5870	-	-
Gabbro	4.6	5.81	5810	-	-
Gabbro	4	5.8	5800	-	-
Gabbro	2.5	5.88	5880	-	-
Gabbro	5	5.89	5890	-	-
Gabbro	4.3	5.81	5810	-	-
Gabbro	3.8	5.8	5800	164.5	61.2
Gabbro	1	5.91	5910	230.1	60.8
Gabbro	0.2	5.98	5980	288.3	59.2

Heap 2020

Rock	Porosity [%]	Young's Modulus [Gpa]
andesite	7	19.2
andesite	7	20.2
andesite	7	20.5
andesite	7	19.6
andesite	7	20
andesite	21	7.8
andesite	21	7.9
andesite	22	7.1
andesite	22	6.8
andesite	22	6.8
andesite	10	21.8
andesite	11	20.3
andesite	12	18.5
andesite	9	23.9
andesite	8	19.9
andesite	8	19.7
andesite	8	21.1
andesite	8	20.4
andesite	9	26.7
andesite	8	28.7
andesite	9	30.2
andesite	10	33.1
andesite	18	5.6
andesite	18	9.7
andesite	18	10.9
andesite	18	7.2
andesite	25	9
andesite	25	9.3
andesite	25	10.8
andesite	25	10.9
andesite	8	18.5
andesite	8	19.3
andesite	8	16.9
andesite	8	17.2
andesite	8	17.7

Rock	Porosity [%]	Poisson's Ratio [-]
andesite	11	0.24
andesite	13	0.26
andesite	7	0.19
andesite	6	0.25
andesite	13	0.18
andesite	6	0.09
andesite	6	0.27
andesite	7	0.34
andesite	7	0.2
andesite	7	0.24
andesite	7	0.14
andesite	7	0.17
andesite	6	0.22
andesite	8	0.23
andesite	6	0.18
andesite	6	0.29
andesite	8	0.17
andesite	3	0.18
andesite	4	0.18
andesite	1	0.26
andesite	3	0.19
andesite	9	0.38
andesite	6	0.2
andesite	19	0.16
andesite	20	0.27
andesite	15	0.06
andesite	16	0.49
andesite	3	0.16
andesite	10	0.38
andesite	11	0.16
andesite	4	0.36
andesite	1	0.16
andesite	1	0.17
andesite	2	0.21
andesite	1	0.14

andesite	7	19.7
andesite	9	18.7
andesite	8	19.7
andesite	8	19.8
andesite	7	17
andesite	8	20
andesite	8	19.4
andesite	8	20.4
andesite	9	19.5
andesite	7	18
andesite	8	19.6
andesite	8	20.2
andesite	7	20.5
andesite	7	19.8
andesite	8	17.2
andesite	7	35.4
andesite	8	30.9
andesite	8	28
andesite	8	25.7
andesite	2	38.2
andesite	13	16.9
andesite	13	16.6
andesite	13	16.2
andesite	14	19
andesite	14	16.8
basalt	24	8.9
basalt	23	9
basalt	25	6.3
basalt	9	28.1
basalt	8	29.2
basalt	9	27
basalt	19	18.3
basalt	18	20
basalt	19	14.3
basalt	16	15
basalt	15	17.5
basalt	18	14.6
basalt	8	27.8
basalt	9	24.8
basalt	8	27.8
basalt	5	31.4
basalt	5	30.8
basalt	5	29
basalt	5	29.2
basalt	5	31.5
basalt	10	19.7
basalt	14	16.2
basalt	14	17
basalt	15	16.6
basalt	12	15.1
basalt	14	14
basalt	15	15
basalt	12	14.9
basalt	13	13.9
basalt	12	14.9
basalt	12	16
basalt	4	36.9
basalt	13	27.3
basalt	20	17.1

andesite	2	0.11
andesite	4	0.33
andesite	1	0.13
andesite	7	0.18
andesite	5	0.2
andesite	10	0.2
andesite	6	0.07
andesite	6	0.21
andesite	3	0.23
andesite	4	0.22
andesite	0	0.3
andesite	5	0.14
andesite	5	0.22
andesite	5	0.18
basalt	3	0.3
basalt	16	0.25
basalt	9	0.18
basalt	6	0.08
basalt	9	0.25
tuff	16	0.21

basalt	21	15.4
basalt	20	16.8
basalt	21	15.2
basalt	21	16.1
basalt	21	16.1
basalt	39	10
basalt	40	9.8
basalt	40	10.3
basalt	40	10.4
basalt	40	9.4
basalt	42	9.1
basalt	43	9.8
basalt	39	9.9
tuff	46	1.6
tuff	47	1.3
tuff	45	1.3
tuff	46	1.6
tuff	45	1.8
tuff	50	4
tuff	50	4
tuff	50	4
tuff	50	3.2
tuff	50	4.2

Tsuji 2008

Rock	**Porosity [%]**	**Vp [m/s]**	**Vs [m/s]**
Pillow margin	3.72	5492.86	3085
Pillow margin	2.85	5515	3148.33
Pillow Massive	3.44	5463.85	3194.17
Pillow Massive	1.7	5850.71	3385
Pillow Massive	2.5	5551.43	3230.77
Pillow centre	2.05	6076.15	3440.77
Pillow margin	1.85	5717.143	3263.58
Pillow centre	1.54	6210	3542.31
Pillow margin	4.84	5090.71	2983.08
Pillow centre	1.27	6003.85	3468.46